Title
The development and evaluation of a three-dimensional musculoskeletal model to investigate jerboa hindlimb dynamics

Permalink
https://escholarship.org/uc/item/8qg1w3h7

Author
Abdelrahman, Yasser

Publication Date
2023

Peer reviewed|Thesis/dissertation

UNIVERSITY OF CALIFORNIA SAN DIEGO

The development and evaluation of a three-dimensional musculoskeletal model to investigate jerboa hindlimb dynamics

A Thesis submitted in partial satisfaction of the requirements for the degree Master of Science

in

Bioengineering

by

Yasser Abdelrahman

Committee in charge:

Professor Andrew D. McCulloch, Chair
Professor Kimberly Lynn Cooper
Professor Daniela Valdez-Jasso

2023

The Thesis of Yasser Abdelrahman is approved, and it is acceptable in quality and form for publication on microfilm and electronically.

University of California San Diego

2023

DEDICATION

Within the usual margin restrictions, any format is acceptable for this page. If you choose to have an Epigraph page, any formatting is also acceptable for that page.

TABLE OF CONTENTS

LIST OF FIGURES

LIST OF TABLES

ACKNOWLEDGEMENTS

I would like to begin by expressing gratitude and acknowledgement to my primary advisor, Dr. Andrew McCulloch, for the inclusive environment and consistent feedback when needed. I would like to thank Dr. Daniela Valdez Jasso for her comforting presence and constant discussions to ensure I was making progress. Additionally, I would like to thank Dr. Kimberly Cooper for bringing this project idea into existence, extending help from her lab and always being willing to provide concrete feedback and objective knowledge. It is very important to acknowledge that this work would not be possible without the generous funding support of the Wu Tsai Human Performance Alliance and Joe and Clara Tsai Foundation.

Immense thanks to collaborators at the university of Michigan, Dr. Talia Moore, Dr. Juri Miyamae, Xun Fu. For providing focused feedback and assisting with many project doubts by extending their expertise and assistance. More thanks go to everyone in the bioengineering department, biological department and VA medical center at UCSD that assisted with pushing various inputs of the project through.

Thank you to all the members of the Cardiac Mechanics Research Group, for those who made me feel like family and gave me endless encouragement. Thank you, Jen Stowe, Dr. Katie Knaus, Rebecca Gow, Pranav Ravi Embar, Lisa Pankewitz, Marcus Hock, Dr. Stephanie Khuu. Thank you to Dr. Swithin Samuel Razu, for being my primary mentor and lending your expertise in the field of musculoskeletal modeling.

Special gratitude to my family and friends, for providing the care and safe place needed to become who I am today. To my parents and siblings for their support and confidence in me, and to my close friends who kept my spirits elevated and helped keep me grounded.

ABSTRACT OF THE THESIS

The development and evaluation of a three-dimensional musculoskeletal model to investigate jerboa hindlimb dynamics

by

Yasser Abdelrahman

Master of Science in Bioengineering

University of California San Diego, 2023

Professor Andrew D. McCulloch, Chair

The lesser Egyptian jerboa, *Jaculus jaculus*, is a small bipedal rodent with unique morphological features such as disproportionately long hindlimbs and tail, fused metatarsal bones, and the loss of medial and lateral digits. These contribute to an extraordinary repertoire of locomotion including high accelerations and decelerations resulting in unpredictable ricochetal motion. In addition to speed, jerboa are capable of producing immense ground reaction forces, allowing for propulsion of their bodies forward and upward over ten times their hip height. This unmatched performance combined with their unique morphological characteristics separates them from other small mammals and invites great interest in the study of their biomechanics and movement. Investigating muscle interactions and how they ultimately result in whole body movement using *in-vivo* experimentation alone is not always practical. Therefore, implementing a detailed computational model can provide insights into the musculoskeletal dynamics of the jerboa. This study describes and evaluates the development of the first three-dimensional model of jerboa hindlimb biomechanics based on detailed anatomical measurement collected from micro computed tomography (microCT) scans. Joints are generated for all bones in the hindlimb following International Society of Biomechanics (ISB) standards, with segment mass properties of each geometry measured experimentally and calculated computationally. Tendon insertions and muscle lines of action were validated using microdissections and biomechanics experiments. A sensitivity analysis was conducted to evaluate the model's robustness to changes in input parameters and to identify muscle and joint parameters that are particularly important for locomotor performance. This model combined with measured kinematics, ground reactions forces, and contractile muscle properties can be used to better understand how anatomic and physiological adaptations in the jerboa have evolved to generate the joint moment arms and control mechanisms that give rise to extreme locomotor performance and stability.

Chapter 1 : Introduction

Movement of mammalian bodies requires a complex orchestra of systems, with skeletal muscle activation as the main determinant of loads acting on joints, moving bones relative to each other to produce motion. Even with direct measurement of these loads, much of the complexity of the neuro-musculoskeletal systems prevents us from breaking down contributions of systems, identifying individual interactions or feedback mechanisms that allow for optimal control or movement [1–4].

The implementation of detailed computational musculoskeletal models has become a useful technique for investigating interactions between neural, skeletal and muscular systems in the body [2]. By dissecting the roles of these systems, we can probe morphological and anatomical features and adaptations that help contribute to the production of movement. Generic rigid-body dynamic tools have become increasingly capable of predicting and simulating accurate, fast, and reliable musculoskeletal dynamics that may be difficult or impossible to measure experimentally [5]. Quantification of values such as joint loads, muscle forces, or work produced within the system provide a deeper analysis of coordinated muscle activation patterns, but are often difficult or impossible to do with the use of experimental measurements alone, even when studying seemingly simple motions [1].

Although the field of musculoskeletal modeling has continued to grow, the vast majority of three-dimensional (3D) models to date have largely focused on depicting movement in large terrestrial animals or humans [6–11]. These investigations are essential to our understanding of musculoskeletal systems and environmental adaptations in large mammals with motion that is easily modeled or predicted, but leave us without insights about smaller species that typically use quick and erratic motion [12]. Although uncommon, current models of small mammals focus on quadrupedal rodents exhibiting predictable steady-state movements [13,14]. Modeling well-studied rodent species allows for mechanistic and easier one-to-one comparison of model results to humans. Moreover, using multi-body rigid musculoskeletal models to study rodents with upright posture or bipedal locomotion will allow for an approach to investigate contributions of tissue to extreme or unpredictable biomechanical movement rather than just disease states.

The lesser Egyptian jerboa (*Jaculus jaculus*), a bipedal rodent native to the deserts of Africa and the Middle East, offers a unique animal model for studying the biomechanics of extreme performance and unique locomotion. The jerboa displays unpredictable ricochetal locomotion, often attributed to its unusual morphological features. A part of the superfamily, *Dipodoidae*, jerboa are the only obligate bipeds and among very few rodents that use this as a form of locomotion, inviting many researchers to probe their associations with the evolution of bipedalism [15–18]. Among their unique morphology, they have exaggeratedly elongated hindlimbs; over three times their forelimb length, which features the fusion of three metatarsal bones and the loss of medial and lateral phalanxes [16,17]. Jerboa are capable of using various gait cycles throughout a dynamic range of speeds under high accelerations and decelerations by employing their eccentric morphological features [19]. They are also well known for exhibiting leaps of over ten times their hip height, an action of maximal performance consistently used during predator evasion [20].

Early studies of the jerboa focused on simply observing and documenting the locomotor abilities in jerboa and often comparing them with those of other closely related rodents [16,21,22]. Other studies have taken a more phylogenetic approach, investigating genes, habitats, or predatory pressures responsible for limb growth proportions, bipedalism and its potential contributions towards the jerboas abilities [12,18,23,24]. In 2017, Moore *et al.* developed the first study to offer a more detailed investigation of musculoskeletal mechanisms of the jerboa, by conducting a two-dimensional inverse kinematics analysis to quantify muscle and tendon contributions and mechanical work during vertical leaping [20]. The study provided the first steps to identifying that jerboas leaping is primarily muscle contraction-based due to stiff tendons that limit energy storage relative to other mammals [20]. Following that study, more detailed quantification of jerboa footfall patterns, number of gait patterns, and transitions between them was modeled using a spring-loaded pendulum model allowing researchers to identify an uncoupling of limb pairs to allow for the jerboas almost instantaneous gait transitions independent of speed. All of the above studies separately investigate aspects of the neural, muscular, or skeletal system that are responsible for the jerboas movement. However, because of the complexity associated with integrating these three systems, little is known about the detailed musculoskeletal mechanisms that allow them to exhibit distinctive and non-traditional biomechanics.

Thus, creating a 3D model of the jerboa musculoskeletal system that can bridge the gap between these systems is the first step towards understanding complex muscular control during their ricochetal movement. The goal of this work is to develop a 3D multi rigid-body musculoskeletal model of a jerboa hindlimb to allow for insight into muscle functions that permit extraordinary locomotive function. Development of the model is followed closely by validation and uncertainty quantification to guide future study. By identifying the potential coordinated muscle activation patterns during jerboa motion, detailed relationships to the production and maintenance of agility and stability during high accelerations and quick directional changes can be developed. Ultimately, greater understanding of the interacting systems involved in movement production has vast application, from investigating disease, optimizing surgical intervention, developing robotic assistance, or even enhancing performance [2].

Chapter 2 : Methods

2.1 Specimen Preparation and Micro-CT Scanning

A female jerboa, 4 years of age at 51.5 g was sacrificed, fixed, skinned and eviscerated. A fatal dose of Ketamine/Xylazine cocktail at 50µl per 8mg of body weight was injected intraperitoneally. After confirming complete anesthesia, the jerboa received a transcardial perfusion of 1x Phosphate-buffered saline (PBS) followed by 4% paraformaldehyde (PFA). After perfusion fixation the animal was eviscerated, skinned and stored at 4 C in 70% Ethanol.

To visualize the jerboa skeleton without invasive dissection, the specimen was scanned using a microCT SkyScan 1076; Brukerm Kontich, Belgium. A microCT dataset of the skeleton was acquired at $(\sim 36\ \mu m)^3$ isotropic voxel resolution, with imaging settings of 50 kVp, 200 µA, 0.5 mm aluminum filter, 180° scan, $\Delta=0.5°$. In order to also study musculature, the specimen was equilibrated in 1% Lugol contrast; 1% I_2 2%KI in PBS 400 ml, at room temperature for 30 days. A microCT dataset of the contrast-enhanced specimen was then acquired at $(\sim 9\ \mu m)^3$ isotropic voxel resolution with imaging settings of 50 kVp, 200 µA, 0.5 mm aluminum filter, 180° scan, $\Delta=0.8°$. During scanning, the specimen was supported within a humidified environment. Images were reconstructed using NRecon (Bruker, Belgium) with a smoothing factor of one, ring artifact reduction factor of six, beam hardening correction factor of 40%, and with a dynamic range from 0.0 to 0.11 attenuation units for the initial $(\sim 36\ \mu m)^3$ scan and 0.02 to 0.2 attenuation units for the contrast-enhanced scan. Reconstruction of the files produced Bitmap Format (BMP) datasets which were later converted to digital imaging and communications in medicine (DICOM) images. Two datasets were acquired, one with visualization of bone before staining of the specimen (Figure 2.1), and another with visualization of muscle after staining (Figure 2.2). Owing to the length of the jerboa, the non-contrast scan featured anatomy from the skull to approximately the 6th cuboid of the tail. While the higher resolution contrast scan featured from the ribcage to the 6th cuboid.

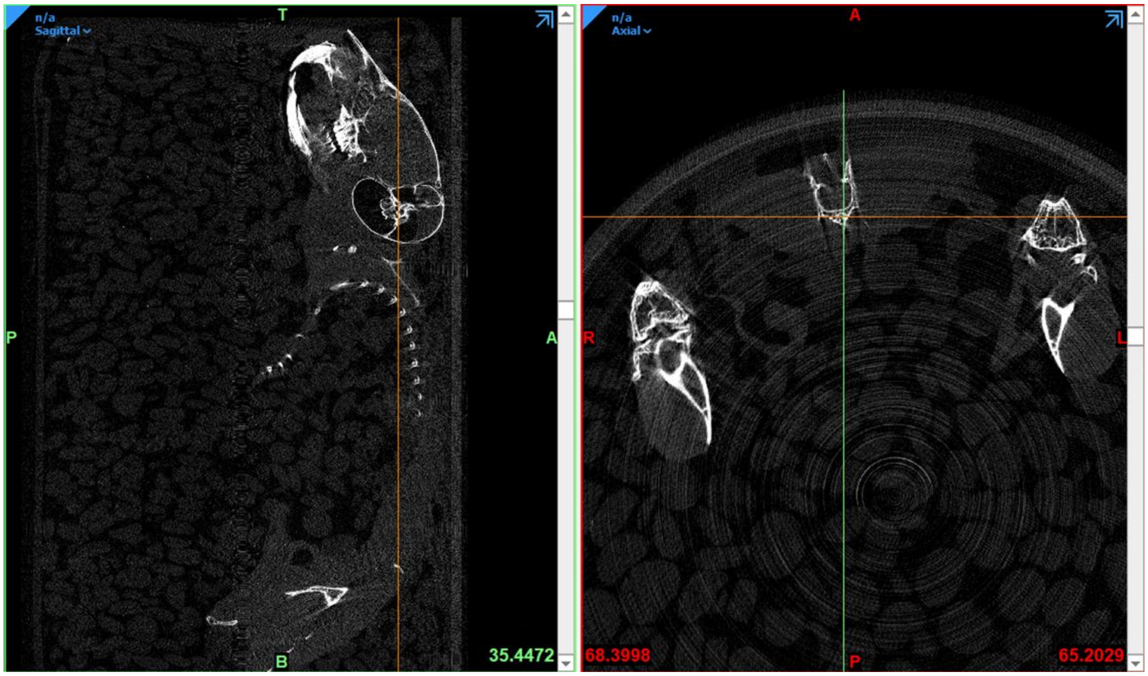

Figure 2.1: MicroCT scan of female jerboa, at 36 microns featuring sagittal (left) and axial (right) views without contrast enhancing Lugol stain.

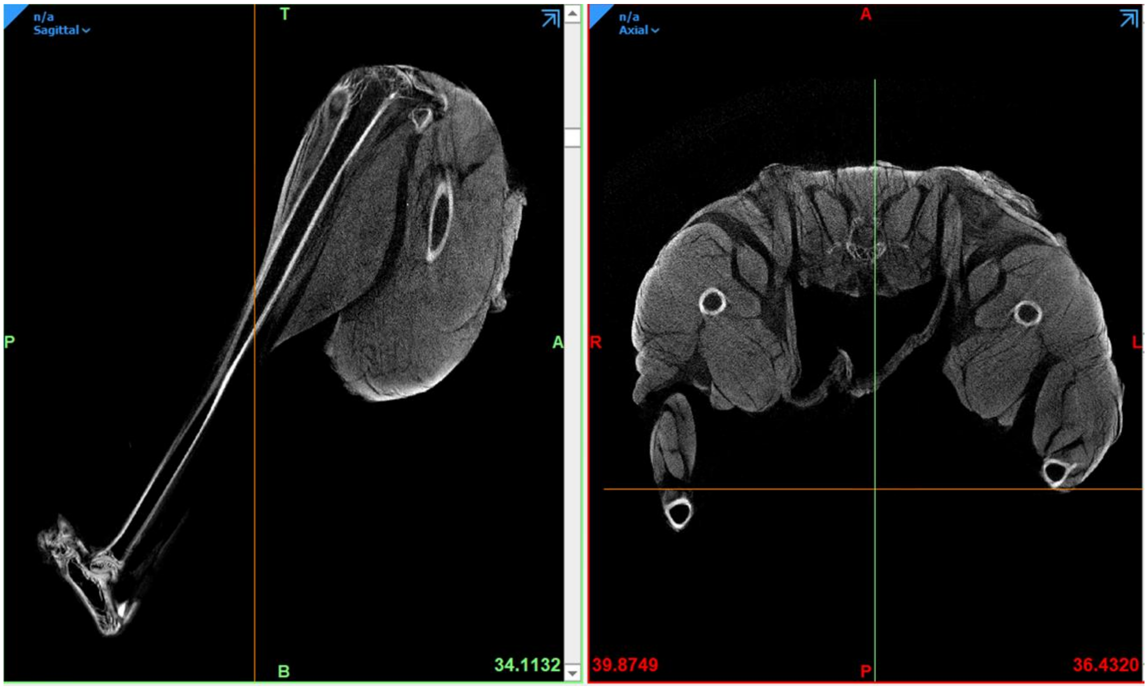

Figure 2.2: MicroCT scan of female jerboa, resized to 12 microns featuring sagittal (left) and axial (right) views with contrast enhanced Lugol stain.

2.2 Bone Segmentation

The use of microCT imaging allowed for high resolution analysis and 3D reconstruction of bones and muscle without destructive techniques. Bone was reconstructed in the low-resolution non-contrast scan as it allowed for the use of semi-automated tools to generate high accuracy geometries without the impediment of surrounding muscle and tissue. The software Mimics (Materialise Inc., Belgium) was used to visualize the reconstructed DICOM images and segment out geometries in the final form of standard triangle language (STL) files. Axial, sagittal, and coronal views were used, and with each bone of interest boundaries were defined to signify the start and end of the geometry in the three planes. After a region of interest (ROI) was established, a new mask is created with a thresholding technique that allows tissue within certain Hounsfield Units (HU) to be highlighted and previewed in 3D (Figure 2.3).

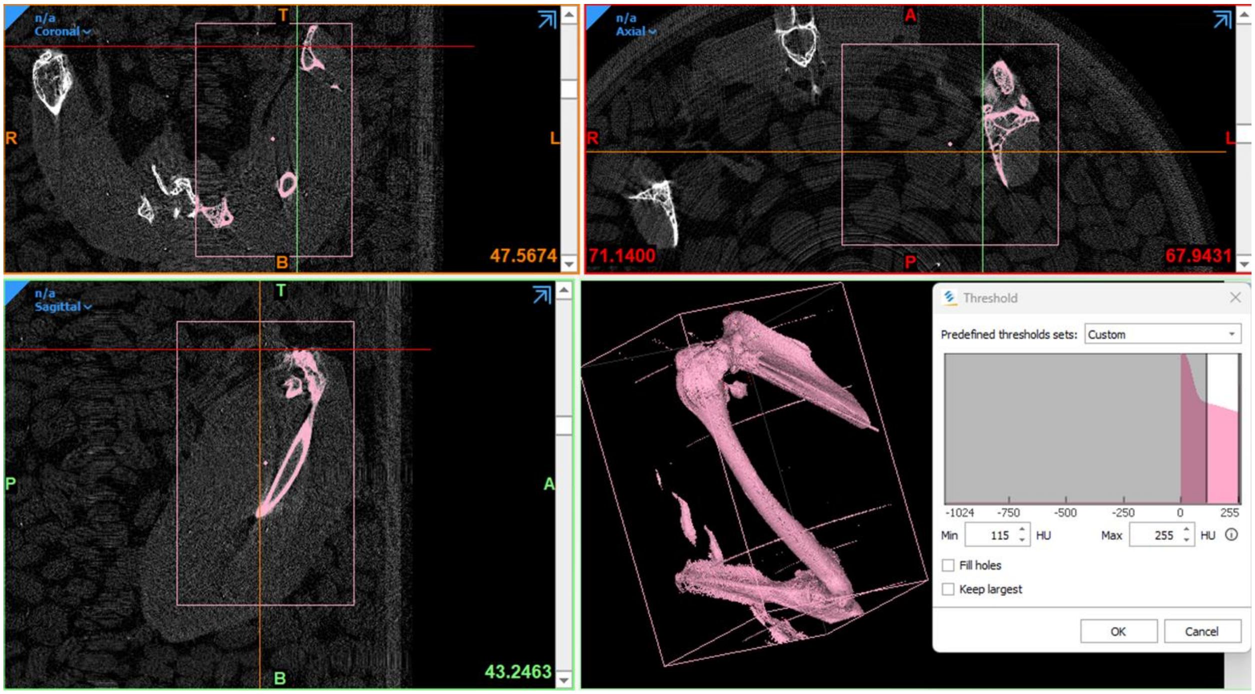

Predefined thresholds sets: Custom

Min 115 HU Max 255 HU

Figure 2.3: MicroCT scans after being processed with the software Mimics, which allow highlighting a region of interest selected in sagittal (left, bottom panel) , coronal (left, top panel), and axial (right, top panel) planes within a threshold range of 115 to 225 HU to isolate the right femur. The fourth view shows a visible 3D mask preview.

After completion of the semi-automated thresholding, manual segmentation was performed in order to completely isolate the geometry of interest (GOI) and correct artifacts created by under or over thresholding. Editing along every plane and slice ensured that gaps in GOI were filled and relevant anatomical landmarks or features were included. Discrepancies in the raw images or confusion in GOI boundaries were validated by inspection and reference of a juvenile *Jaculus jaculus* skeleton with a digital microscope.

2.3 Mesh Smoothing and Decimation

Segmentation of the microCT images was performed to delineate rigid bodies to be used in a computational model of jerboa anatomy. After manual segmentation, an interpolation of each voxel was generated in order to calculate the segment "part". Once the part was calculated, the mask was converted into a 3D mesh. To further ensure the closure of all gaps in the object, a wrap was performed on each geometry. The first step to a watertight mesh is ensured by wrapping the STL. The "smallest detail" parameters and gap closing distance in Mimics were chosen based on the size of the geometry and allocated memory. Once wrapping is completed, the part is exported out of Mimics as an STL to be smoothed.

Smoothing functioned as a final step for geometric reconstruction that ensured watertight meshes and triangular surface reduction for computation efficiency. Geometries were imported into MeshLab (ISTI-CNR Research Center, Italy) for the smoothing protocol. Wrapping objects often introduced additional surface material on the original part, thus the first step of smoothing included a "Laplacian" smoothing algorithm with iterations that varied based on the degree of wrapping and size of the geometry. Next, surface reconstructions and "taubin" smoothing allowed for a surface that could undergo remeshing. Finally, a two-step iso parameterization was used to reduce the number of triangles on the surface and decimate the mesh. After the above processes were completed, the finished mesh appeared like the example in Figure 2.4**.**

Validation of post segmentation processing and smoothing was done to ensure the prevention of over smoothing and degradation of anatomical landmarks. Processed geometries were reimported back into raw imaging data and reviewed in all planes to confirm consistent outline and overlap with raw CT data (Figure 2.5).

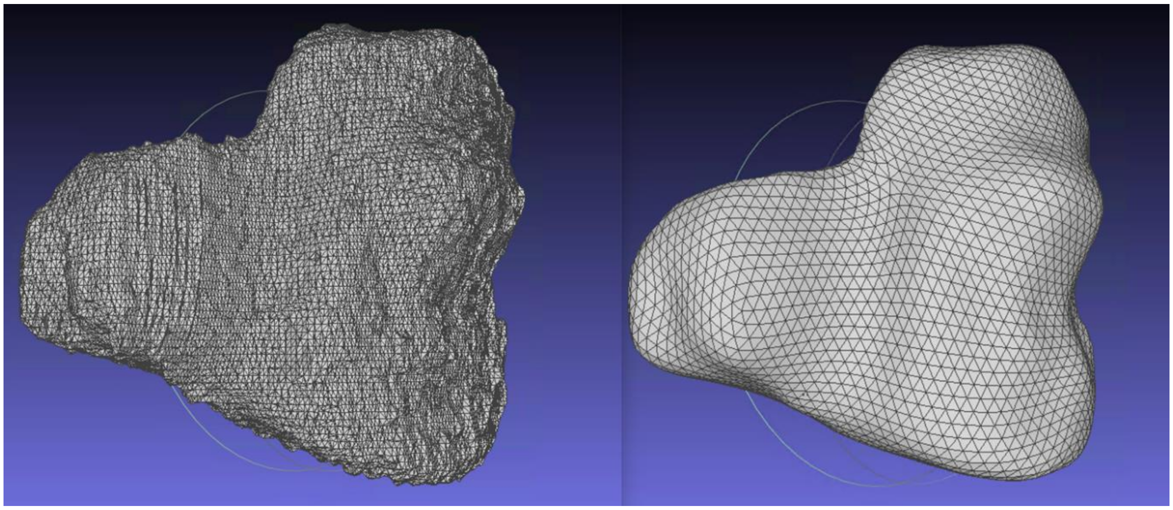

Figure 2.4: STL of the jerboa tibial plateau before (left) and after (right) smoothing, decimation and remeshing. This process is conducted on all geometries to allow post processing and efficiency of point spread during computational simulation by preventing over discretized geometries.

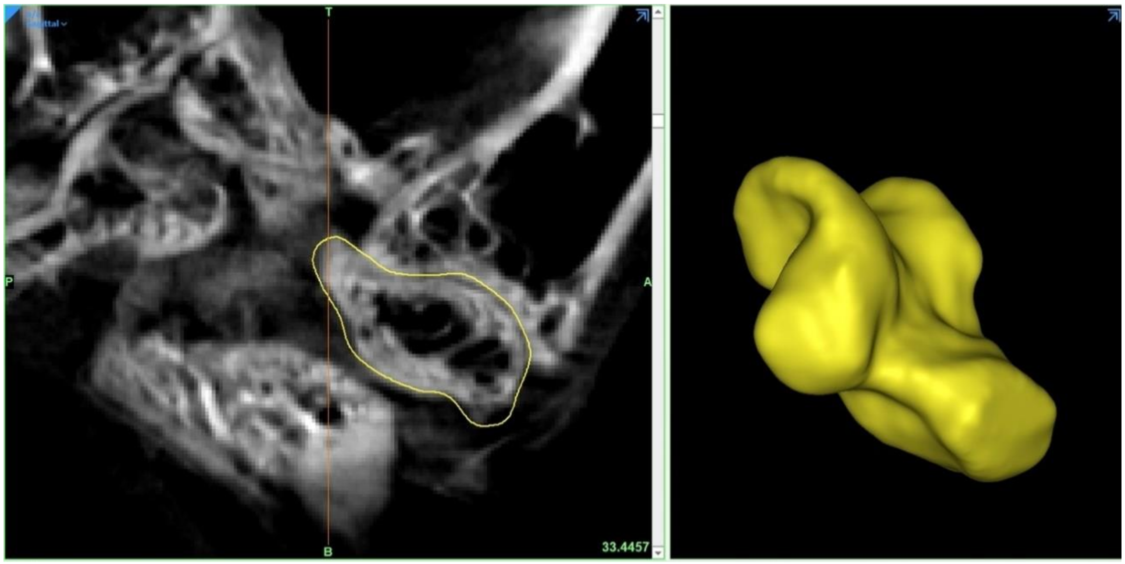

Figure 2.5: Confirmation of proper smoothing, transformation or post processing by importing a bone geometry and verifying the outline of the STL corresponds with the raw CT data.

2.4 Transformations

When performing muscle segmentation, efficiency and accuracy relied heavily on using bony landmarks and surrounding geometries as a reference and validation for muscle origins and insertions. To import bodies from the non-contrast scan to the contrast scan, translation and rotation of each geometry were calculated to account for changes in orientation of the specimen in the scanner between the two scans. To begin, a rough manual segmentation and wrap of the GOI was performed in the contrast scan. This geometry and the corresponding body from the non-contrast scan were both imported into Geomagic Wraps software (3D Systems, USA). After ensuring the contrast geometry was watertight, a least square fit algorithm was used to reorient the processed and smoothed geometry to be translated and rotated until the lowest surface mesh error is achieved (Figure 2.6). The alignment of the geometries was evaluated by use of a heatmap (Figure 2.7) and previous reimportation techniques (Figure 2.5). Owing to the fixation of the specimen, a few geometries in proximity allowed for the use of duplicate transformations. However, most bodies required their own transformations, resulting in a total of 10; from the non-contrast bone scan to the Lugol's stained muscle scan. Individual transformations from non-contrast to contrast can be found as 4x4 transformation matrices and corresponding Eulerian angles in Appendix A. Processed geometries were imported into the contrast-scan and the development of a master scan was created which allowed for all further mathematical calculations, such as transformations, to be conducted in a single scan rather than two.

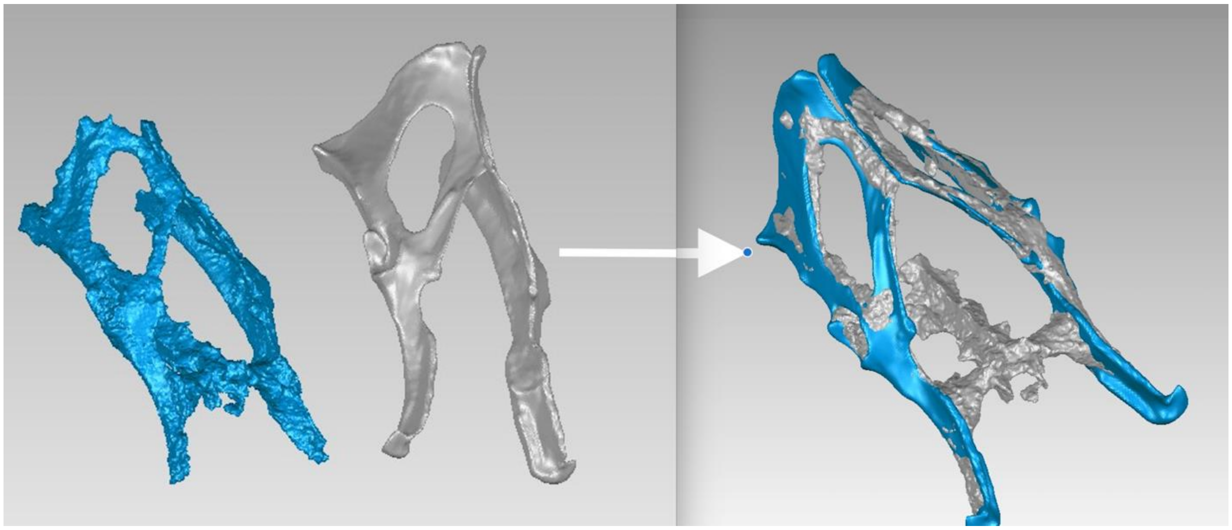

Figure 2.6: Geomagic least square fit of pelvis segmented in contrast and non-contrast scan in order to generate matrix of rotation and translation for unstained geometries.

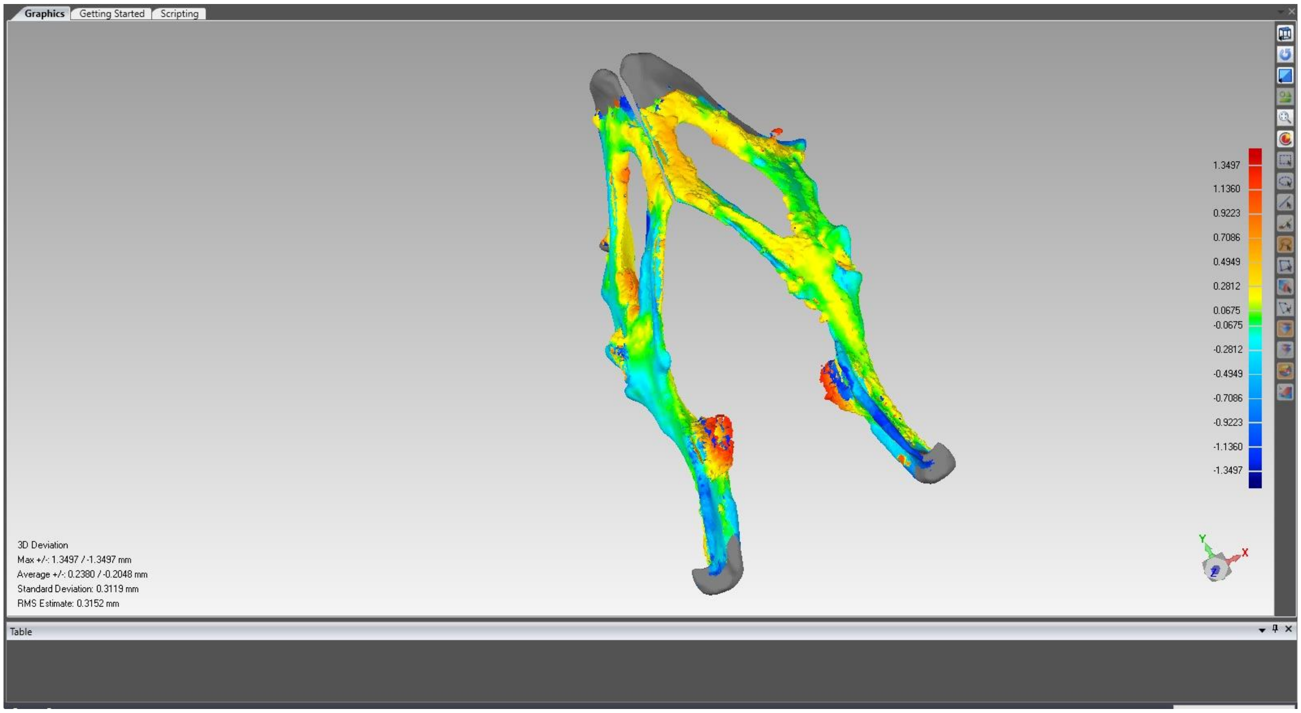

```
3D Deviation
Max +/-: 1.3497 / -1.3497 mm
Average +/-: 0.2380 / -0.2048 mm
Standard Deviation: 0.3119 mm
RMS Estimate: 0.3152 mm
```

Figure 2.7: Three-dimensional heatmap generated in geomagic after conducting a least-square fit of meshes from different scans. Heatmap quantifies differences in fitting between the two objects.

2.5 Muscle Segmentation

Segmentation and importation of transformed bone was followed by muscle segmentation. Complete and iterative manual segmentation was required for muscle meshes. Previous microCT characterization and segmentation of jerboa hindlimb muscles had not been done and thus identification of muscles was accompanied by close review of previous mouse hindlimb segmentation [25]. Due to the inherent anatomical differences between the rodent specimens, more species-specific information was needed. Thus, microdissections were performed and reference to detailed documentation of dissections of jerboa performed by Alfred Howell on various Dipodomys were used to confirm separation, size, path, and attachment points of muscle [26]. Muscle segmentation methods and results are detailed by Ravi-Embar [27].

2.6 Rigid Body Mass Properties

The rigid bodies constructed from the microCT images require the associated mass and inertial properties in order to allow for dynamics simulations. A male jerboa, aged 7 months and 4 days, weighing 57.9 grams was sacrificed by lethal injection of a Ketamine/Xylazine cocktail at 50μl per 8mg of body weight. Body segments were marked on the jerboa (Figure 2.8) passing through appropriate joint centers including surrounding skin, muscle and tissue. Separation of segments was based on a center of mass calculation approach rather than separation of tissue based on functional characteristics or contributions. Each separated segment was weighed on a fine scale and totaled to match the original specimen mass. A percentage mass was then calculated for each segment and used to scale the segments for a specimen weight of 51.5 grams (Table 3-1). It is important to note that the weight of the segment labeled “upper body”, refers to anything excluding the pelvis, tail and hindlimbs.

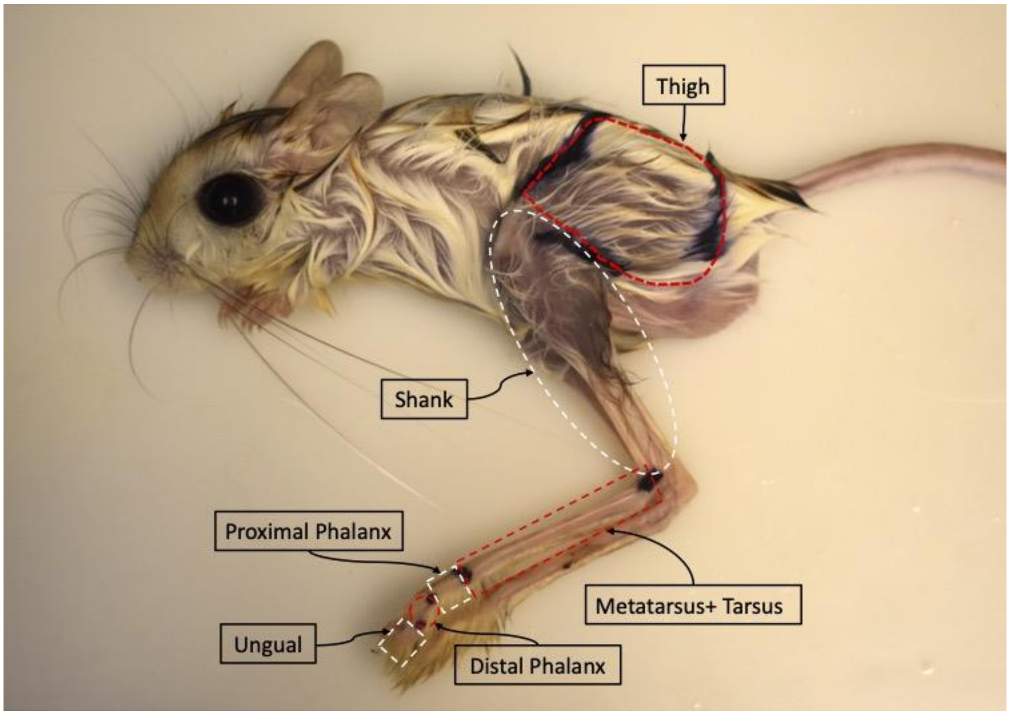

Figure 2.8: Body segments marked on jerboa before dissection and separation of segments for use in calculating mass properties and musculoskeletal modeling inputs.

To calculate center of mass and inertial tensor properties, the same regions of the hindlimb distinguished by previous dissection (Figure 2.8) were segmented out in the contrast CT scan. All tissue visible in the scan and exceeding the density threshold was included. Each region was wrapped, smoothed and decimated as detailed in Section 2.1 in order to allow for computational processing. The segmentation resulted in the regions seen in Figure 2.9. Adams View (Hexagon, Sweden), a multibody dynamics and motion analysis software, was used to process the segments. Before importing into Adams, each region was transformed based on rotations and translations generated for bone coordinate systems described in Section 2.6. Importing each geometry in its transformed state ensured that values for center of mass and inertial tensor were taken based on an origin defined for each geometry with respect to the BCS global coordinate state. This confirms the same values can be imported later into musculoskeletal modeling software without modification.

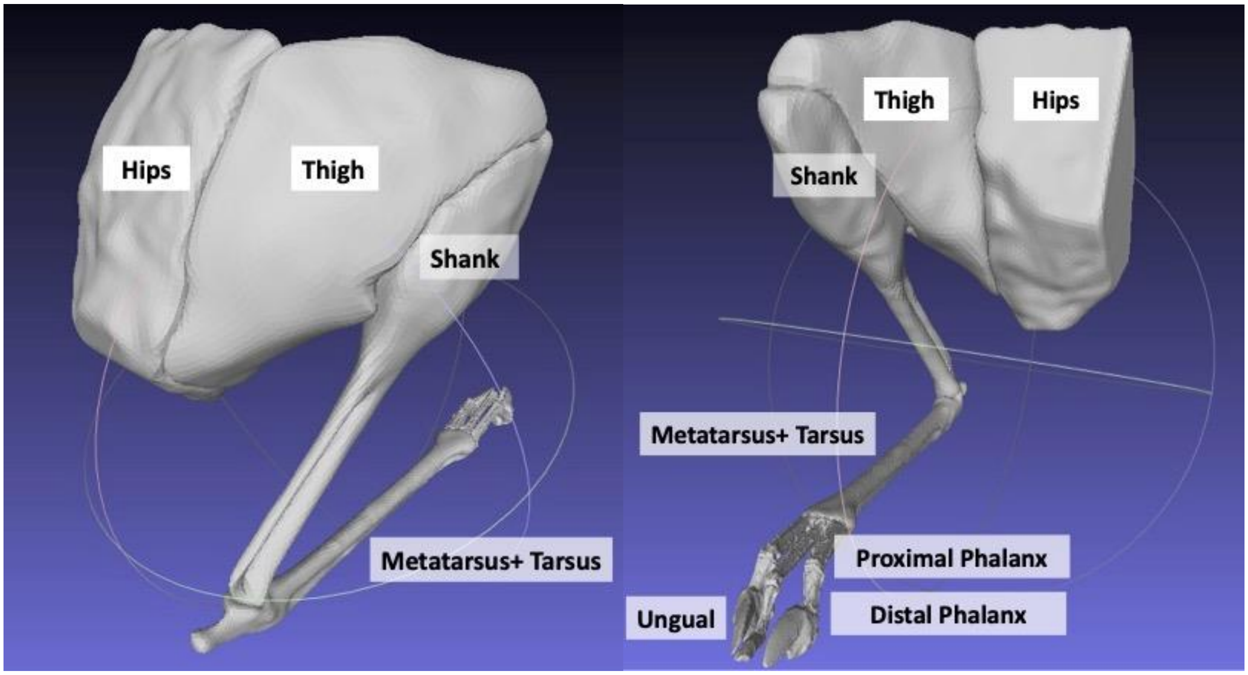

Figure 2.9: Segmented bodies in the hindlimb mimicking regions marked in Figure 2.8 to calculate mass and inertial properties for modeling inputs.

Bodies must be exported as STL ASCII from Mimics to be imported properly by Adams. A density of 1000kg/m^3 was assigned to the rigid bodies in Adams following previous biomechanics studies in jerboa and mice [20,25]. Adams then uses an iterative approach to calculate the center of mass and the corresponding inertial tensor along the principal axes. Mass is later used to describe the tendency to resist translation. The inertia tensor, a rotational 3x3 matrix, describes the tendency to resist changes in rotation due to the distribution of mass in the rigid body. The center of mass, which is a 3x1 vector, indicates the location of a point where all the mass should be concentrated [28]. Values for mass properties for each geometry can be seen in Appendix B: Model Parameters.

2.7 Bone Coordinate Systems

With rigid bodies and their corresponding inertial and mass properties, the preceding step would be to generate movement. To allow for movement between two rigid bodies, a joint is required. Building joints from two segments requires bone coordinate systems (BCS) that define the movement of one body with respect to the other. Relative movement of a joint here is assumed to be about a single point known as the joint center origin. Three axes were defined for each bone in order to provide movement corresponding to clinically relevant rotations or movements. The methods used coincided with those defined by the International Society of Biomechanics (ISB), previous rodent models and other human musculoskeletal models [6,13,29–31]. Anatomical landmarks on the bones were utilized to manipulate geometric bodies and create the BCS. BCS were generated primarily for bones in the hindlimb surrounding the hip, knee, ankle, metatarsal-phalanx and phalanx-ungual joints. BCS were also generated for other joints in the jerboa body to compensate for the effect of spinal curvature and movements caused by the conical CT pose. Creation of coordinate systems is noncommutative and explicit documentation of the order of operations below must be followed to ensure proper Eulerian rotations and transformations. Each axis of the coordinate systems is restricted to the orthogonality of the previously defined. Therefore, the order presented here follows previous models and ISB to ensure properly defined joints. All BCS were created in Geomagic Wraps. Anatomical points of interest used to generate the coordinates from the contrast scan perspective can be found in Table 2-1.

Beginning with a full pelvis, the origin was defined between the center of the left and right anterior superior iliac spines (LASIS, RASIS) as seen by ISB. Previous rodent models used the origin at the hip joint center, due to segmentation of only a hemi-pelvis, however with the use of a full pelvis, an approach more commonly seen in human models was used [31]. The z-axis is first constrained by selecting points on the LASIS and RASIS. Z is the vector from LASIS to RASIS pointing laterally. Points for the left and right posterior iliac spines (LPSIS, RPSIS) are selected and a plane is defined from the midpoint of the LPSIS and RPSIS to the previously defined left and right ASIS. The x-axis is then defined parallel to the plane pointing anterior/cranially. The y-axis is orthogonal to the previous two axes, pointing dorsally.

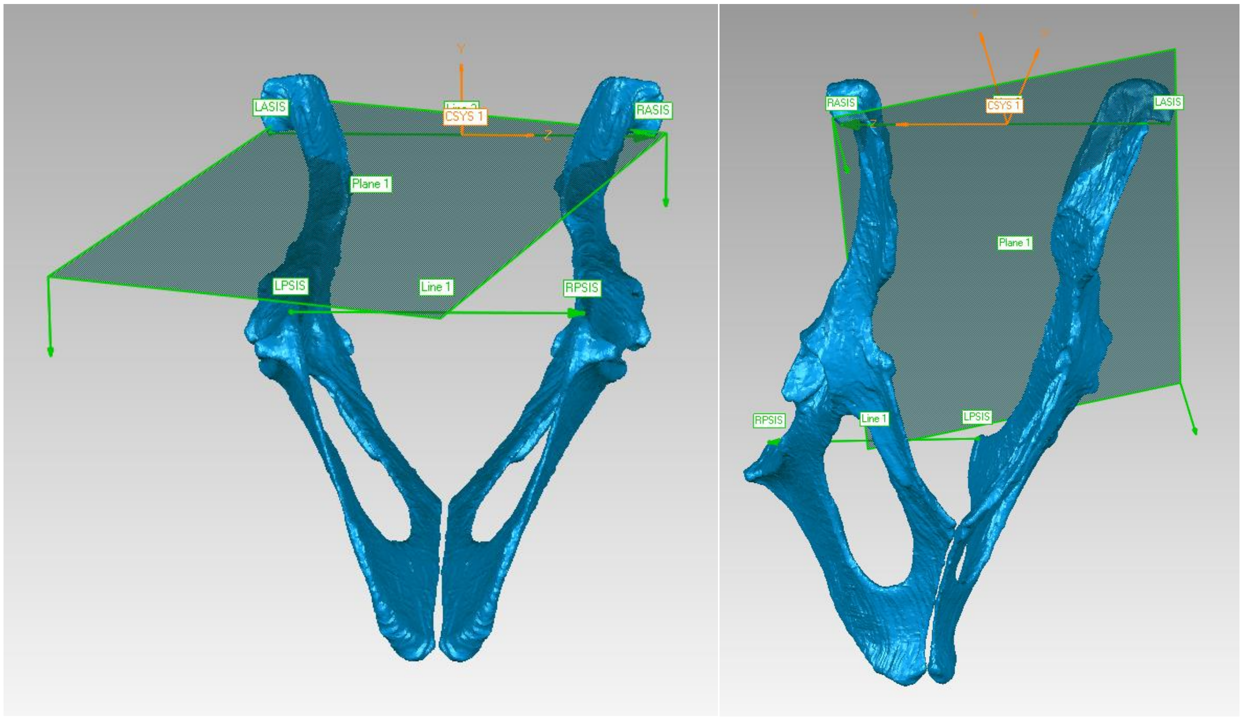

Figure 2.10: Pelvic coordinate system, with origin between ASIS, planes and points featured and defined by human ISB standards.

The origin of the femur is defined as the center of the femoral head (FHC), this can also be defined as the hip joint center (HJC). To find the FHC a sphere is fit to the portion of the head that contacts the acetabulum, and the center of the sphere is the origin. The y-axis is defined by the line between the HJC and knee joint center (KJC). The knee joint center is found by fitting a cylinder to surfaces of contact on the epicondyles (Figure 2.11). The center line defined by the cylinder is the knee axis. Surfaces on the epicondyles of the femur intersecting with the knee axis were selected and the midpoint between them is thus the KJC. From the previously obtained HJC and the KJC, the y-axis is the vector between them pointing proximally. The z-axis is defined as the knee axis pointing laterally and the x-axis is orthogonal to the previous two axes, pointing anterior.

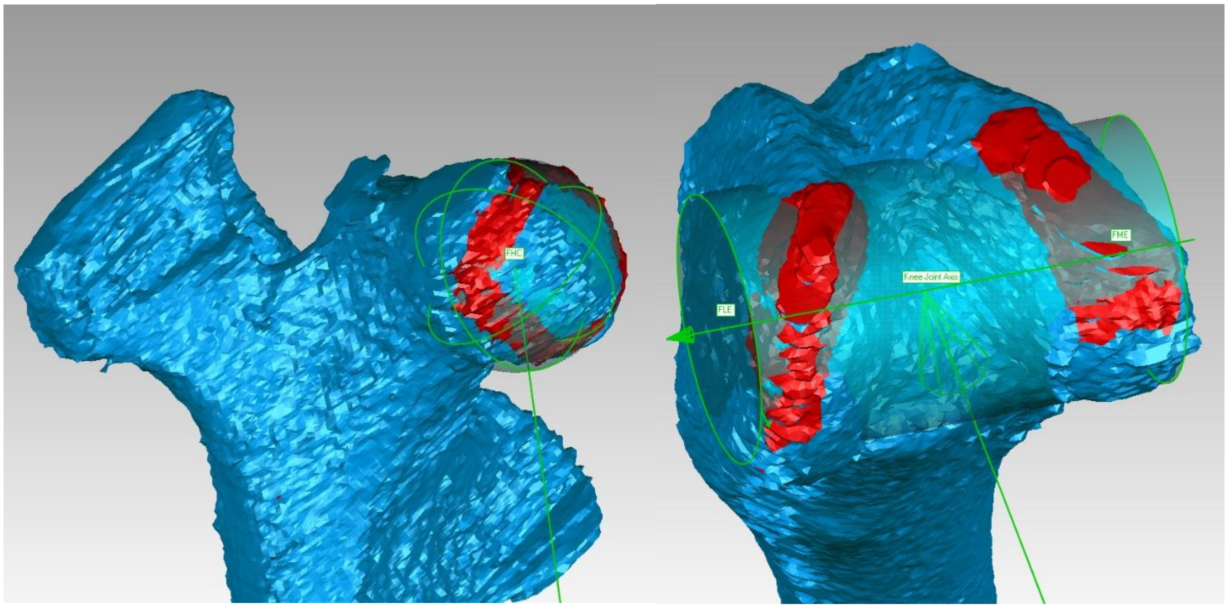

Figure 2.11: The femoral head (left) and condyles (right) with regions (red) selected to generate geometric shapes for the creation of bone coordinate systems.

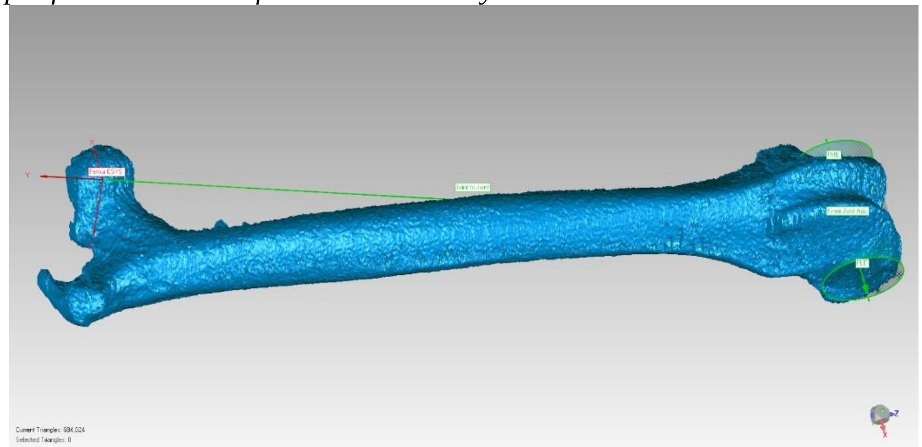

Figure 2.12: Overview of Femur after the creation of BCS, with origin of axes depicted at the center of the femoral head.

The origin of the tibia was defined at the KJC**.** Points for the right lateral and medial malleolus and right lateral and medial condyles (RLM, RMM, RLC, RMC) were defined. The z-axis is defined as the vector between RLM and RMM pointing laterally. A plane was created between the intermalleolar point (IMP), RMC and RLC (Figure 2.13). The x-axis is defined parallel to the vector normal to the plane, pointing anterior. The y-axis is orthogonal to both, pointing proximally.

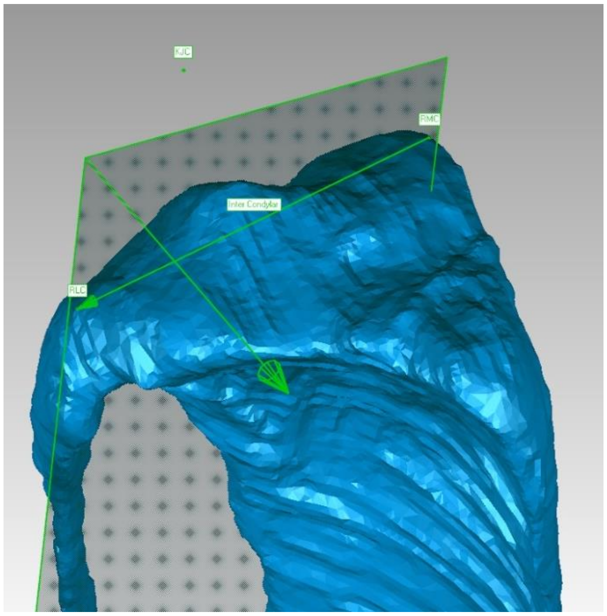

Figure 2.13 Tibial Plateau; displaying points chosen for condyles, development of the BCS plane and their proximity to the KJC.

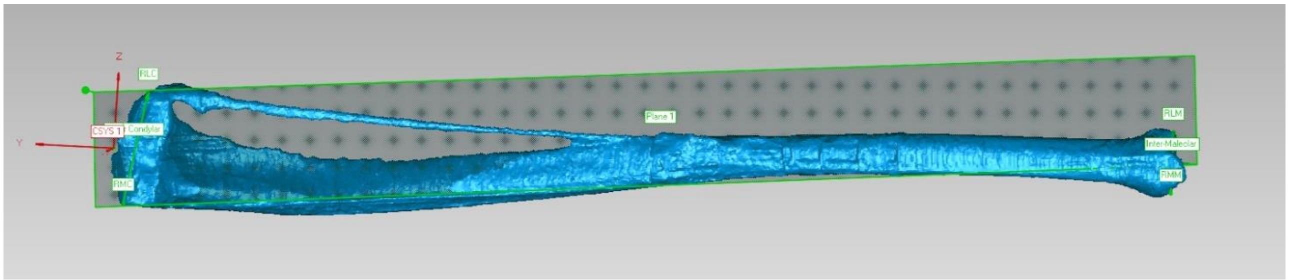

Figure 2.14: Tibia with BCS originating at the KJC and developed using points on the condyles and malleoli.

The origin of the ankle lies in the inter-talar point (ITP). Points for the medial and lateral extremity of the talus (MTP, LTP) are selected. This was done by fitting a cylinder to regions of the talus that make contact with the tibia. Then, by finding the model and line intersection with the cylinder, the MTP and LTP can be defined. From here the origin is the point in the center of the line that joins these points. The z-axis is defined as the line between the two previously defined points, pointing laterally. A point on the posterior extremity of the calcaneus (CAL) is chosen and a plane is defined between MTP LTP and CAL. The x-axis became the line parallel to this plane pointing cranially. The y-axis is orthogonal to both, pointing dorsally.

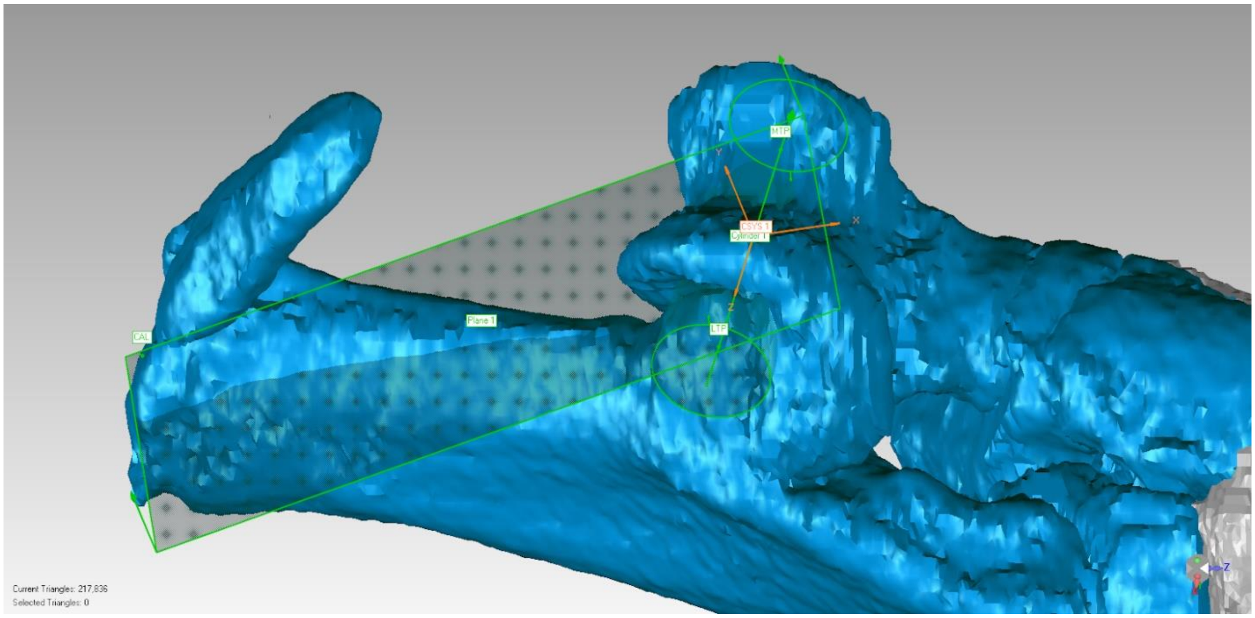

Figure 2.15: The ankle joint with the tibia hidden. Featuring points selected on the talus, and calcaneus as well as geometries between them to generate a BCS at the center of rotation between the talus and tibia.

For joints and bones distal to the ankle, all origins were found by fitting cylinders to the joint's rotational surface and finding the center between the line and model intersection of the cylindrical axis. The z-axis corresponded to the cylinder’s central axis pointing laterally. The x-axis was found from the origin of the distal joint to the proximal joint, pointing proximally. The y-axis is orthogonal to the two. These BCS were developed firsthand, following iterations of procedures described for other joints and similar phalanx joints in human and chimp models [8,9,31]. These joints were not defined in previous rodent models.

Table 2-1: Bone Coordinate System Anatomical Landmarks chosen in contrast microCT

Bone/Joint	**Anatomical Landmark**	**Contrast Location (mm)**	**Abbreviation**
Pelvis	RASIS	27.3243, -53.3722, 39.8616	Right Anterior Superior Iliac Spine
	LASIS	12.5951, -53.7153, 39.7456	Left Anterior Superior iliac Spine
	RPSIS	24.7760, -39.0550, 22.2286	Right Posterior Superior Iliac spine
	LPSIS	14.7149, -39.1515, 21.9118	Left Posterior Superior iliac spine
Femur	FHC	26.2067, -42.8694, 32.8600	Femoral Head Center
	FME	34.4271, -44.9348, 55.8302	Femoral Medial Epicondyle
	FLE	38.5617, -44.5518, 55.4030	Femoral Lateral Epicondyle
	KJC	36.4945, -44.7433, 55.6166	Knee Joint Center
Tibia	IMP	33.4860, -19.3610, 18.2545	Inter-Malleolar Point
	RMC	34.0416, -43.2556, 56.1916	Right Medial Condyle
	RLC	38.5590, -42.4094, 55.3736	Right Lateral Condyle
	RMM	32.1713, -19.5773, 18.2775	Right Medial Malleolus
	RLM	34.8006, -19.1447, 18.2315	Right Lateral Malleolus
Ankle			
	LTP	34.6197, -19.8706, 17.5607	Lateral Extremity of Talus
	MTP	32.3561, -20.0586, 17.4313	Medial Extremity of Talus
	ITP	33.3487, -19.9762, 17.4880	Inter-Talar Point
	CAL	34.0515, -20.7555, 12.7449	Posterior Extremity of Calcaneus
Metatarsal			
	MT_P6_L	31.9267, -8.0186, 50.7661	Medial and Lateral Points on MT
	MT_P6_M	30.5967, -8.3697, 50.8709	“”
	MT_P4_M	29.2898, -8.1585, 51.4466	“”
	MT_P4_L	30.2265, -8.1067, 51.5352	“”
	MT_P2_L	27.7344, -8.0640, 49.9965	“”
	MT_P2_M	29.1242, -8.4028, 50.4192	“”
	P6M	29.2467, -6.9428, 58.2500	Digit P6 Medial Point
	P6L	30.4013, -6.9501, 58.3366	Digit P6 Lateral Point
	P4M	27.9563, -6.0008, 60.6600	Digit P4 Medial Point
	P4L	27.0810, -6.0844, 60.5454	Digit P4 Lateral Point
	P2M	25.7275, -6.6110, 57.2509	Digit P2 Medial Point
	P2L	26.7954, -6.3499, 57.5288	Digit P2 Lateral Point
	P1M	24.7007, -3.6966, 59.1952	Digit P1 Medial Point
	P1L	25.4638, -3.2792, 59.2634	Digit P1 Lateral Point
	P3M	26.4756, -2.5650, 62.4764	Digit P3 Medial Point
	P3L	27.1474, -2.6281, 62.6736	Digit P3 Lateral Point
	P5M	29.0455, -3.5705, 60.2020	Digit P5 Medial Point
	P5L	29.9252, -3.8278, 60.6025	Digit P5 Lateral Point
	C1P	25.2351, -3.0589, 63.6273	Tip of Claw 1
	C2P	26.0237, -2.8698, 65.4489	Tip of Claw 2
	C3P	27.4357, -3.1752, 63.9708	Tip of Claw 3

For the patella, the origin is located at the distal pole of patella, medial and lateral points are chosen, as well as a proximal pole. The y-axis is defined from distal to proximal, then the x-axis was defined from medial to lateral. The z-axis is orthogonal to both. This portion of the procedure was not created to model motion, but simply for visual appearance of non-moving parts. BCS were defined for bones along the lumbar spine, thoracic spine and skull for the sake of adjusting the skeleton away from the conical CT pose, but not for anatomically relevant movement. Cylinders were fit to the inferior IVD and the origin was defined at the center of this cylinder. Z-axis points laterally based on the cylindrical axis. X-axis goes from inferior to superior IVD center. Y orthogonal to both [29,32].

The development of each axis and coordinate system of the individual bone segments was followed by alignment of the coordinate axis to the globally defined coordinate axis in Geomagic to allow for accommodation of joint creation in OpenSim (OS) musculoskeletal model construction workflow. All bodies were exported in the globally transformed state and transformation matrices were calculated and used to move geometries post upload. All the above BCS can be viewed in their master files as listed in the instructions of Appendix A.

2.8 Joints and Range of Motion

Following the definition of relevant axes and points of rotation between bones; minimum and maximum joint angles were found on the left hindlimb of skinned specimen JJ0198, male aged 5 years and 4 months. Joint range of motion ensures that any data output from the musculoskeletal model only corresponds to physiologically possible movements. The hip, knee, ankle, meta-phalangeal and ungual joints were each articulated independently in the defined degrees of freedom. The hip was moved in three degrees of freedom corresponding to axes defined for the BCS; flexion-extension, adduction-abduction, and internal-external rotation. In the model, the knee was constrained as a functional hinge joint, but was generated with three degrees of freedom; flexion-extension, varus-valgus, and internal-external rotation. Similar approaches were taken for the remaining distal joints with a particular focus on flexion and extension. For each range of motion trial, the joint of interest was moved until passive restraints such as bone, muscle and ligaments prevented the joints from being moved any further. This was done while surrounding joints were held at relaxed states to best ensure that tissue was not being stretched past its passive restraint and altering the corresponding range of motion. Video was recorded of each trial and processed in ImageJ (U.S. National Institutes of Health, Bethesda, MD, USA) to find the change in joint angle measured from the stance phase. Angles were calculated by picking proximal and distal joint centers to the joint of interest. Joint centers were picked manually on the still shots of the video based on anatomical region and approximated bony landmarks. As corroboration, video was also digitally scaled and overlaid with OS model joint range of motion to capture the alignment of measured angles. The model was also analyzed through the prescribed joint range of motion to ensure no bone penetration or discrepancies were observed. All joints for which video data was not collected and degrees of freedom that were not explicitly defined were also provided limits based on visual model interpretation and the start of inaccurate bone overlap.

2.9 Muscle Architecture

To allow for the potential of collecting and calculating architectural data. A female jerboa, specimen JJ0998, mass 56.4 grams and age three months was sacrificed as detailed in Section 2.1. The specimen was secured in a rig that ensured hindlimb stance phase was upheld to maximize the potential for achieving optimal fiber lengths before being injected for perfusion fixation. After the fixation, the specimen was skinned and eviscerated. Joint angles were measured at the hip, knee, and ankle using a goniometer. A careful and detailed dissection was performed to remove all muscles that were previously identified in the imaging segmentation. Throughout the dissection, high magnification images were taken of attachment sites and muscles were excised from origin to insertion. After removal of all muscles in the hindlimb, bone segments were measured using a caliper and imaged as well. For each muscle-tendon unit (MTU), muscle belly (Lm) and tendon length (Lt), if applicable, were collected with calipers and from images using ImageJ. Mass was weighed on a fine scale initially after excision and again after being put in a desiccator to achieve a dry weight. Both muscle belly mass (Mm) and tendon mass (Mt) were collected by first weighing the MTU and then weighing the belly after removing all external tendons. Purposes of the dissection included image segmentation corroboration and muscle architecture measurement and data can be accessed by viewing Appendix A: Accessing the Database.

2.10 Muscle Attachment Sites and Wrapping Surfaces

In addition to the embedded hill-type model that uses contractile parameters as inputs, OS utilizes attachment sites, via points (VPs) and wrapping surfaces to model muscles. Muscles and tendons are represented as an MTU. Muscle and tendon attachment sites are approximated by importing muscle geometries and bone geometries into Geomagic wraps and manually selecting the centroid of the attachment point. Muscles with large attachment points that encompassed a large volume such as BF and Gmax were modeled using multiple MTUs, and therefore multiple origin and insertion sights (Figure 2.18). For muscles with very tendinous insertion such as those that attach distal to the talus, tendon could not be visualized in the microCT and therefore insertion sights were estimated according to bony landmarks and then corroborated with dissections conduction as described in Section 2.9 and published literature[26]. Attachment sites selected on the bone were done with reference to the coordinate system of the Lugol-stained scan. To use these points in OS, transformation matrices for each geometry from CT to OS were generated similar to Section 2.3. These transformation files can be found linked in Appendix A: Accessing the Database.

For many muscles, origin and insertion sights alone were not sufficient to capture complex muscle lines of action that could be caused by fascia sheets constraining muscle path along bone or due to distribution of muscle mass. Muscles can follow complex paths over multiple joints and a variety of curved surfaces. Thus, the use of varying VP locations based on segmentation and dissection was used to affix the path of muscles to bone. This was true for muscles such as the PLANT, TA, EDL, and FDL. For more complex lines of action, geometries such as cylinders, ellipses and spheres called wrapping surfaces were created by manipulating muscle and bone geometries in Geomagic and later confirming range of motion and muscle path throughout the joints range of motion in OS. The above ultimately allows the model to more accurately reflect muscle moment arms, force production and the operating lengths of muscles. Examples of a wrapping surface can be seen in Figure 2.16. More detailed information about the construction and development of attachment sites, wrapping surfaces and VPs for each muscle is given by Ravi-Embar [27].

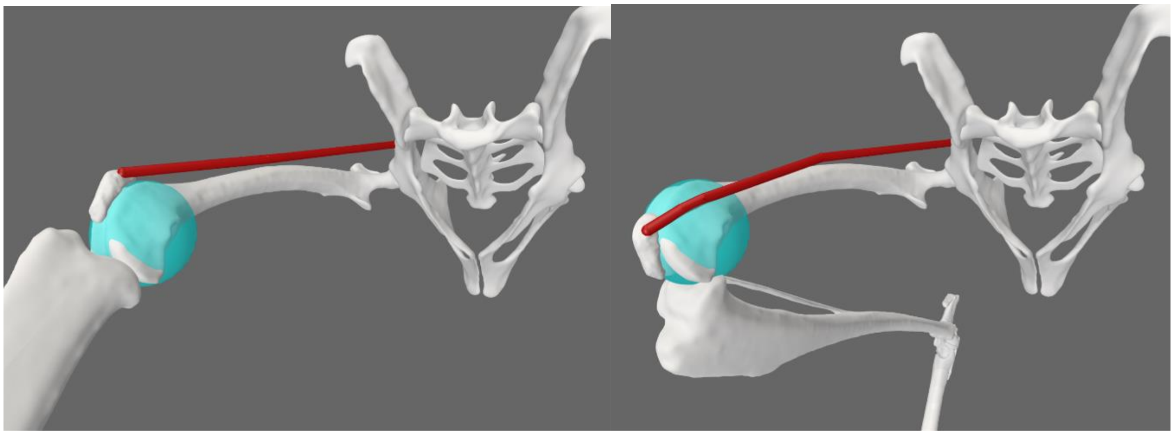

Figure 2.16: MTU of Rectus Femoris, origin at the pelvis and insertion on the proximal pole of the patella, with spherical "quads" wrapping surface preventing MTU penetration of femoral epicondyles. The left pan shows knee extension, and right pan shows knee flexion, where via point can be identified at the center of MTU path.

Figure 2.17: An isolated segmentation mesh of the RF in which MTU origins, insertions, and via points were modeled from.

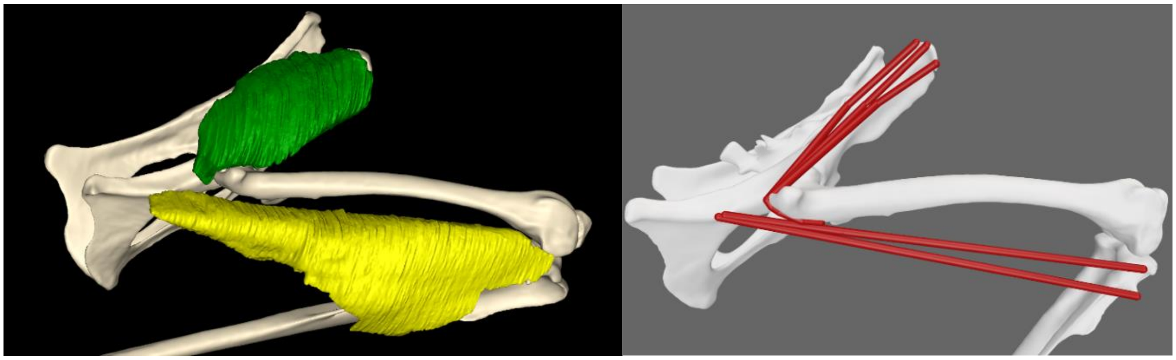

Figure 2.18: Gluteus Group and Biceps Femoris Posterior displayed in segmentation meshes (left) and corresponding MTUs from origin and insertion (right). The broad origin or insertion of these muscles warranted multiple MTUs to represent each muscle.

2.11 MATLAB API Construction

Development and construction of the model followed the use of an application programming interface (API) in MATLAB (MathWorks, USA). The program relied heavily on the organization of previously collected raw data into a shareable, editable google drive sheet which was downloaded and read by the code to supply the appropriate parameters while constructing the code. Previous OS models were written in XML, which involved repetitive syntax and proved to inhibit ease of public interpretation and access. The MATLAB API used built-in functions included in OS and the entirety of the code is available in Appendix C: JerboaModelBuilder.m Code. Before using the API, a package was downloaded to allow MATLAB (2022a) to interface with the latest version of OS (4.4). Appropriate packages and libraries were imported as seen in Section 1.1 of the code. An open model was declared and properties such as units, gravity, name of the model and the ground were defined. Here the units were defined in meters. It is important to note, changing the "set_length_units" did not result in any change in the model visualization or unit conversion, but rather functioned as a cue for the model user later. Thus, it is important to note that all geometries and points of interest were required to be entered in units of meters. In Section 1.3, all raw data and processed points are gathered and read by the code through the editable google excel sheet. The latest version of this sheet can be found by accessing Appendix A: Accessing the Database or directly in Appendix B: Model Parameters.

After all the data uploaded by the code into tables, the construction of the bodies was required. Section 2.1 of the code features a "for loop" that allows the creation of all bodies without any reliance on naming and is automated based on any changes in the sheet. An "if" statement was also used for geometries that were given multiple meshes, to allow for adding meshes based on the number included in the sheet. Later development of the code required recalling body variables that were previously created as a string variable. However, use of the "for loop" did not allow for explicit variable names to be defined. Thus, a built-in OS "bodylist" was called upon and later sifted through to compare to a list in the google sheet creating the correct order of variables when defining joints. The definition of joints initially only involved a short loop as seen in Section 2.2.4. Each joint was created using a "customjoint" that allowed for the input of generalized coordinates to describe how the child body moves with respect to parent body. This required the definition of six independent spatial axes. To begin child bodies were moved to the appropriate positions by being translated using the "LocationinParent" and "OrientationInParent". This implemented predefined bone coordinate systems embedded in the geometries and spatial transformations to move the child bodies from their origin to the location required for the position of the joint. The joint was finalized and later the default configuration for joint range of motion and stance phase was input. After joints were created and visualized with the OS Graphical User interface (GUI), joint penetration and discrepancies were identified to initiate adjustments. All joints in Section 2.2.4, excluding the patella-femoral and knee joint, were allowed rotation only. Meaning the joint center remains fixed with respect to the parent body during joint motion; as was the case in prior studies[8,11,14,28]. For the knee joint, using only rotation resulted in large amounts of bone penetration at extremes of joint range and did not allow for physiological motion of the tibia with respect to the femur. In Section 2.2.1, a "simmspline" function was used in order to define a function of tibial translation with respect to the joint angle rotation. This was done to prevent limitation or underestimation in joint ROM and therefore affect muscle operating lengths[28]. This function was adapted by observing the functions developed in previous models with knee joint functions and modifying the points based on video data described in Section 2.9, following tibial translation during knee flexion and extension. These functions were developed in all translation axes for the tibia and were also based on reducing bone penetration and preserving the physiological joint space.

Muscles such as the knee extensors were given insertion points on the patella, therefore without patellar movement these muscles would serve no function. Previous human models extended these muscle insertions with the patellar tendon and inserted them on the tibia which bypassed the need for a moving patellar joint. However, this was difficult due to the jerboas flexed knee stance and inability to visualize tendon in the microCT. Therefore, a similar method to the knee was used for the patellar joint and was created in Section 2.2.2 of the code. This section defined additional translation in *x* and *y* directions. The patella's movement could then be later constrained to the movement of the knee joint through a coordinate coupler as seen in 2.2.5. These points were also based on bone penetration and video data observation.

Finally, the addition of muscles was created similarly to that of bodies. In Section 3.1, muscles are defined, and dummy parameters are given based on the google sheet for contractile properties. Later path points were defined based on previously calculated and transformed points. Section 3.3 and 3.4 were used to define wrapping surfaces for muscles also using the data provided in the sheet. Point discretization appeared to decrease for many muscles when using cylindrical surfaces. The WrapCylinder.cpp has a 2-mm gap between segments on the surface hard coded into the class, and due to the scale of the jerboa this caused discrepancies in some wrapping. For many muscles, in particular the knee extensors, this was resolved by using spheres instead of cylinders to wrap. Section 3.5 lists the muscle groups based on previously defined functional groups for humans and mice to allow easier access to each force production. The last step involved updating the marker set, finalizing the model connections, and printing the .osim file to open in OS.

2.12 Uncertainty Quantification and Sensitivity Analysis

There was uncertainty in the accuracy of various parameters of model inputs, and thus conducting an analysis to quantify the level of robustness of the model by wavering values and observing the effects on results was important. Here muscle paths/attachment sites and wrapping surfaces were modified based on uncertainty in location, quantity or size. The identified degree of uncertainty was a result of many factors such as segmentation, dissection and previous models. The analysis was conducted on 11 muscles (LG, PLANT, TA, RF, VL, VM, SM, ST, BFA, AB, AM) with varying changes that can be viewed in Table 2-2. Muscles from each functional group/region of the hindlimb were picked for the sensitivity analysis, excluding ankle evertors and hip rotators due to overlap with the structure or similarity in changes to other muscles already selected. The PLANT and LG were isolated particularly due to their working contributions during vertical leaping identified in a previous study [20]. Adjustments to attachment points are described as cranial (CRAN; towards the skull), caudal (CAUD; towards the tail), proximal (PROX; closer to the center of the body), distal (DIST; further from the center of the body), medial (MED; towards the midline of the body), and lateral (LAT; away from the midline of the body). Accompanied with this is a distance in the defined direction. VPs were both moved and removed. Wrapping surfaces were either increased or decreased by 10% of their original diameter or removed completely.

All changes were made independently and resulted in multiple MTUs to be analyzed simultaneously. Changes in attachment points were acquired in Geomagic by generating spheres at the center of original attachment points with radii corresponding to the amount of uncertainty defined by previously analyzed raw data and literature [26]. Points were then picked between the overlap of the surface of the sphere and bone surface geometry. This was repeated for all muscles of interest with varying degrees of change and culminated in a duplicated sheet of the original “JerboaSim” model. For the removal of points, attachment was deleted between origin and insertion. Changes to wrapping were made by adjusting radii in the script as well. Contrast points chosen in Geomagic were transformed to OS coordinate systems using a developed MATLAB script that sifted each point for the correct body transformation and output an organized list of the transformed points.

To observe all the changed MTUs together a duplicate script of “JerboaModelBuilder " was created; “JerboaSensitivityAnalysis”, to ensure no models were overridden. MTUs could be isolated and plotted in OS against the joint angle and moment arm of interest. These plots were exported as .txt files and plotted in MATLAB using “Sensitivity_Plotter.m”.

Table 2-2: Adjustments selected for sensitivity analysis of attachment points and wrapping surfaces of muscles within the jerboa hindlimb musculoskeletal model.

Muscle	Point and Wrapping Adjustment
LG	**Origin**: CRAN, CAUD, DIST, PROX: 0.5 mm **Insertion:** CRAN, CAUD: 0.5 mm **Wrapping**: 10% the original diameter
PLANT	**Origin**: CRAN, CAUD: 0.5 mm **Insertion**: PROX, DIST: 0.5 mm **Via**: VP1: CRAN, CAUD: 0.5mm. VP2-9: removed **Wrapping**: 10% the original diameter
TA	**Origin**: Along Tibial ridge: 1.25 mm **Insertion**: PROX, DIST: 1 mm **Via**: VP2: MED, LAT 0.5 mm. VP 3-4: removed
RF	**Origin**: CRAN, CAUD: 1 mm **Insertion**: PROX, DIST: 0.75 mm **Via**: removed **Wrapping**: 10% the original diameter
VL	**Origin**: PROX, DIST: 1 mm **Insertion**: MED, LAT: 0.75 mm **Via**: removed all **Wrapping**: 10% the original diameter
VM	**Origin**: PROX, DIST: 1 mm **Insertion**: PROX, DIST: 1mm **Wrapping**: 10% the original diameter
ST	**Origin**: CRAN, CAUD: 1 mm **Insertion**: CRAN, CAUD: 1 mm **Wrapping**: removed
SM	**Wrapping**: 4 wrapping surfaces removed independently
BFA	**Origin**: CRAN, CAUD: 0.5 mm **Insertion**: CRAN, CAUD: 1.5 mm **Via**: removed **Wrapping**: removed
AB	**Origin**: CRAN, CAUD: 1.5 mm **Insertion**: LAT: 1 mm
AM	**Origin**: CRAN, CAUD: 1 mm **Insertion**: MED, LAT: 1 mm **Wrapping**: 10% the original diameter

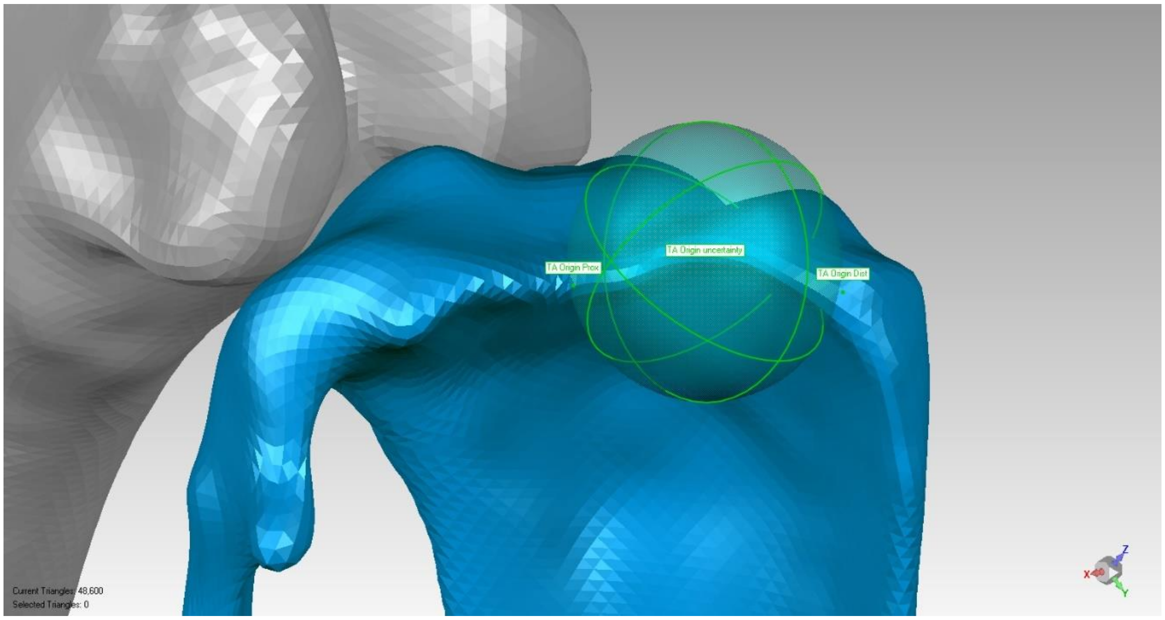

Figure 2.19: Sphere generated at the ridge of the tibial plateau with a diameter of 2.50mm. The center of the sphere is the original origin of the TA, and the outline of the sphere allows for new points to be chosen 1.25mm away but on the surface of the body.

Figure 2.20: OpenSim model with two TA MTUs. Both feature the same origin and insertion but one MTU (top) has two via points removed to observe effects in moment arm results at ankle ROM.

Figure 2.21: Three TA MTUs spanning different origins within uncertainty bounds to analyze moment arm effects.

Acknowledgements

I'd like to acknowledge Dr. Ceri Weber from the UC of San Diego biological sciences department for conducting sacrificial techniques in the section titled "Specimen Preparation and MicroCT scanning". Additionally, I'd like to acknowledge Erica Gacasan at UC of San Diego Bioengineering department for the imaging described in the section "Specimen Preparation and MicroCT Scanning". Pranav Ravi-Embar is acknowledged for initial segmentation, grouping and iteration of muscle Segmentation. Acknowledgements to Dr. Kimberly Cooper from the UC of San Diego biological sciences department for regions marked as seen in Figure 2.8. Finally, I'd like to acknowledge Dr. Juri Miyamae and Dr. Talia Moore from the University of Michigan at the EMBir Lab for the detailed dissections in this chapter.

Chapter 3 : Results

3.1 Model Construction

Segmentation procedures were conducted separately for all bones in the right hindlimb and lumped bodies in the upper body for a total of 47 individual segmentations. The hindlimb was separated into the pelvis, femur, tibia, calcaneus, talus, tarsals, cannon bone, proximal phalanges, distal phalanges, unguals and sesamoids. For the remainder of the specimen, the skull, sacrum, lumbar vertebra and first three cuboids were segmented separately. The cervical spine, thoracic spine, ribcage and forelimbs were segmented as a single geometry with no separation.

Parameters for smoothing and decimation were adjusted depending on the size and shape of each bone or body. Figure 3.1 features all raw segmented bodies, with a focus on the hindlimb.

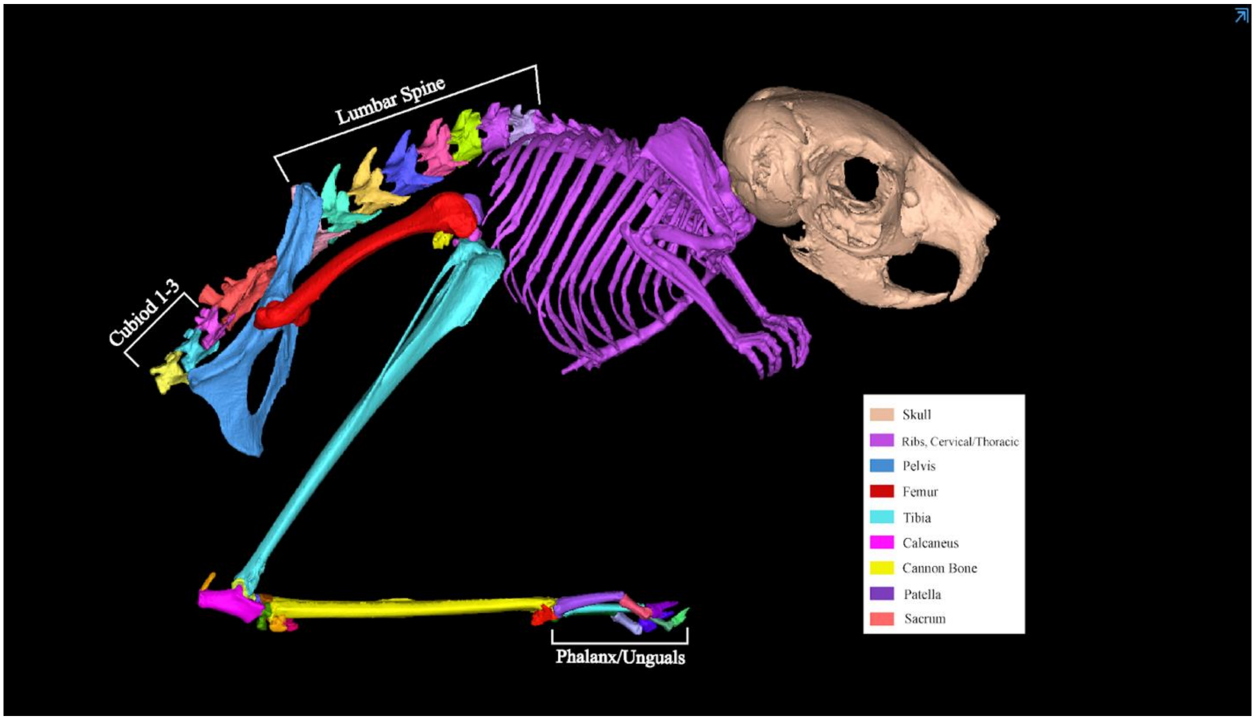

Figure 3.1: Complete segmentation of jerboa hindlimb, spine, ribs and skull, where different colors indicate individual meshes.

A total of 26 individual muscles in the hindlimb were segmented. Those included Medial and Lateral Gastrocnemius (MG & LG), Plantaris (PLANT), Soleus (SOL), Tibialis anterior

(TA), Extensor Digitorum longus (EDL), Flexor Digitorum longus (FDL), Flexor hallucis longus (FHL), Popliteus (POP), Vastus lateralis (VL), Vastus medialis (VM), Vastus intermedius (VI), Rectus femoris (RF), Biceps femoris anterior and posterior (BFA, BFP), Gemellus inferior (GI), Quadratus femoris (QF), Semitendinosus (ST), Adductor longus (AL), Obturator externus (OE), Obturator Internus (OI), Pectineus (PECT), Peroneus longus (PL), Peroneus digiti quarti (PDQ), Gluteus superficialis (GSup), and Iliacus (ILI). Nine additional muscles were segmented into various groups. Gluteus maximus (GMax), Medius (GMed), Minimus (GMin), and Gemellus Superior (GS) were segmented together in the gluteal group as they were very intimate in region and their separation was difficult. Semimembranosus (SM) was segmented together with Adductor brevis (AB) and Adductor magnus (AM) as their fibers were intertwined and the unit was inseparable in microCT. Gracilis anterior (GA) and Gracilis posterior (GP) were also segmented as a single muscle. Finally six muscles where found to be absent in the imaging with respect to the mouse hindlimb; Extensor hallucis longus (EHL), Caudofemoralis (CF), Peroneus brevis (PB), Peroneus digiti quinti (PDQI), Peroneus tertius (PT) and Tensor fascia latae (TFL) [25]. Additionally, Psoas Major (PMA), Psoas minor (PMI) and Tibialis Posterior (TP) were not segmented. The above was corroborated by work done by zoologist Alfred Howell in addition to close review of a mouse model and experimental jerboa microdissections [25,26]. Post-processing and smoothing were not required as muscle geometries are not modeled the same as bone in 3D musculoskeletal models.

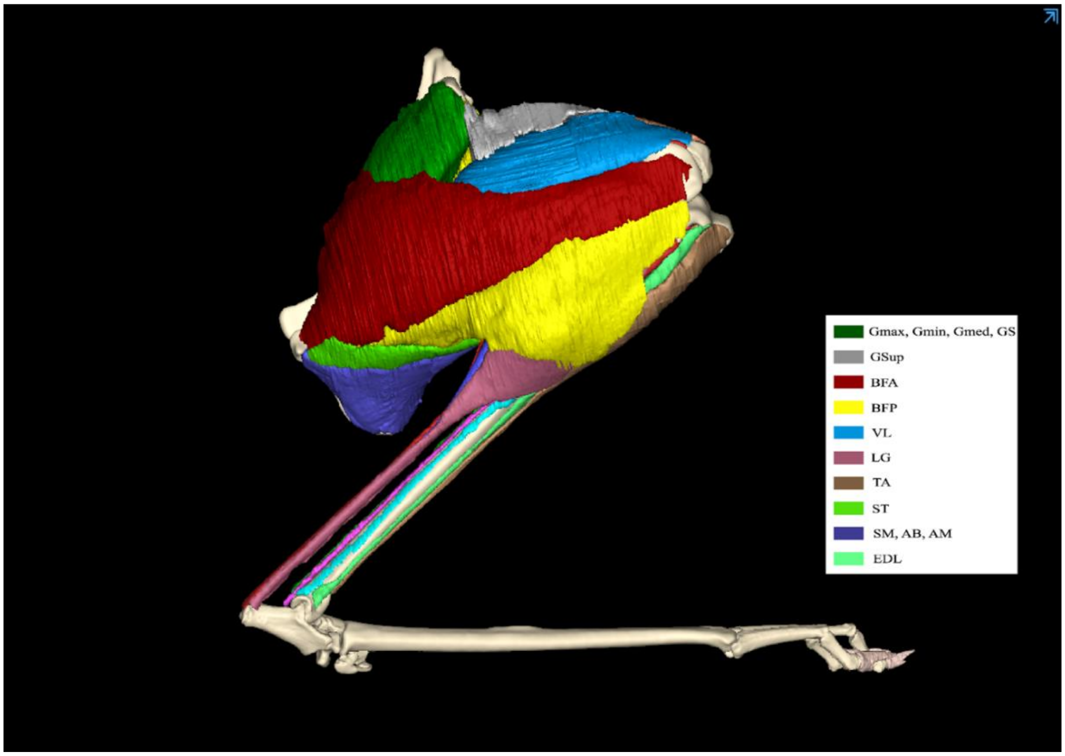

Figure 3.2: Jerboa right lateral hindlimb with color coded meshes corresponding to superficial muscles.

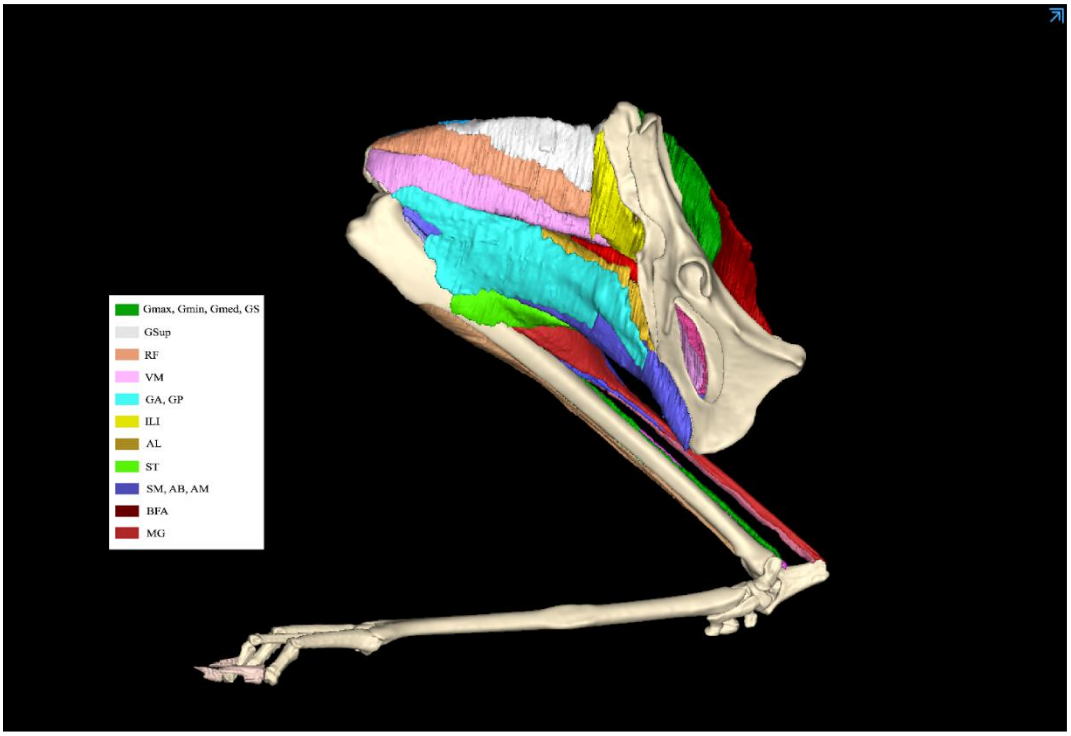

Figure 3.3: Jerboa right medial hindlimb with color coded meshes corresponding to superficial muscles.

Figure 3.4: Jerboa right medial hindlimb with color coded meshes corresponding to inferior muscles.

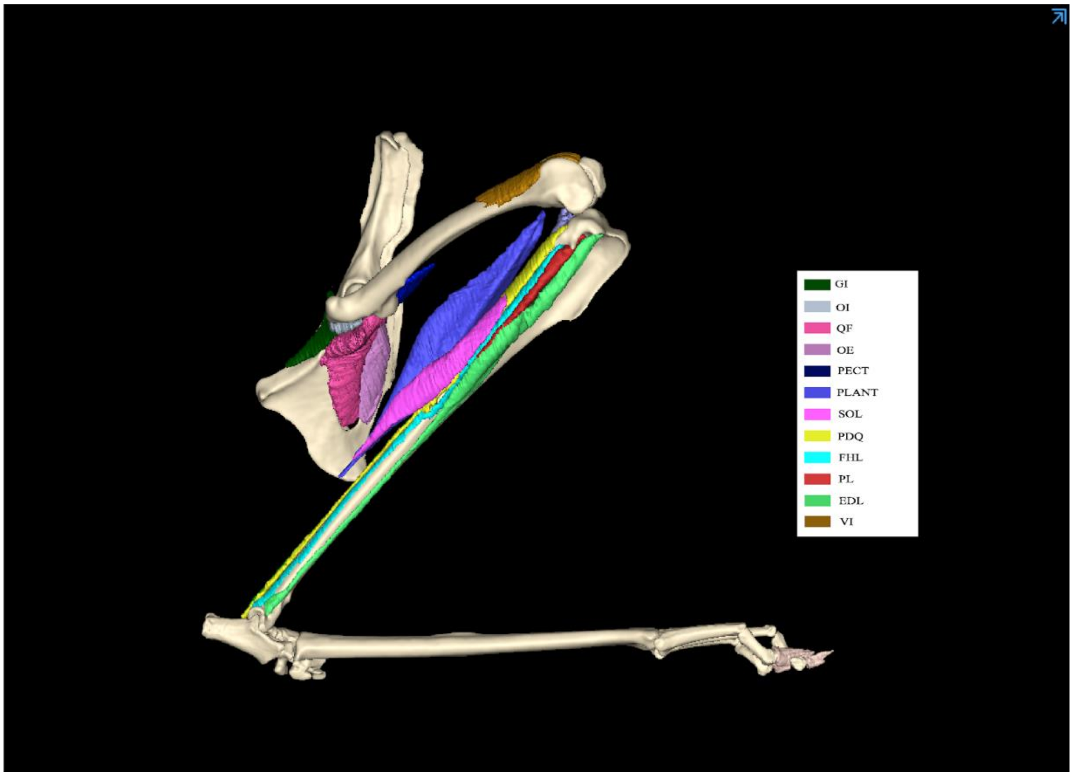

Figure 3.5: Jerboa right lateral hindlimb with color coded meshes corresponding to inferior muscles.

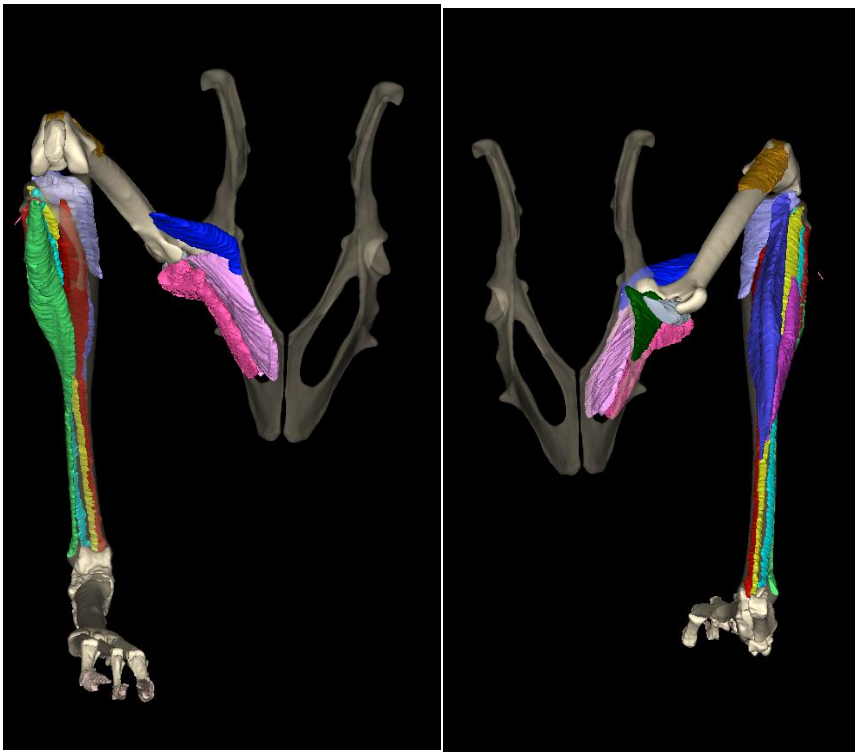

Figure 3.6: Jerboa hindlimb anterior (left) and posterior (right) view with color coded meshes corresponding to inferior muscles.

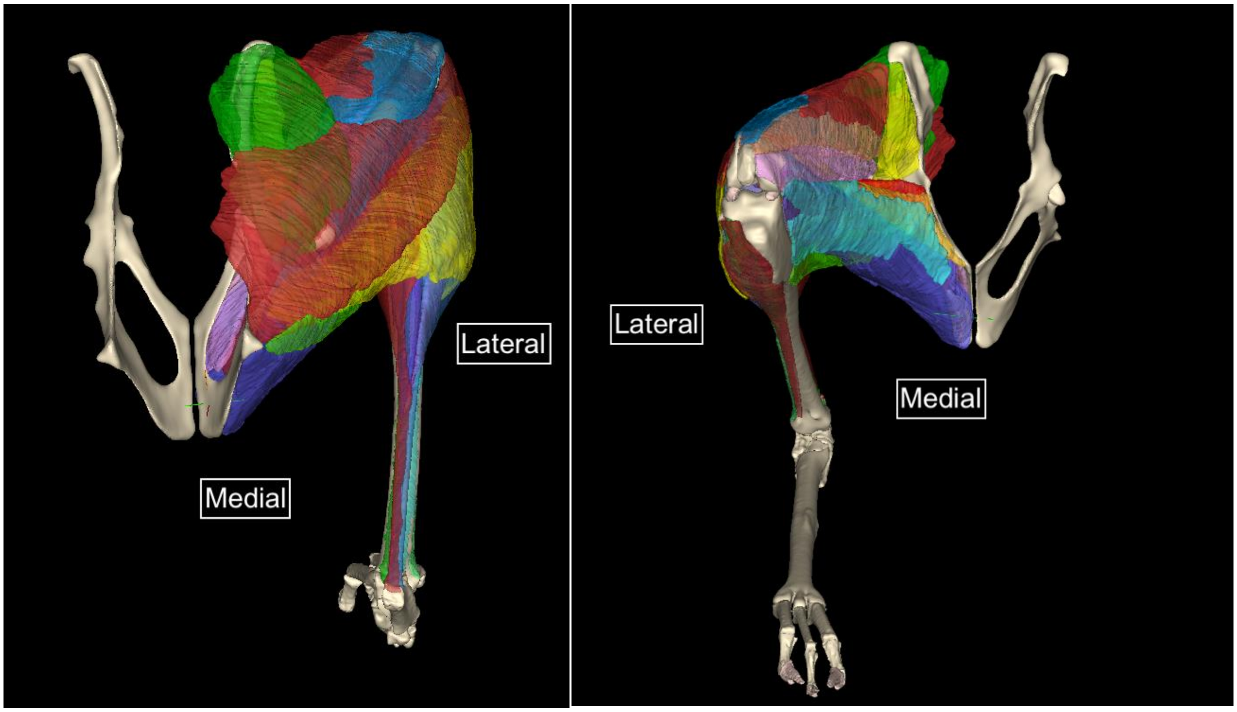

Figure 3.7: Jerboa hindlimb posterior (left) and anterior (right) view with transparent color coded meshes corresponding to superficial muscles.

Segmental masses for rigid body mass properties resulted in approximately 99% of the total weight of the specimen before dissection, where loss of mass may have arisen during dissection from phenomena such as sample drying or scale fluctuations. Images of the weighted segments can be viewed by accessing Appendix A: Accessing the Database.

Table 3-1: Segment mass corresponding to segments highlighted in Figure 2.1, the percentage body weight for that specimen and then a scaled version for microCT.

Segment	Mass (g)	Percent Body Weight (%)	Corresponding Mass for 51.49 g
Upper Body	38.15	65.92	33.94
Hips	6.86	11.85	6.10
Thigh	2.552	4.41	2.27
Shank	1.718	2.97	1.53
Metatarsus + Tarsus	0.345	0.60	0.31
Patella	0.012	0.021	0.012
Center Proximal Phalanx	0.03	0.05	0.03
Lateral Proximal Phalanx	0.028	0.048	0.025
Medial Proximal Phalanx	0.032	0.055	0.028
Center Distal Phalanx	0.017	0.029	0.015
Lateral Distal Phalanx	0.02	0.03	0.02
Medial Distal Phalanx	0.02	0.03	0.02
Center Ungual	0.018	0.031	0.016
Lateral Ungual	0.018	0.031	0.016
Medial Ungual	0.017	0.029	0.015
Right Hindlimb	5.41	9.34	n/a
Tail	2.06	3.56	n/a
Total	57.30	99.023	n/a

3.2 Multibody Musculoskeletal Model

A musculoskeletal model was built in OS using the built-in MATLAB API. The model consists of 13 joints in the hindlimb, a total of 27 individual bodies in the upper body and hindlimb, and 32 muscles represented with a total of 36 MTUs. Parameterization of the bodies was done with the pelvis as the primary joint with the ground, and the topology of joints following that seen implemented by previous OS models. It comprises a nested parent-child relationship between bones that are adjacent (Figure 3.8). Joints in the hindlimb consisted of the ground, hip, knee, patellar-femoral, ankle, three metatarsal-phalangeal and three phalangeal. All joints rotated about a single point, except the knee and patellar-femoral joints that featured translation as a function of rotation. All joints in the hindlimb featured no bone penetration in the previously defined range of motion (Appendix B) for all allocated degrees of freedom. All MTUs feature placeholder values for contractile parameters as they are required for construction. Joints not in the hindlimb allowed for movement away from the CT-pose and were saved in a default angle value along with a stance phase for the hindlimb. MATLAB API code structure was validated by successfully replicating a previous model written in xml and outputting identical results to those published [8].

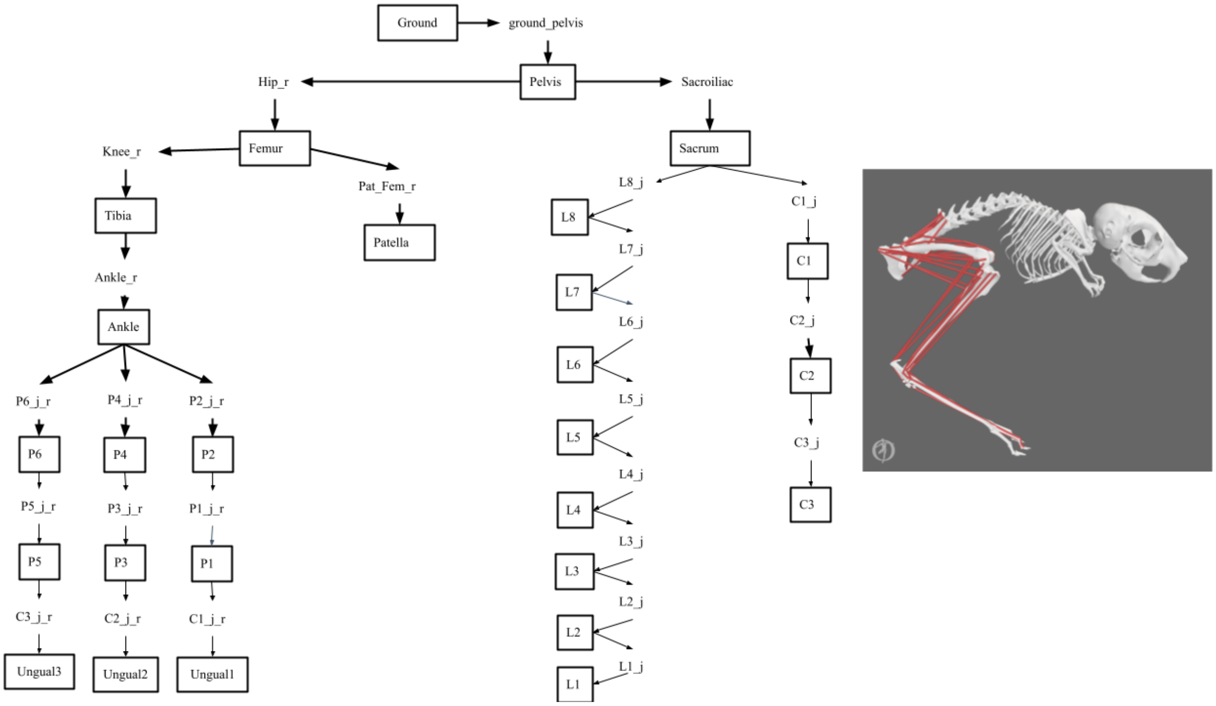

Figure 3.8: Musculoskeletal Model parent and child body topology. Boxed words refer to parent or child bodies (beginning with the ground) and unboxed words represent joints between the previous and following arrowed bodies.

3.3 Model Evaluation

The LG was the only muscle with origins and insertions that were moved in two perpendicular directions resulting in eight separate MTUs for just origin and insertion. Changes to origin both along the shaft of the femur between the hip and knee joint and circularly around the shaft resulted in small differences to moment arms at the ankle (with the knee flexed at 90 degrees), where the maximum percent change was below 0.5%. Similarly, altering the wrapping surface on the posterior side of the tibia, resulted in changes less than 5%, which primarily occurred at extreme joint angles such as -40 and greater than 50 degrees (Figure 3.9 A). Conversely, changes to insertion cranially and caudally along the border of the calcaneus resulted in larger differences, with maximum differences of about 16% at about -26 degrees of ankle extension. Moment arm results at the knee showed the opposite findings. Insertions showed very little effects on the moment arm through the entire joint range, but origins both along and around the femoral shaft showed larger differences up to about 13% at knee joint angles less than -120 degrees. Changes to wrapping surfaces featured slightly larger changes.

Observations of the PLANT at the ankle joint showed moment arm magnitudes were insensitive to all changes except the first VP. The PLANT is constructed with a total of nine VP s between origin and insertion, and completely removing VPs two to nine had no effect on moment arm values, putting more emphasis on the selection of the first VP (Figure 3.9 C). The first VP appears to constrain any points following, and changes to the first VP (closest to the ankle) resulted in a 43% increase in moment arm magnitudes at 57 degrees. The same changes observed over flexion and extension of the P3 phalanx showed zero effect in all plots except for removal of VPs (Figure 3.10). Movement of origins caused the largest increases or decreases of about 18% change at -113 degrees of knee flexion with no effect from insertion, or VPs.

Wrapping surfaces also contributed to approximately 9% changes at a knee angle of -45 degrees (Figure 3.9 D).

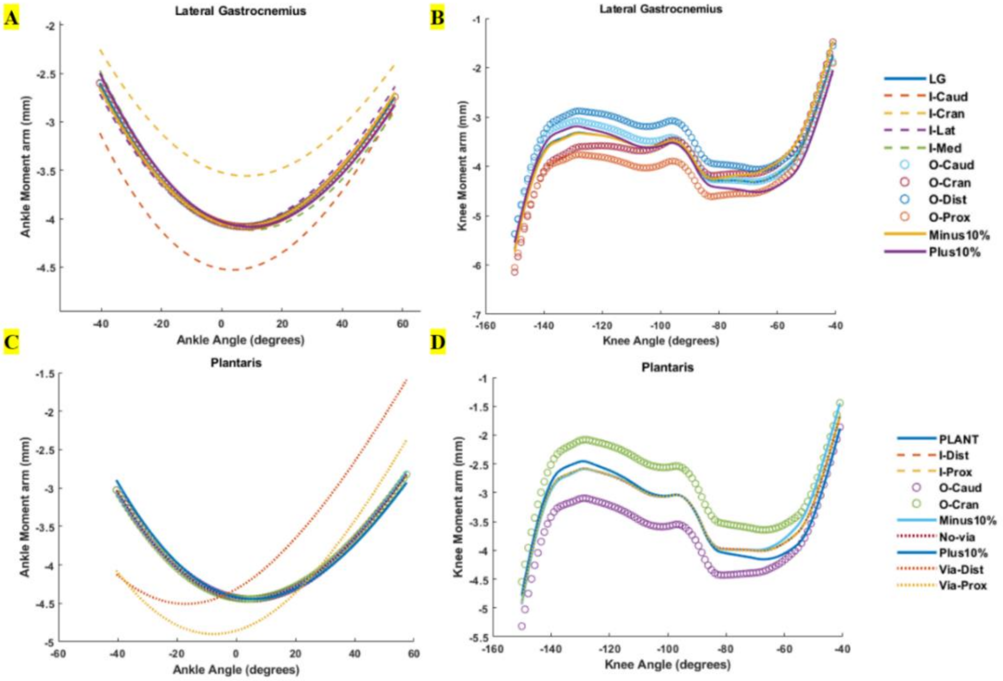

Figure 3.9: Plots of joint angle on the x-axis vs moment arm on the y-axis for the Plantaris and Lateral Gastrocnemius. Each line represents an MTU with an altered input parameter. At the knee, changes to origin site location affect the moment arms the

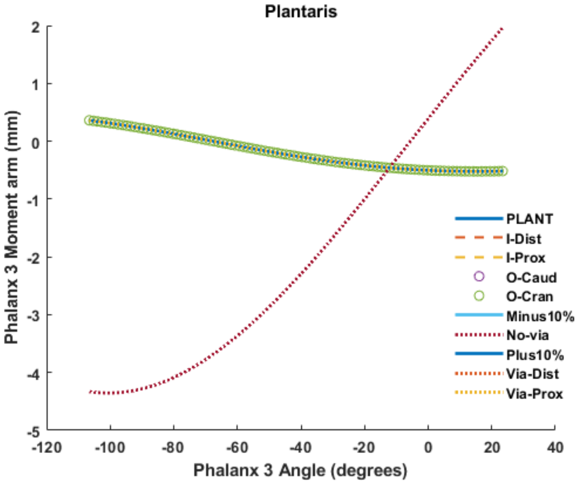

Figure 3.10: Middle Phalanx angle on the x-axis vs moment arm for Plantaris. Ten lines each representing an MTU with a variation of the original input parameters. Only removing via points had any effect on moment arm magnitude.

TA moment arms at the ankle were insensitive to any changes to parameters except for changes to VPs. Removal of VPs between the first VP and the insertion generated up to 29% increase in moment arm magnitude at 10 degrees. Movement of the first VP both laterally and medially resulted in changes with very similar percent changes at 4 degrees and 33 degrees (Figure 3.11).

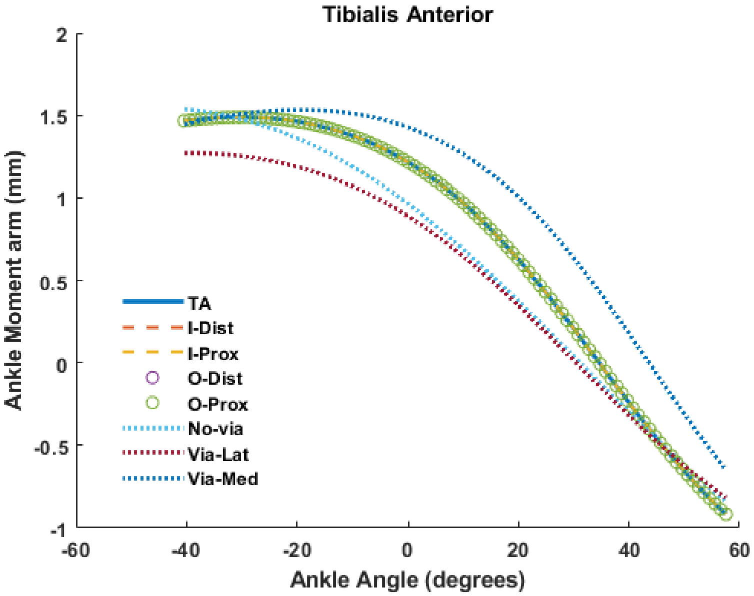

Figure 3.11: Moment arm magnitudes on the y-axis vs joint angle on the x-axis for various modified MTUs of the Tibialis Anterior. Changing origins and insertions had no effect on moment arm magnitude with the presence of via points.

The RF was sensitive at the hip joint during flexion and extension to changes in origin, resulting in about 25% increases or decreases in moment arm values. However, it was unaffected by other changes except minor observances during extreme flexion and extension when removing the VP constraining the muscle path to the centerline of action of the segmented STL (Figure 3.12 B). These same changes at the knee were much different. Overall, each modified MTU followed a similar path to the original RF, with the largest deviation seen in the distal insertion modification at 25% change. Wrapping surfaces changes at the knee to influence wrapping over the femoral condyles resulted in 6-7% differences. Origins showed no effects on moment arm magnitudes as expected from the VP and distance from the joint center. Insertions had the greatest influence but only at angles between -60 and -40 degrees (Figure 3.12 A).

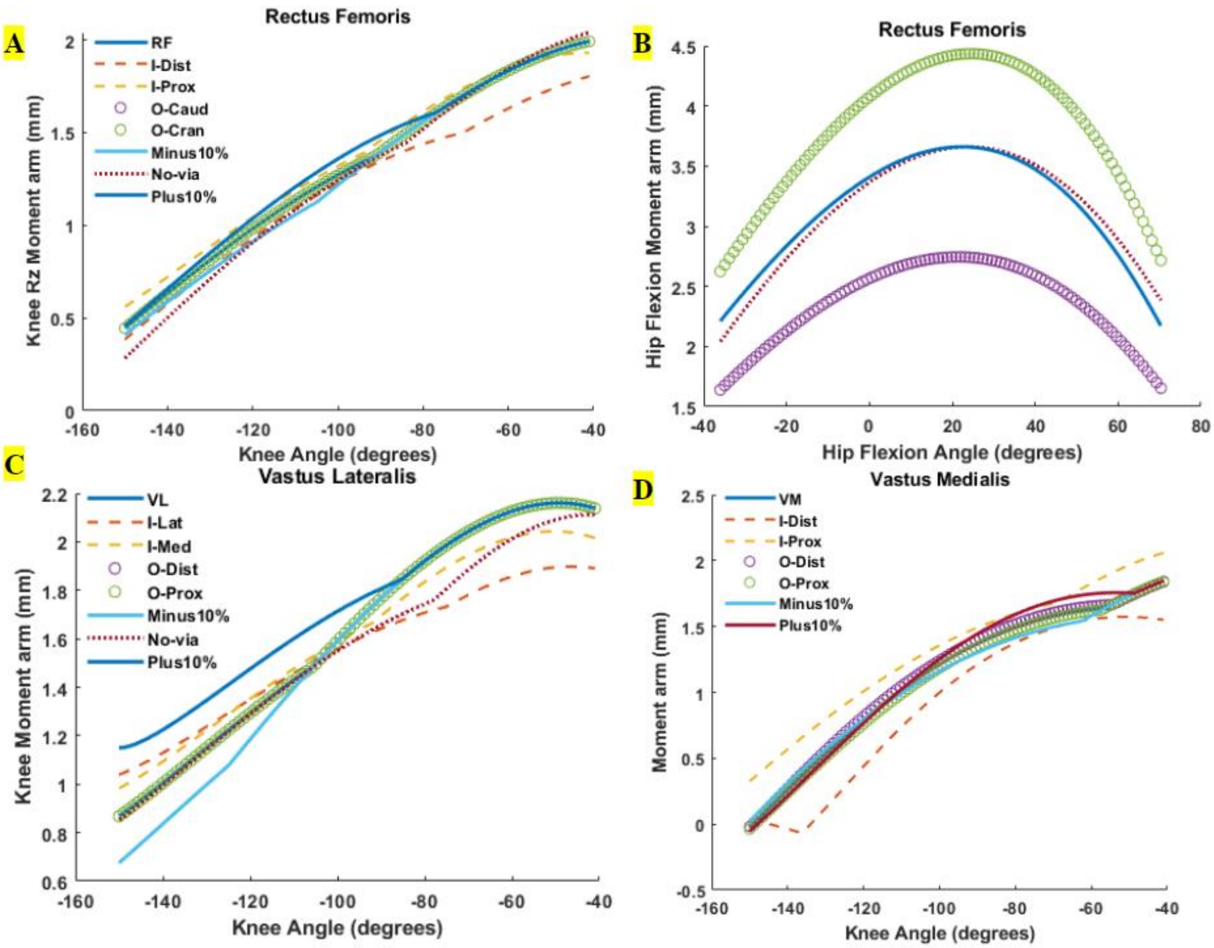

Figure 3.12: Plots of knee extensor muscles featuring modified MTU parameters. Joint angle on the x-axis vs moment arm magnitude on the y-axis. At the hip for Rectus Femoris, changes to origin sites can be seen having large effects on moment arm magnitudes, whereas at the knee for all the muscles, insertions or via points have a greater influence on moment arms. For Vastus Lateralis, changes to wrapping surfaces had greater effects than for other knee extensors.

Although similar in location and function to the RF, the VL appeared to be affected much more by wrapping changes (they feature the same wrapping at the condyles) with about 32% change at -150 degrees. Origin fluctuations had no effect, and insertions reached a maximum difference between lower angles at about 12% change (Figure 3.12 C). VM was not created with a VP and thus could be seen with percentage changes during origin modifications of as low as

3% increase in moment arms. Changes in insertion appeared to have effects that spanned more of the joint range than the other knee extensors but stayed within 0.5 mm differences.

BFA showed insensitivity to all changes. It showed less than 6% change in moment arms when completely removing a large wrapping surface preventing the BFA from penetrating along the shaft of the femur. Although hip flexion was analyzed, changes to origins featured much less of an effect (1-9%), versus insertions that were much farther from the joint center (24-45%) (Figure 3.13). Overall, the offset for all MTUs was consistent along the joint range.

STs removal of wrapping that prevented penetration at the hip resulted in close to no change during all three movements, with the highest deviation at about 3% for knee extension of -41 degrees. The knee moment arms featured the largest effect from insertion changes due to the proximity to the joint center and the vast insertion uncertainty. The changes were greatest at larger flexion angles past -120 degrees at about 15 % differences. Also unsurprisingly, the largest impact as a result of modifying origins was at the hip during flexion and rotation, between 7-17% change (Figure 3.15).

Semimembranosus featured a complex muscle path and was thus accompanied by four wrapping surfaces to prevent bone penetration and constrain the line of action to the muscle belly seen in the microCT imaging. Therefore, the only analysis here was to look at the effects of wrapping on muscle moment arms in all three hip degrees of freedom. For hip flexion and extension, each MTU followed very closely along the joint range and featured slight deviation near angles of 60 to 80 degrees. The largest effect came from removing a spherical wrapping surface at the greater trochanter with a 22% difference, but this is not occurring at maximum moment arm values and thus may appear larger. All femoral wraps within hip rotations are within 23% change, with the removal of an ellipsoidal wrapping at the distal end of the femoral head resulting in no effect at all.

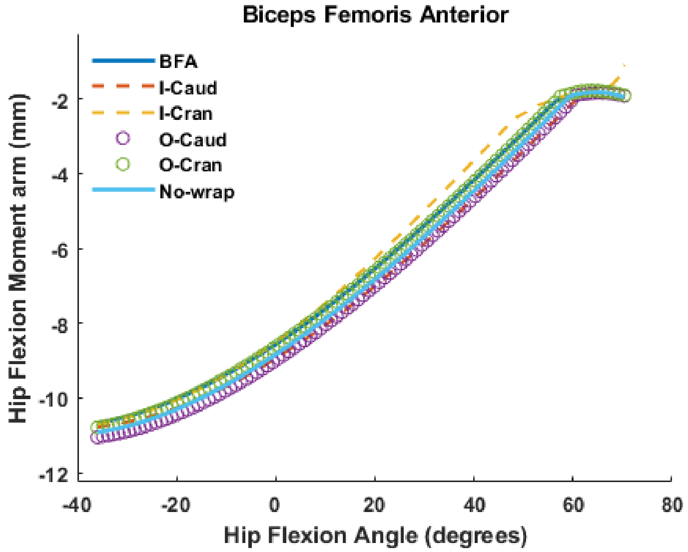

Figure 3.13: Biceps Femoris Anterior altered MTU parameters observed at hip flexion angles vs moment arm magnitudes. Larger adjustments to insertion were made and therefore greater effects in moment arm magnitude.

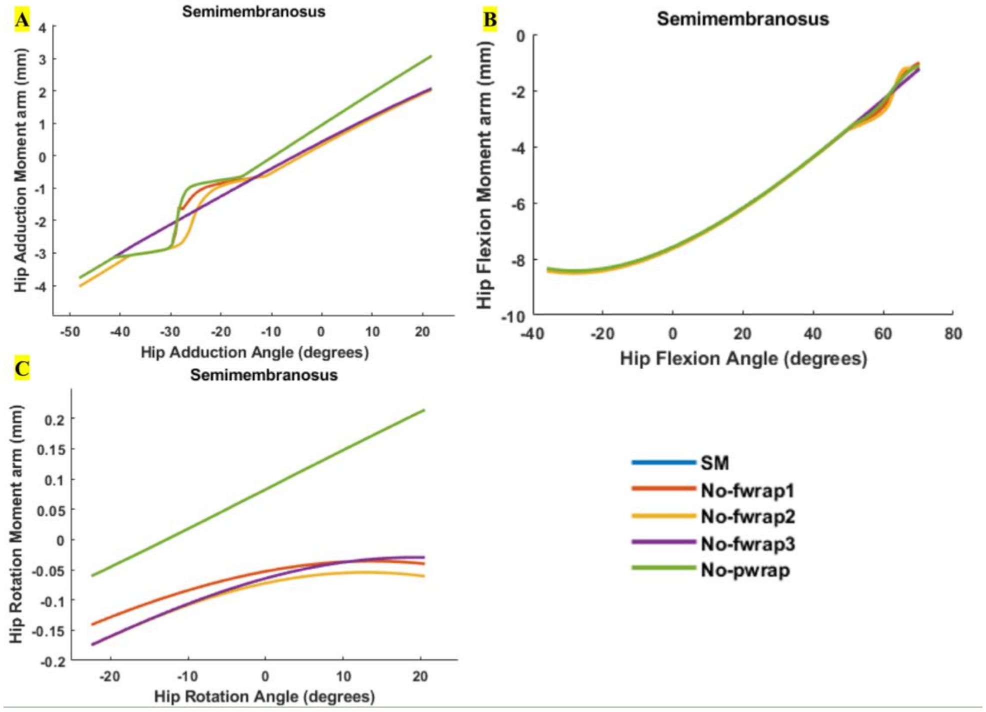

Figure 3.14: Plots of joint angle on the x-axis vs moment arm magnitude on the y-axis for variations of wrapping surfaces for Semimembranosus MTUs. Hip rotation moment arms were influenced the most, while hip flexion was perturbed the least when cycling through removal of wrapping surfaces.

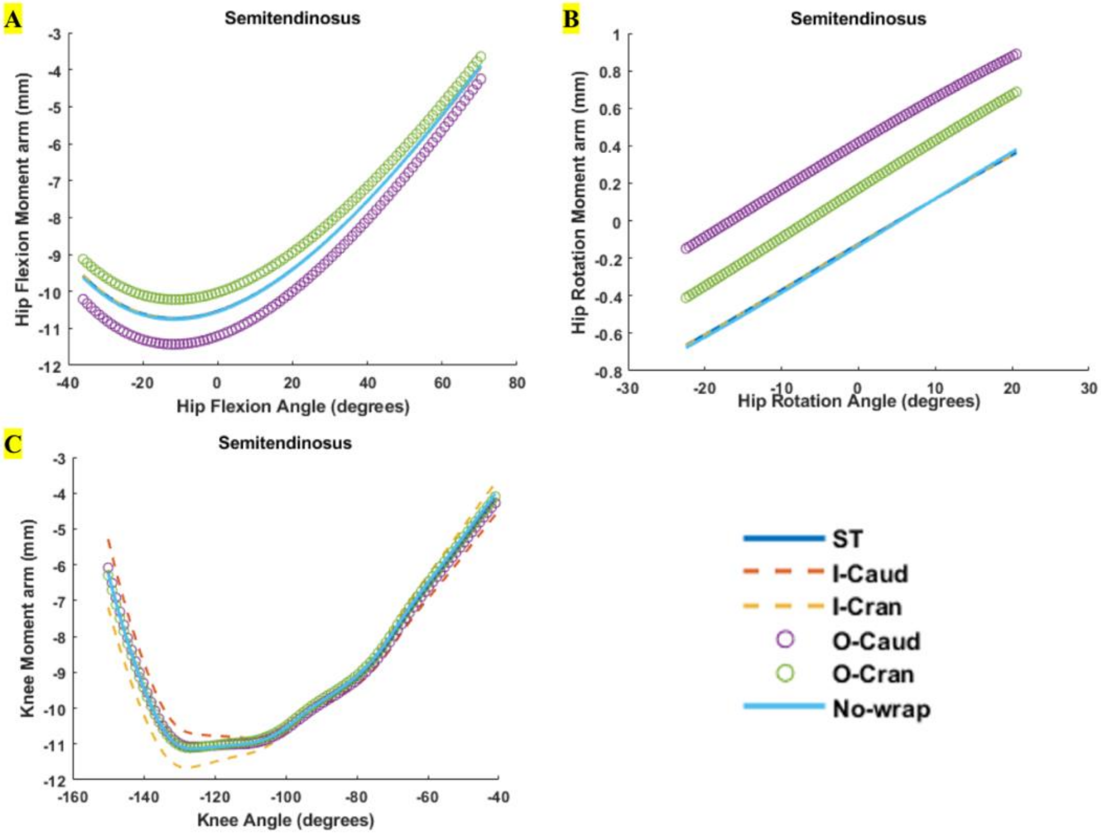

Figure 3.15: Altered MTU input parameters of Semitendinosus for joint angle (x-axis) vs moment arm (y-axis). At the knee, changes to insertion had the largest influence on moment arm magnitudes, whereas at the hip changes to origin had much greater effects.

AB was analyzed at all three motions as well to investigate potential changes in functional characteristics of the muscle. AB origins and insertions were difficult to visualize in segmentation and were therefore developed from previous literature. A larger bound was used for insertion than typical for other analyses, but only in a single direction. At hip rotation, this point resulted in the largest change with about 27% at 20 degrees. Effects of origin were much smaller, where cranial changes resulted in 2% difference and caudal changes in 7%. During hip flexion, which featured the largest magnitude in moment arms of the 3 movements, results were affected much less with insertion resulting in a maximum of 12% change and origins creating differences that fell within 5%. During hip adduction, insertion movement led to a 33% increase in adduction moment, while origins peaked at 10% differences. Similarly, AM was analyzed at the same 3 degrees of freedom, with the inclusion of changes to wrapping surfaces and an additional insertion that was medial. Observations of hip rotation had the largest effect seen in any muscles with both origins and insertions resulting in great sensitivity as high as 60% and 40%, with wrapping changes staying within 10%. Hip flexion was affected much less, with origins at about 8% and insertions following well under that percentage except at a peak near 70 degrees where the moment arms approach zero. Wrapping surface changes also had low influences until this very degree. Hip adduction followed the opposite trend where insertions resulted in greater effects than origins at a high of 40% appearing at -22 degrees. Along the rest of the path, insertions appeared to mate with the original MTU closely. Origins and wrapping were all under 10% and had consistent differences along the path of the joint range.

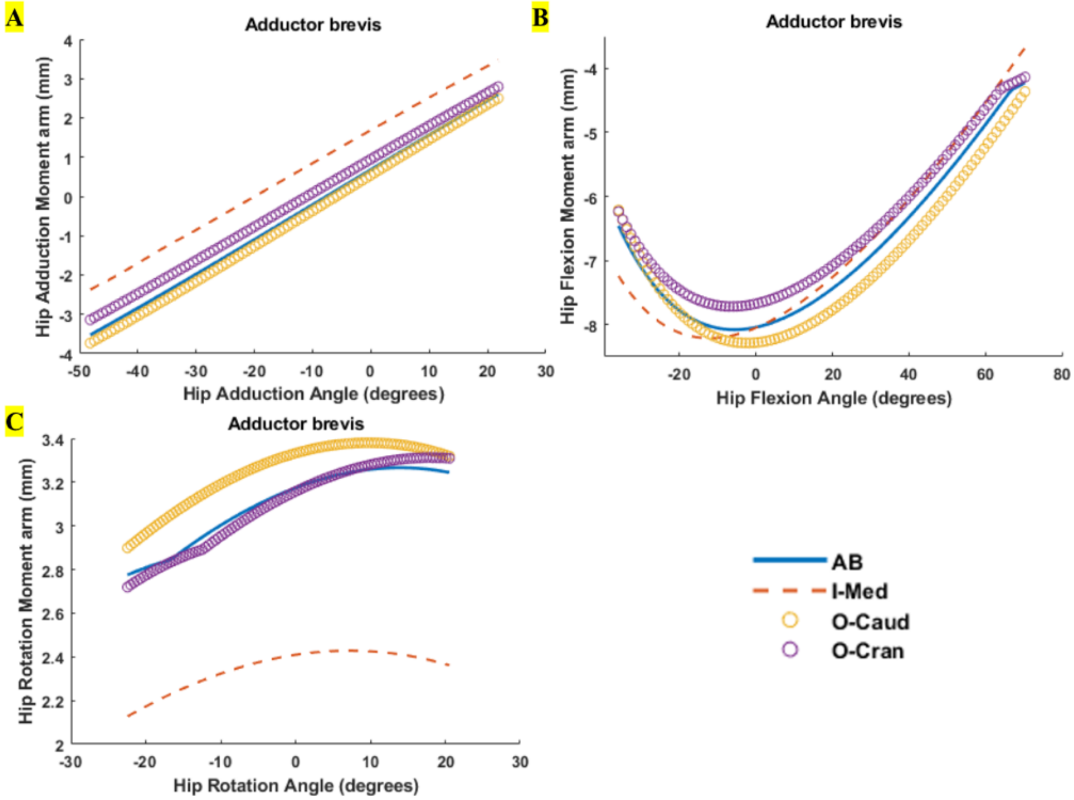

Figure 3.16: Joint angle on the x-axis vs moment arm magnitudes on the y-axis of Adductor brevis for three MTU variations. A single point adjustment for insertion was chosen with exceedingly large uncertainty, showing moment arm influence at all degrees of hip movement.

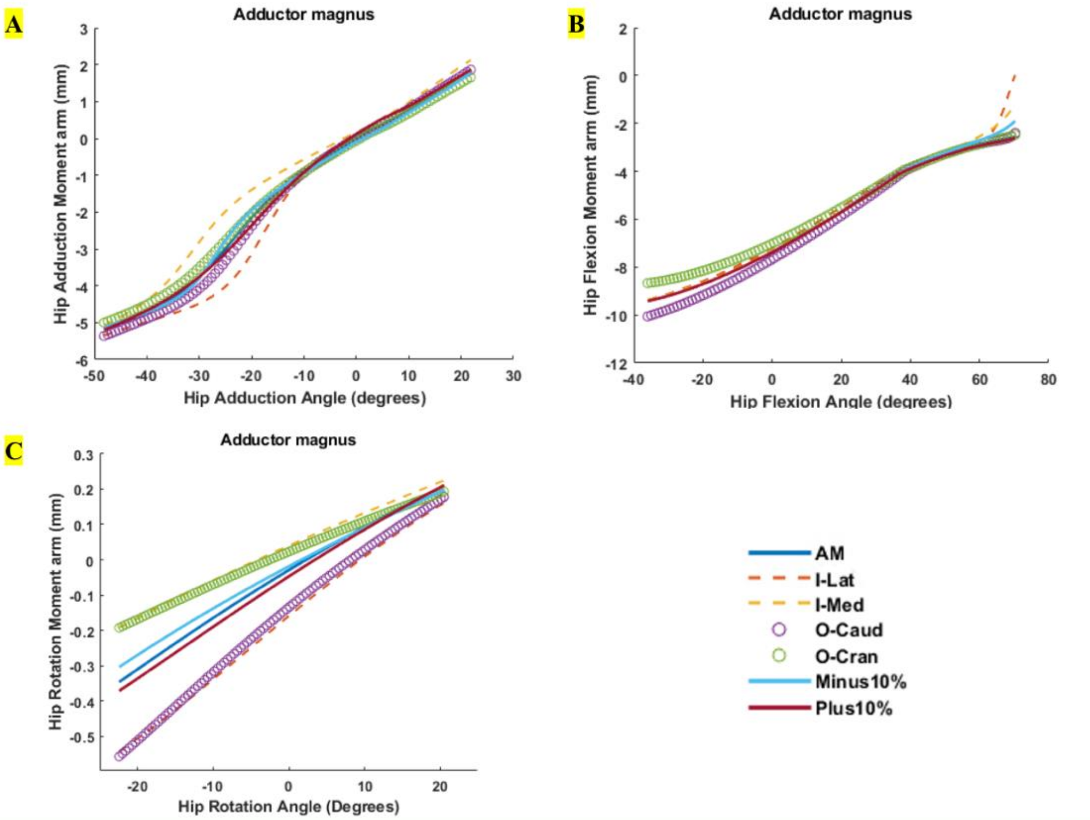

Figure 3.17: Adductor Magnus altered MTU parameters plotted with joint angle (x-axis) vs moment arm (y-axis). Moment arms are most affected by both variations in origins and insertion sites during hip rotation.

The box plot of percentage changes in muscle parameter for the 11 muscles (Figure 3.18) showed that the percentage difference was on average highest for insertions at approximately 18%. VPs followed closely behind at 17.2%, and origins and wrapping surfaces were as low as 8.8% and 8.6% (represented by the green dot). Insertions also had the largest outliers, with over 100%, where percentage differences that were approaching infinity were not accounted for. These values were either adjusted for the 2nd largest difference that wasn't crossing zero or removed from the dataset. Wrapping surfaces fell within the smallest range of percentage differences, along with origins very close. VPs 3rd quartile falls in a larger range of high percentages than any other group. Investigation of insertions percentage changes over joint motion and angles (Figure 3.19) shows that the hip joint features higher average percentages in all three degrees of rotation, larger ranges of differences, and overall values that exceed knee and ankle maximum percentage changes.

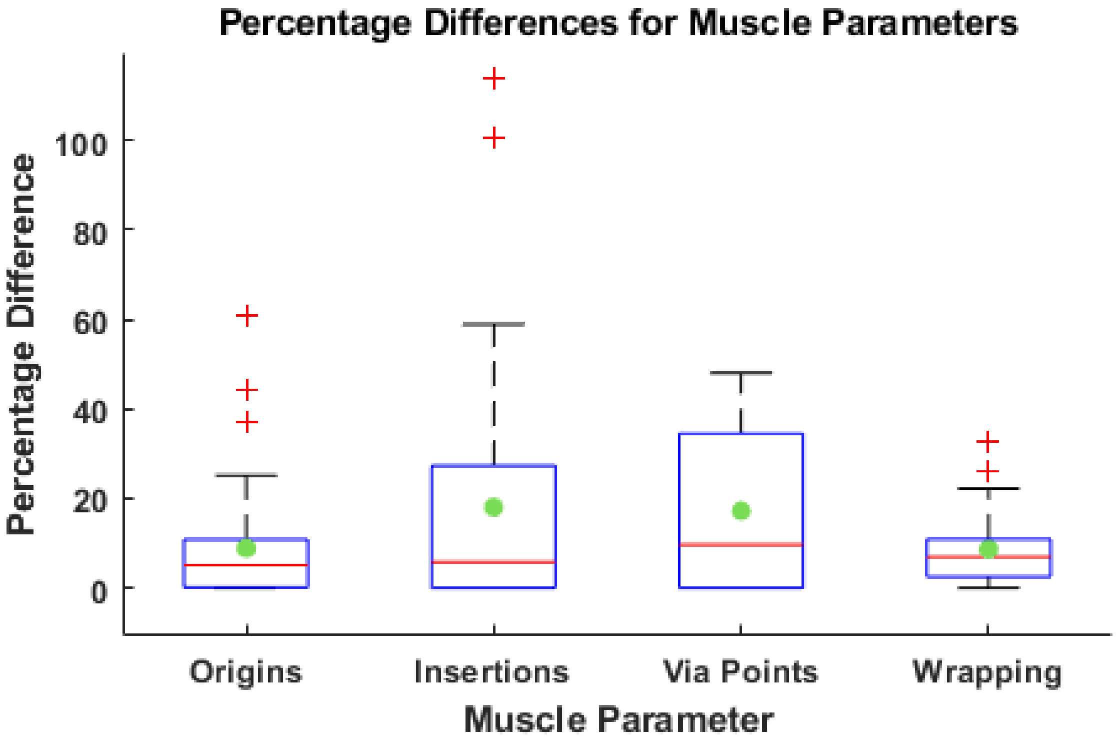

Figure 3.18: Box plot of model evaluation for changes to origins, insertions, via points and wrapping surfaces. Insertions feature the largest average percent differences, via points following behind, and wrapping surfaces with the lowest average percent differences. Insertions have the largest outliers and while via points have a 3rd quartile in a higher range of values. Average percentages are represented by green dots.

Separation of the percentages for each joint degree of freedom with respect to the corresponding angle that it occurred at can be seen in Figure 3.20 and Figure 3.21. No clear trend dictated by joint angle extremes or ranges can be seen in any degree of freedom. Outliers are more easily distinguished, with an evident large percentage change during knee flexion at -140 degrees. A majority of data points in the knee cluster between higher and lower joint angles, but still occurred below 20% differences. Each plot features a different range of motion due to the corresponding joint range defined in Section 2.8.

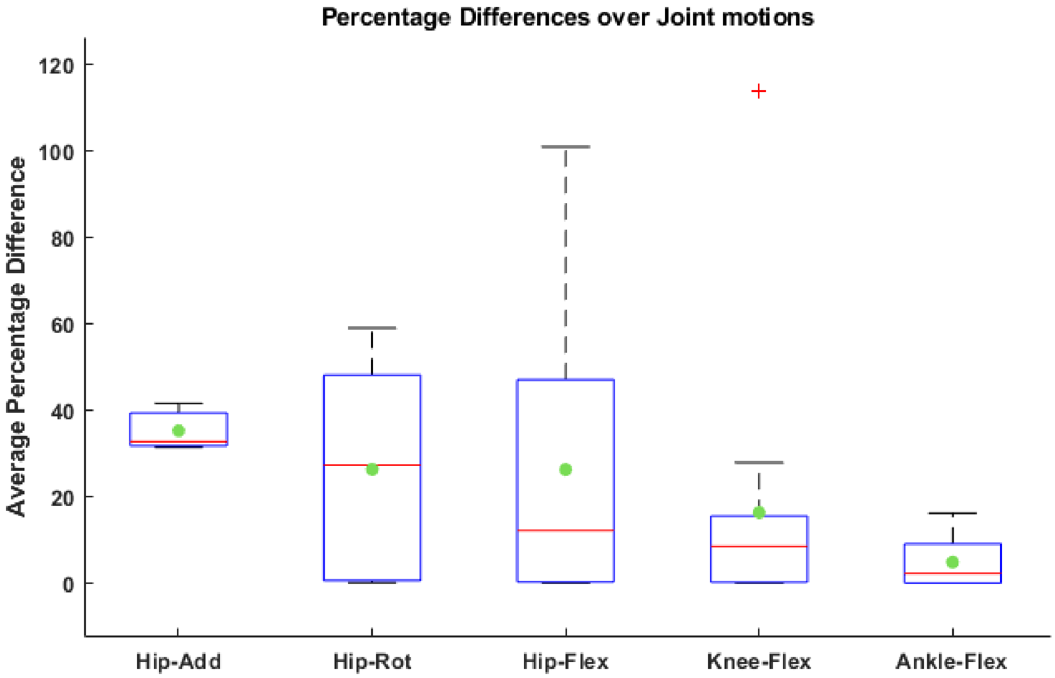

Figure 3.19: Plot of percentage differences in insertions separated by joint motions. Green dots signify an average percent difference. Plot shows a much higher trend of percentage differences in the hip than any other joint.

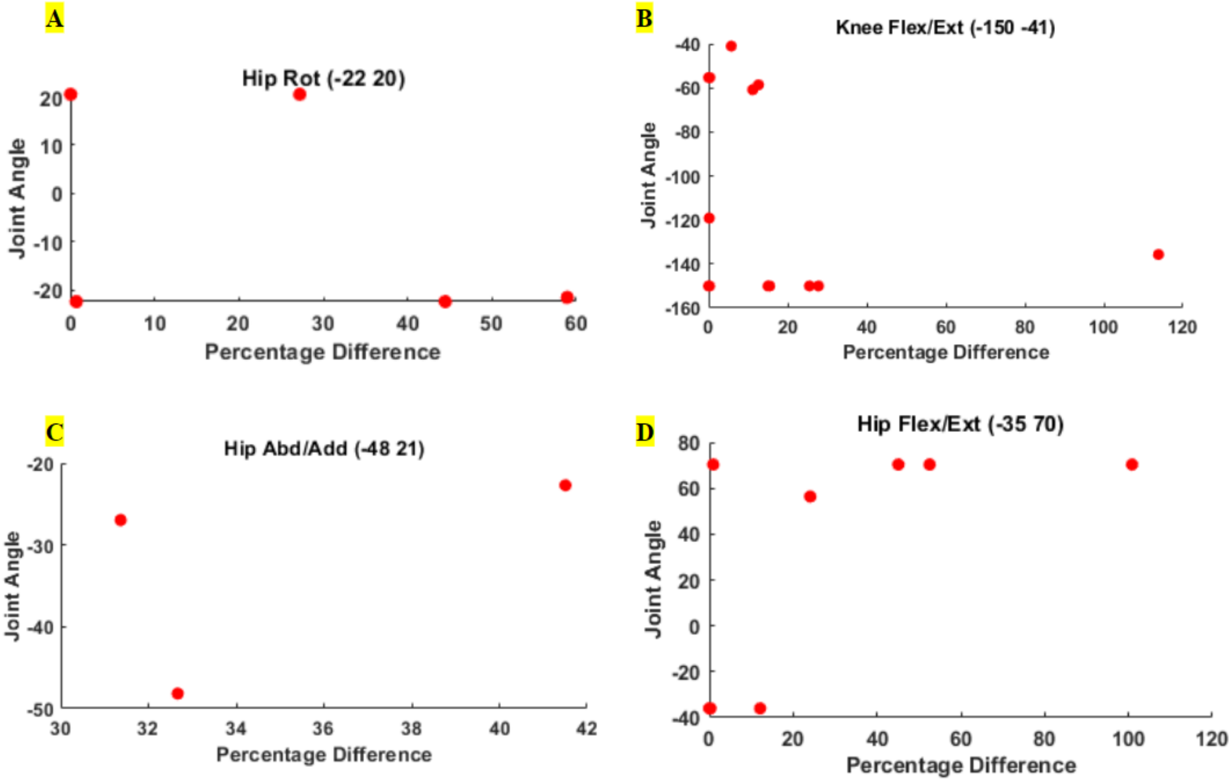

Figure 3.20: Plots of Percentage change in insertion vs joint angle separated by joint movement.

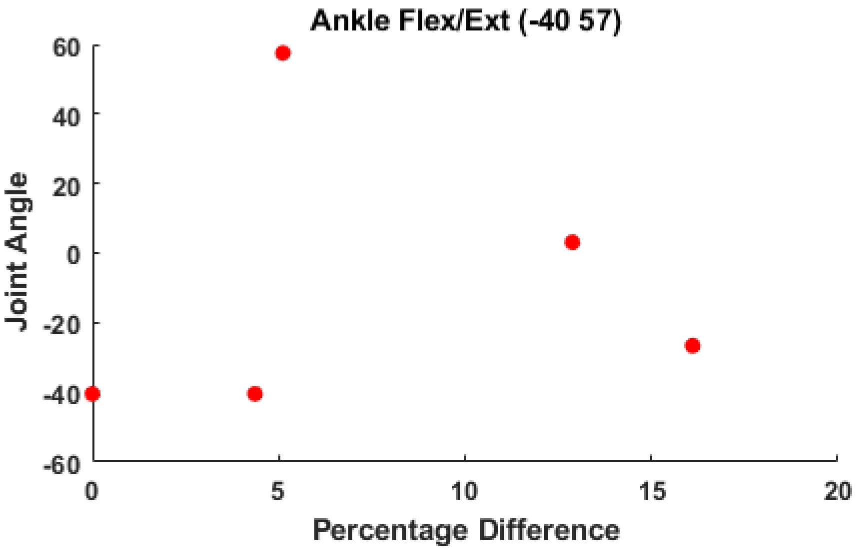

Figure 3.21: Percentage change vs joint angle for during ankle flexion and extension of the right hindlimb during insertion evaluation.

Chapter 4 : Discussion

This study developed the first 3D jerboa hindlimb musculoskeletal model utilizing microCT imaging to obtain bone and muscle geometry inputs. Bone STLs were utilized to generate joints and clinically relevant bone coordinate systems that could be populated with mass properties and constrained to physiological ranges of motion. Muscle meshes assisted in identifying attachment points, generating wrapping surfaces and ultimately calculating muscle moment arms. Using a sensitivity analysis, the model was shown to be robust to changes in important muscle parameter inputs, where varying effects in the results were identified and highlighted. The above was implemented for the purposes of generating the first steps to relating form to function in the jerboa while attempting to tackle complex and intricate integration of muscular and skeletal systems that cannot be simultaneously probed and analyzed experimentally.

4.1 Sensitivity analysis

The LG in Figure 3.9 A and B displayed changes to origin and insertion in four different directions. It became apparent from the percent changes that moving points closer or farther from joint centers had much greater effects than in the perpendicular direction. Therefore, all points selected on following muscles were first determined by the larger direction of uncertainty for that muscle and if the muscle spanned equally in both planes, then in the axis that corresponded with further or closer to the joint center of interest. The origins and insertions of the PLANT in the jerboa, unlike in other rodents, is much further from the ankle joint than seen in other muscles of the plantar flexor group, explaining why there may be below 1% difference as a result of moving such points. Additionally, as seen in Figure 3.9 C, the largest effects resulted from changes to VPs. Specifically, in the first defined VP of the PLANT, which happens to be the closest to the joint center, relative to the remaining. When altering these same VPs at the phalanx in Figure 3.10, there was no change, with the only effects seen by removal of the VPs after the first. This large change in moment arms at the phalanx is expected due to the removal of the VP closest to insertion and up to the ankle causing a drastic change in the muscle line of action. A more reasonable adjustment to more conservatively view the effects for this joint would have been local adjustments of VP nine which would have likely resulted in smaller perturbations in moment arm values like those seen in Figure 3.9 C. At the knee for both PLANT and LG adjusting insertions did not result in the largest effect on moment arms but rather the largest observable effect is seen by changing origins, due to their much closer proximity to the knee joint. Figure 3.9 B and D feature a similar curvature and perturbations along the graph, which can be accounted for by the polynomial function generated for translation of the tibia with respect to the femur. In the dorsiflexor group, the TA was chosen as another muscle with VPs, to observe differences in sensitivity that may not be apparent from the EDL due to its similar path to the PLANT. Unsurprisingly, Figure 3.11 shows phenomena very close to the PLANT with respect to adjustments that resulted in moment arm changes. Although the TA does not insert on the phalanx as does the PLANT, its path features curvature that requires VPs, which in this case prevents any effects in path from being seen by the joints from the insertion or origin.

Knee extensors were another important group that was probed for movement in the sagittal plane. The greatest differences between the muscles could be seen where VL featured larger sensitivity to wrapping surface changes than VM or RF. In jerboa, VL follows a path more dorsal to the femur than other rodents, and although it features an identical wrapping surface to that seen in RF and VM, its path evidently shifted much more when wrapping is increased or decreased as seen in Figure 3.12. BFA was analyzed due to its very large span at insertion and featured the largest insertion adjustment in both directions in the entire sensitivity analysis. As seen in Figure 3.13, unlike the remaining monoarticular muscles, BFA showed much greater effects in moment arm magnitudes from insertion, which was much farther from the joint than origin. This can likely be attributed to the much larger point adjustment causing the insertion to drastically affect the muscle line of action, also due to its rather unphysiological wrapping on the femoral condyles when shifted 1.5 mm.

ST was a muscle that featured functional characteristics that fell outside the envelope of previously defined groups in rodents by simply observing maximum moment arm magnitudes [14] and thus was analyzed in both knee flexion/extension, hip flexion/extension and hip rotation instead of just at its proposed primary function. Once again like the PLANT and LG, tibia translation is apparent in the perturbations viewed in Figure 3.15.

SM has similar characteristics and location to ST, but has a muscle path that is much more convoluted and thus features only effects from wrapping surfaces. During hip adduction in Figure 3.14, there appeared to be a large fluctuation in the moment arm between -30 to -20 degrees. This is a result of minimal constraints from removing other wrapping surfaces allowing the MTU path to wrap on multiple sides of a single wrapping surface, jumping from medial to lateral between -40 to -20 degrees. During hip adduction, all wrapping surfaces are necessary to prevent this, except when completely removing the spherical wrapping at the trochanter. For hip rotation, the deletion of the wrapping surface preventing the muscle from penetrating the pelvis results in very large sensitivity. Although, due to its path near 0, looking at percent change is not relevant as it will result in infinitely large percentages. Complete removal of wrapping surfaces may have not been ideal in all wrapping surfaces, such as the wrapping at the pelvis and may have been more beneficial to adjust relative diameter sizes. Moreover, removal of other smalling wrapping resulted in zero change in moment arm results (Figure 3.14 B).

Analyses were also conducted on previously defined adductors in the rodent hindlimb. This group was difficult to see in microCT imaging and therefore origins and insertion points relied more heavily on other data. Additionally, although named as adductors, these muscles feature moment arms that peak at hip extension rather than hip adduction in the jerboa. Phylogeny that allows the jerboa to walk on two limbs may result in a constraint that eradicates the need for heavy adductor muscles such as in mice. This is also seen in some adductors in the OS chimp model [8]. Adductors did not show on average a larger percent change with respect to other muscle groups relative to the distance shifted.

Overall, the sensitivity analysis showed that muscle modeling is reliant on many parameters and that perturbations in these parameters can result in large effects in model output, such as the 43% increase in moment arms when perturbing the PLANT VP 1. The analysis also informed us that these effects are variable and dependent on the muscle and location. In general results showed that changes to insertions often had larger effects on moment arm output at the joint of interest than movement of origins. This is likely since insertions are often closer to joint centers of interest for muscles and thus results in a greater effect to moment arms at the corresponding joint by causing larger displacement of the muscle line of action from the joint center. This phenomenon can be seen reversed when looking at the knee joint for biarticular muscles such as LG and PLANT or the hip joint for RF, where changes to origins resulted in greater effects to moment arm magnitudes than insertions. In the jerboa hindlimb, origins were observed often to be much broader and more muscular than insertions, meaning bounds of uncertainty tended to be larger than those chosen for insertion (except in the case of the BFA that features a large insertion site). Insertions often ended at very thin tendinous points that were more easily isolated, especially for the jerboa that has no muscles in the foot. Therefore, although insertions had much greater effect on moment arm results when changed, confidence in insertion location was also greater than origins. Higher sensitivity to more defined parameters and insensitivity to parameters with higher uncertainty allows more confidence in both parameters. In addition, many muscles in the jerboa follow convoluted paths and are constrained by VPs and wrapping surfaces which proved important to investigate. Although important for the reasons mentioned above, results showed that only VPs after origins or directly before insertions could affect moment arm magnitudes of nearby joints. VPs anywhere in between appear to have zero effect on moment arm results even when completely removed from the model. We notice this when observing knee extensor moment arms at the knee, where changing origins has zero effect on moment arm magnitudes at the knee. Each of these muscles has a VP constraining the center line of action after the origin but before the knee joint, which alters the path permanently regardless of the changes in origin. We can see this with the PLANT as well, where when VPs two to nine are removed, the moment at the ankle joint is unaffected. The same is not true for the TA, due to the targeted VPs traveling over the joint center rather than after or before. This provided the reasoning behind observing changes to location in the first VP or that closest to the proximal or distal side of the joint. Moving this point at the PLANT showed it can result in very large (43%) changes in moment arm results, putting much more weight on choosing proper VPs than origins and insertions for muscles following paths like the PLANT or TA.

Investigation of wrapping surfaces showed that in most muscles that were perturbed, effects caused by wrapping were typically lower than either origins or insertions. There were large effects when wrapping surfaces were observed near joint centers of interest, with muscles wrapping over the largest area (depending on if it is an ellipse or cylinder). For example, VL showed about 32% change and AM showed about 25% change in moment arm in these cases. Other knee extensors such as RF and VM have identical wrapping cylinders at the condyles of the femur that were also changed identically but only resulted in a maximum of 7% change. Both RF and VM wrap more medially to the surface and thus the line of action is not affected as greatly as VL is when the diameter of the cylinder is changed. Many wrapping surfaces even resulted in zero or close to zero changes to the moment arm when completely removed, such as BFA or PLANT at the ankle. Semimembranosus showed that changes really depend on the motion of interest and the size of the wrapping surface. The orientation of the wrapping surfaces resulted in close to no effects during flexion and extension when completely removing the wrapping. However, during rotation and adduction, the largest wrapping surface at the pelvis has the greatest effect on changes in moment arms. Although completely removing wrapping surfaces may have been ambitious, results showed small wrapping surfaces had effects that were smaller than anticipated. Due to the variability in size and shape of wrapping surfaces, their effects will depend on the muscle it was modeled for. Wrapping surfaces are very muscle specific, and no general rule about their effects on moment arms can be applied aside from in relation to their proximity and size. Wrapping surfaces that are further from the joint of interest will have a reduced effect on change to the line of action and thus smaller effects on moment arms results. Wrapping surfaces that are larger in size will cause increases in moment arms whereas smaller in size will do the opposite.

Previous OS models conducting sensitivity analyses on muscle path parameters featured results that showed variability in both muscles and among parameters. These studies featured analyses with much fewer muscles and parameters, but in general it was found that moment arms were more sensitive to fluctuations in insertions with the exception of biarticular muscles. It was also shown that wrapping surfaces were never the main contributor to the largest change in moment arm magnitude. Moving points away from a joint increased the moment arm and moving closer decreased the moment arm [8,14].

Although it is important to determine the muscle attachment points to the highest degree possible, the above results (Figure 3.18) showed that the jerboa model featured percentage changes where more than 50% of all changes fell below 10% offsets from original data. Unsurprisingly, as mentioned before, changes to insertion points featured the largest percentage difference on average, over twice as large as origin changes, warranting confidence in the model due to the nature of insertion points and their certainty. In many of the wrapping surface changes, wrapping was completely deleted, and percentage changes still fell within the lowest of the 4 parameters, which is favorable due to the subjectivity of wrapping creation between muscles and individuals generating the surfaces. VPs showed bounds of 75th percentile at higher percentages than any other group. This would indicate a need for higher certainty and precision in selection of VPs, but it’s important to note the smaller dataset of 14 adjusted VPs when compared to 41 points for insertion. Although VPs feature a need for higher certainty than origins, they are also more easily distinguishable than origins. As VPs function is to constrain the line of action to the center of the muscle, this can often be calculated mathematically from a muscle mesh, or selected with smaller degree of uncertainty as they follow more well-defined tendon paths in the jerboa. Previous results also suggested that VPs following previously generated points have no effect on moment arms, putting more weight on selecting a single VP rather than a following set of 9. Insertions have very large outliers, both of which fall under AM during hip rotation and VM during knee flexion-extension. VM features a very large percent change when shifting insertion as the largest difference crosses zero and into negative moment arms (Figure 3.12 D). The differences near zero create an illusion of large percentage change as the number becomes infinitely small. For AM, (Figure 3.17 B) this percentage difference is explained by the same phenomena, where the moment arm crosses zero generating a misleadingly large change, which is amplified by the shift in MTU path over the AM wrapping surface. Few other plots such for PLANT, TA, and ST features percent differences that were on the order of 1000% and were eliminated by selected differences that did not cross zero within the same graph.

After confirming that insertions resulted in the overall largest average percentage differences in moment arm results, insertion data was separated across different joints. The hip featured the largest average difference in addition to a larger distribution than ankle and knee flexion/extension. Hip adduction had a small range of percentages limited to 30-50%, but also incorporated only three points. Hip rotation followed with five points, had a larger range with a larger distribution. Hip flexion had slightly more with nine points, with a distribution similar to rotation, with a larger maximum at 100%. This large difference is once again attributed to approaching zero on the plot. An outlier at the knee is also attributed to this phenomenon. Although large percentage changes are seen in the overall model evaluation, these large differences are largely isolated to the hip joint. Previous 2D model of the jerboa showed that during extreme vertical leaping, muscles acting at the ankle joint contributed to the most work to produce energy [20]. In addition, it showed these muscles exhibited much higher mean peak stresses than any other muscle analyzed. The knee joint followed next for the joint with the second highest work produced in the hindlimb. Overall insertion changes feature the largest average differences in changes, and yet appear to have a low percentage difference at two joints that feature the largest contribution to extreme performance in the jerboa. Facilitating confidence in the model's ability to accurately depict sagittal plane motion and contributors to high performance movement like vertical leaping.

4.2 Functional Groups

Since muscles in the jerboa have never been characterized, little was known about their functional capabilities, or primary function during movement. Previous models have shown that to determine such, plots for muscle moment arm vs joint range of motion are calculated in OS. Muscles were then grouped or classified into functional roles based on the joint motion in which it had the greatest moment arm [14]. This is based on a moment arm quantifying a muscle's effectiveness at creating a movement. However, it has been shown that moments produced at joints are dependent on both the moment arm as well as the applied force, and this will change in a non-linear fashion depending on the amount of muscle activation, and speed of contraction [33,34]. This results in the notion that when a muscle moment is maximal, it may not necessarily result in a moment arm or muscle force that is maximal [35]. The previous, combined with other oversights such as muscles rarely acting in isolation to produce a movement create discrepancies when attempting to characterize muscles with a single primary function leading to the following conclusions. Using moment arms can be a generous form of quantifying basic relationships between form and function or for hypothesizing muscle function and evolution [36,37]. However, OS moment arms feature more integrative ways to be used in musculoskeletal modeling and simulation, such as quantification of sensitivity to embedded parameters and potential effects that result in varying locomotor patterns as seen in Section Chapter 33.3 [8,14,28]. For more discussion and analysis of functional muscle groups in the jerboa using the "JerboaSim" model, refer to the following dissertation ("Musculoskeletal modeling and functional characterizations of hindlimb muscles of a bipedal jerboa", 2023).

4.3 Muscle Architecture

Muscles bridge the gap between central nervous system control and whole-body movement [33]. In order to run muscle driven simulations that can synthesize and output quantities that are nearly impossible to measure such as force development, activation dynamics or muscle-tendon contractile dynamics, the model must be able to incorporate a mathematical model capable of representing musculotendon units. OS implements generic hill-type muscle models [33,34,38] to depict dynamics of muscle activation and force production. The model consists of an elastic element typically representing muscle tendon, that is in series with a contractile element arranged in parallel with one elastic element which are generally equated to properties of muscle fibers [2,8]. Both are approximations, and rely on four muscle parameters; optimal fiber length, tendon slack length, pennation angle and max isometric force, that can be derived from experimental measurements to represent muscles of different size, strength and structure [2].

Previous research that analyzed the vertical leaping of jerboa used morphological measurements from three jerboa, assumed morphological measurements and scaled the data for a mass of 62.72 grams [20]. Mass, fiber length, and pennation angle were measured for each jerboa in the study, however the details of the measurement techniques were not documented. Depending on whether the specimen is fixed or fresh, mass measurement techniques will vary, often accounting for shrinkage of muscles during fixation or variable saturation of muscles during dissection [39,40]. Fiber length, often referred to as optimal fiber length, involves immersing muscle tissue in an acidic solution for a fixed amount of time that depends on the size of the sample. Once the fascia and surrounding structure of muscle tissue is dissolved, muscle fascicles are teased out of the tissue and measured [8,25]. In order to ensure that the fiber is at its optimal length, sarcomere length is typically measured to scale the length and avoid variations to fiber length caused by muscle or fiber stretch/shrink that occurred during dissection or fixation [41]. In the above study, it is likely the fiber length was measured by measuring the whole muscle rather than the previously more accepted description. Pennation angle appeared to be measured directly on live muscle, but description of averaging or multiple measurements was unclear. It is shown that in many mammals, pennation angle will vary along the length of a muscle and thus determination of a single value is not often able to capture the internal heterogeneity of a muscle [28]. This is both a limitation in modeling and experimental measurement, but can be compensated by using various averaging approaches as it has been shown that changes in pennation have the least effect on muscle force production in musculoskeletal models relative to other parameters [8,42]. Tendon slack length was not calculated in this study, likely due to the fact that this is a parameter that cannot be measured *in-vivo,* and is derived from force length curves and generally viewed as an abstract concept unique to musculoskeletal models to describe in-series elasticity of a MTU [8,14]. For all the reasons stated above and potential unknowns that using the data could cause in model output due to its ambiguity in collection, the architecture was not used or scaled for our model.

4.4 Limitations/Assumptions

Limitations do not invalidate models, but rather help us better interpret the data that is outputted from them. Early limitations began with scan quality and tendon visibility. Although the initial scan was conducted at nine microns, this resulted in a scan size of 450gb and proved impossible to conduct timely segmentations. Downsizing the scan to 35 microns drastically reduced the scan quality, which in turn resulted in difficulty to distinguish muscle boundaries. The use of similar semi-automated tools conducted with bone was attempted for muscle segmentation, but due to the lack of contrast between neighboring muscles and the ambiguity in identifiable features, manual segmentation was required for the vast majority of muscles in the hindlimb. This may be a direct cause of a few muscles being segmented as groups as detailed in Section Chapter 33.1. Grouping muscles made it difficult to individually identify origins and insertions, but for the same reason, micro-dissections and literature were referenced to clarify these points. Furthermore, analyses were conducted specifically on a few muscles in the adductor group to identify sensitivities to these parameters. The Lugol staining of the specimen allowed muscle contrast but failed to more clearly capture tendons. Tendon staining would have been ideal to capture insertions, but instead bony landmarks and microdissections were referenced once again for these points.

Assumptions that were also implemented while constructing the model include rigid bodies instead of deformable bodies. This is often an accepted assumption in whole body musculoskeletal models, that limits bones to no stretch, compression or bending when subjected to load. Although the deformability in the jerboa skeleton is not studied in detail, little effect on analyses when studying muscle activation patterns is likely to occur. Rigid bodies are great for computational efficiency and deformability would only lend more insight in the event of a finite element stress and strain investigation. The creation of joints involved many joints with which joints centers were “constant”. Physiological joints do not have true centers of rotation and point of contact can depend on the motion or load applied. A center of rotation was chosen for the hip joint, and the ankle joint. Although this is not true to the physiology, small movement within the joint would unlikely cause significant effects to moment arm results or maximal moments about joint centers. Additionally, modeling movement at these joints, particularly that of the tarsals near the ankle joint would require detailed data to accurately translate into the model. This assumption was not sufficient to prevent bone penetration in the knee or patellofemoral joint but data was more attainable for this exposed joint and thus tibial and patellar translation with knee angle was defined.

In this study, the accompaniment of muscle architecture and contractile parameters of the specimen scanned were not provided, as neither the currently measured dataset, or previous literature was complete or robust. The dissection data was well documented and therefore in the future max isometric force, tendon slack length, and pennation angle could be calculated from the stored images and weights as shown in previous literature [25,41,43]. Optimal fiber length could be substituted from another specimen if access to the previously dissected sample is not possible. Scaling the data to the original specimen imaged in the microCT would be required in order to input the parameters into the musculoskeletal model following previously accepted techniques [28].

Furthermore, due to the detailed documentation during construction of the model, scaling parameters that are collected in the future would be anything but ambitious. Collection from multiple specimens would allow for a larger sample size, expertise of data collection and averaging of the data. When observing another important aspect of the musculoskeletal model, details of muscle modeling are key to achieving accurate results. In OS, muscles are modeled down to a single MTU, represented by a four parameter hill-type model. Many assumptions and limitations have been detailed regarding this form of muscle modeling, often in relation to simplification of parameters, material properties of tendon or muscle that are ignored but these assumptions are well documented by OS and previous models have shown hill type models are sufficient at representing changes in muscle force with changes in length and velocity [2,34].

Validation of models before their use is crucial, and although the above study did not provide validation for model outputs, sensitivity analyses detailing the uncertainty and sensitivities of input parameters paved the way for investigation of moment validation with the inclusion of muscle contractile parameters. In the past, many models have used other existing models to validate moment arms, like in the case of mouse and rat, rat and cat, or chimp and human [7,8,13,14]. However, due to the novelty of the jerboa's skeletal form, muscle moment arms are not expected to fall within ranges of currently published 3D models, and there are no detailed moment arm values in literature over joint ranges of motion to sufficiently compare. Additionally, techniques for evaluating moment arms in OS are documented to be solved differently than other methods typically used experimentally, and thus could also result in values that are different without meaningful result. Therefore, validation of muscle moments rather than moment arms with *in-vivo* torque validations on live jerboa could present the best option for comparison of such values.

The above limitations are stated to better help future users of the musculoskeletal model further evaluate impact on specific questions but have been considered in the light of evaluating the model for muscle forces and pattern activations in complex movement.

4.5 Future work

Future work could pair the model with collected muscle architecture data and provide contractile parameter inputs for the 32 developed muscles. With such values present, steps towards moment validation and torque evaluations on live animals to corroborate outputs from the model are clear. After model validation, collection of kinematic data featuring jerboa locomotion of interest would allow for further investigation of such movements. The use of high-speed cameras to capture extreme vertical leaping or maneuvers used for outsmarting predators would be paired with ground reaction forces to allow for inverse dynamics analyzes in OS resulting in moments about joints and muscle forces through static optimization to solve the muscle redundancy problem. Ideally, high-speed video would be captured in the jerboas natural habitat, as lab settings have behavioral and physiological constraints that can influence outcome of complex or extreme motion [20]. Studies have shown success using video editing software such as deeplabcut to track positions on the body of a jerboa, and this same data can be used as inputs to inverse dynamics simulations [19]. Additionally, extending the model to feature muscles in the tail and studying the potential coupling of the tail and hindlimb could be essential for the future to incorporate additional sources of stability and agility of the jerboa.

Modeling the extreme vertical leaping observed in live animals would be especially informative in the detailed quantification of muscles or muscle groups responsible for maximal performance. Model comparison of previously categorized gait cycles could verify the limb kinematic interactions and help further understand the development of smooth transitions between cycles. Leveraging the diversification of their unique limb morphology from that of rodents that have already been modeled could even provide insight into the evolution of bipedalism and corresponding biomechanical function [17,44]. Bridging the gap between morphological form and biomechanical function has vast applications in the field of human performance. Quantification and understanding of activation patterns that allow jerboa to maintain stability during complex and abrupt movements could inform athletes on better techniques or training to help prevent injury [3]. More detailed or accurate investigations of gait transitions could help inform the movement and creation of robotic assistive devices that often have difficulty with smooth gait transitions [19]. Finally, having a model of an obligate bipedal rodent could be more informative in disease studies related to human hip and knee osteoarthritis than those done in quadrupedal animals.

Chapter 5 : Conclusions

Creating a 3D jerboa hindlimb musculoskeletal model is beneficial for being able to investigate muscle force, joint loads and moments that may not be achievable through experimental data collection alone. The development of the model involved funneling inputs from high resolution imaging, dissections, and computation analyses to generate a multi-joint rigid body musculoskeletal system where muscles are approximated with attachment points, and geometric techniques are used to modify their line of action. Model evaluation of moment arms results for 11 muscles in the hindlimb pointed to increased sensitivity in insertion points about the hip and increased confidence for model outputs at the ankle and knee where the most work is produced during high performance locomotion. With the addition of muscle contractile properties and kinematic data of jerboa, this framework allows for the investigation of muscle activation patterns and forces to lend information to the evolution of bipedalism, creation of smooth gait transitioning for robotic devices, and ultimately to investigate how unique biomechanical form leads to extreme locomotor function.

REFERENCES

(1) Neptune, R. R.; McGowan, C. P.; Kautz, S. A. Forward Dynamics Simulations Provide Insight into Muscle Mechanical Work during Human Locomotion. *Exerc. Sport Sci. Rev.* **2009**, *37* (4), 203–210. https://doi.org/10.1097/JES.0b013e3181b7ea29.

(2) Uchida, T. K.; Delp, S.; Delp, D. B. *Biomechanics of Movement: The Science of Sports, Robotics, and Rehabilitation*; The MIT Press: Cambridge, Massachusetts, 2020.

(3) McErlain-Naylor, S. A.; King, M. A.; Felton, P. J. A Review of Forward-Dynamics Simulation Models for Predicting Optimal Technique in Maximal Effort Sporting Movements. *Appl. Sci.* **2021**, *11* (4), 1450. https://doi.org/10.3390/app11041450.

(4) De Groote, F.; Falisse, A. Perspective on Musculoskeletal Modelling and Predictive Simulations of Human Movement to Assess the Neuromechanics of Gait. *Proc. R. Soc. B Biol. Sci.* **2021**, *288* (1946), 20202432. https://doi.org/10.1098/rspb.2020.2432.

(5) Seth, A.; Hicks, J. L.; Uchida, T. K.; Habib, A.; Dembia, C. L.; Dunne, J. J.; Ong, C. F.; DeMers, M. S.; Rajagopal, A.; Millard, M.; Hamner, S. R.; Arnold, E. M.; Yong, J. R.; Lakshmikanth, S. K.; Sherman, M. A.; Ku, J. P.; Delp, S. L. OpenSim: Simulating Musculoskeletal Dynamics and Neuromuscular Control to Study Human and Animal Movement. *PLOS Comput. Biol.* **2018**, *14* (7), e1006223. https://doi.org/10.1371/journal.pcbi.1006223.

(6) Hutchinson, J. R.; Rankin, J. W.; Rubenson, J.; Rosenbluth, K. H.; Siston, R. A.; Delp, S. L. Musculoskeletal Modelling of an Ostrich (Struthio Camelus) Pelvic Limb: Influence of Limb Orientation on Muscular Capacity during Locomotion. *PeerJ* **2015**, *3,* e1001. https://doi.org/10.7717/peerj.1001.

(7) Karabulut, D.; Dogru, S. C.; Lin, Y.-C.; Pandy, M. G.; Herzog, W.; Arslan, Y. Z. Direct Validation of Model-Predicted Muscle Forces in the Cat Hindlimb During Locomotion. *J. Biomech. Eng.* **2020**, *142* (5). https://doi.org/10.1115/1.4045660.

(8) O'Neill, M. C.; Lee, L.-F.; Larson, S. G.; Demes, B.; Stern, J. T., Jr; Umberger, B. R. A Three-Dimensional Musculoskeletal Model of the Chimpanzee (Pan Troglodytes) Pelvis and Hind Limb. *J. Exp. Biol.* **2013**, *216* (19), 3709–3723. https://doi.org/10.1242/jeb.079665.

(9) Rajagopal, A.; Dembia, C. L.; DeMers, M. S.; Delp, D. D.; Hicks, J. L.; Delp, S. L. Full-Body Musculoskeletal Model for Muscle-Driven Simulation of Human Gait. *IEEE Trans. Biomed. Eng.* **2016**, *63* (10), 2068–2079. https://doi.org/10.1109/TBME.2016.2586891.

(10) Stark, H.; Fischer, M. S.; Hunt, A.; Young, F.; Quinn, R.; Andrada, E. A Three-Dimensional Musculoskeletal Model of the Dog. *Sci. Rep.* **2021**, *11*, 11335. https://doi.org/10.1038/s41598-021-90058-0.

(11) Hutchinson, J. R.; Anderson, F. C.; Blemker, S. S.; Delp, S. L. Analysis of Hindlimb Muscle Moment Arms in Tyrannosaurus Rex Using a Three-Dimensional Musculoskeletal Computer Model: Implications for Stance, Gait, and Speed. *Paleobiology* **2005**, *31* (4), 676–701. https://doi.org/10.1666/0094-8373(2005)031[0676:AOHMMA]2.0.CO;2.

(12) Villacís Núñez, C. N.; Ray, A. P.; Cooper, K. L.; Moore, T. Y. Metatarsal Fusion Resisted Bending as Jerboas (Dipodidae) Transitioned from Quadrupedal to Bipedal. *Proc. R. Soc. B Biol. Sci.* **2022**, *289* (1984), 20221322. https://doi.org/10.1098/rspb.2022.1322.

(13) Johnson, W. L.; Jindrich, D. L.; Roy, R. R.; Edgerton, V. R. A Three-Dimensional Model of the Rat Hindlimb: Musculoskeletal Geometry and Muscle Moment Arms. *J. Biomech.* **2008**, *41* (3), 610–619. https://doi.org/10.1016/j.jbiomech.2007.10.004.

(14) Charles, J. P.; Cappellari, O.; Spence, A. J.; Wells, D. J.; Hutchinson, J. R. Muscle Moment Arms and Sensitivity Analysis of a Mouse Hindlimb Musculoskeletal Model. *J. Anat.* **2016**, *229* (4), 514–535. https://doi.org/10.1111/joa.12461.

(15) Cooper, K. L. The Lesser Egyptian Jerboa, *Jaculus Jaculus* : A Unique Rodent Model for Evolution and Development: Figure 1. *Cold Spring Harb. Protoc.* **2011**, *2011* (12), pdb.emo066704. https://doi.org/10.1101/pdb.emo066704.

(16) Eilam, D.; Shefer, G. The Developmental Order of Bipedal Locomotion in the Jerboa (Jaculus Orientalis): Pivoting, Creeping, Quadrupedalism, and Bipedalism. *Dev. Psychobiol.* **1997**, *31* (2), 137–142. https://doi.org/10.1002/(SICI)1098-2302(199709)31:2<137::AID-DEV6>3.0.CO;2-L.

(17) Moore, T. Y.; Organ, C. L.; Edwards, S. V.; Biewener, A. A.; Tabin, C. J.; Jenkins, F. A.; Cooper, K. L. Multiple Phylogenetically Distinct Events Shaped the Evolution of Limb Skeletal Morphologies Associated with Bipedalism in the Jerboas. *Curr. Biol. CB* **2015**, *25* (21), 2785–2794. https://doi.org/10.1016/j.cub.2015.09.037.

(18) Wu, S.; Zhang, F.; Edwards, S. V.; Wu, W.; Ye, J.; Bi, S.; Ni, X.; Quan, C.; Meng, J.; Organ, C. L. The Evolution of Bipedalism in Jerboas (Rodentia: Dipodoidea): Origin in Humid and Forested Environments. *Evolution* **2014**, *68* (7), 2108–2118. https://doi.org/10.1111/evo.12404.

(19) Ding, J.; Moore, T. Y.; Gan, Z. A Template Model Explains Jerboa Gait Transitions Across a Broad Range of Speeds. *Front. Bioeng. Biotechnol.* **2022**, *10*, 804826. https://doi.org/10.3389/fbioe.2022.804826.

(20) Moore, T. Y.; Rivera, A. M.; Biewener, A. A. Vertical Leaping Mechanics of the Lesser Egyptian Jerboa Reveal Specialization for Maneuverability Rather than Elastic Energy Storage. *Front. Zool.* **2017**, *14*, 32. https://doi.org/10.1186/s12983-017-0215-z.

(21) Alexander, R. M. Bipedal Animals, and Their Differences from Humans. *J. Anat.* **2004**, *204* (5), 321–330. https://doi.org/10.1111/j.0021-8782.2004.00289.x.

(22) Schröpfer, R.; Klenner-Fringes, B.; Naumer, E. Locomotion Pattern and Habitat Utilisation of the Two Jerboas Jaculus Jaculus and Jaculus Orientalis (Rodentia, Dipodidae). **1985**, *49* (4), 445–454. https://doi.org/10.1515/mamm.1985.49.4.445.

(23) Saxena, A.; Sharma, V.; Muthuirulan, P.; Neufeld, S. J.; Tran, M. P.; Gutierrez, H. L.; Chen, K. D.; Erberich, J. M.; Birmingham, A.; Capellini, T. D.; Cobb, J.; Hiller, M.; Cooper, K. L. Interspecies Transcriptomics Identify Genes That Underlie Disproportionate Foot Growth in Jerboas. *Curr. Biol.* **2021**, *0* (0). https://doi.org/10.1016/j.cub.2021.10.063.

(24) Moore, T. Y.; Biewener, A. A. Outrun or Outmaneuver: Predator–Prey Interactions as a Model System for Integrating Biomechanical Studies in a Broader Ecological and Evolutionary Context. *Integr. Comp. Biol.* **2015**, *55* (6), 1188–1197. https://doi.org/10.1093/icb/icv074.

(25) Charles, J. P.; Cappellari, O.; Spence, A. J.; Hutchinson, J. R.; Wells, D. J. Musculoskeletal Geometry, Muscle Architecture and Functional Specialisations of the Mouse Hindlimb. *PLOS ONE* **2016**, *11* (4), e0147669. https://doi.org/10.1371/journal.pone.0147669.

(26) Howell, A. The Saltatorial Rodent Dipodomys: The Functional and Comparative Anatomy of Its Muscular and Osseous Systems. *Am. Acad. Arts Sci.* **1932**, *67* (10), 377–536.

(27) Ravi-Embar, P. *Musculoskeletal Modeling and Functional Characterization of Hindlimb Muscles of a Bipedal Jerboa.* [Manuscript in preparation]; 2023.

(28) Bishop, P. J.; Cuff, A. R.; Hutchinson, J. R. How to Build a Dinosaur: Musculoskeletal Modeling and Simulation of Locomotor Biomechanics in Extinct Animals. *Paleobiology* **2021**, *47* (1), 1–38. https://doi.org/10.1017/pab.2020.46.

(29) Wu, G.; Siegler, S.; Allard, P.; Kirtley, C.; Leardini, A.; Rosenbaum, D.; Whittle, M.; D'Lima, D. D.; Cristofolini, L.; Witte, H.; Schmid, O.; Stokes, I. ISB Recommendation on Definitions of Joint Coordinate System of Various Joints for the Reporting of Human Joint Motion—Part I: Ankle, Hip, and Spine. *J. Biomech.* **2002**, *35* (4), 543–548. https://doi.org/10.1016/S0021-9290(01)00222-6.

(30) Cappozzo, A.; Catani, F.; Della Croce, U.; Leardini, A. Position and Orientation in Space of Bones during Movement: Anatomical Frame Definition and Determination. *Clin. Biomech.* **1995**, *10* (4), 171–178. https://doi.org/10.1016/0268-0033(95)91394-T.

(31) Arnold, E. M.; Ward, S. R.; Lieber, R. L.; Delp, S. L. A Model of the Lower Limb for Analysis of Human Movement. *Ann. Biomed. Eng.* **2010**, *38* (2), 269–279. https://doi.org/10.1007/s10439-009-9852-5.

(32) Slykhouse, L.; Zaseck, L. W.; Miller, C.; Humm, J. R.; Alai, A.; Kang, Y. S.; Dooley, C.; Sherman, D.; Bigler, B.; Demetropoulos, C. K.; Reed, M. P.; Rupp, J. D. Anatomically-Based Skeletal Coordinate Systems for Use with Impact Biomechanics Data Intended for

Anthropomorphic Test Device Development. *J. Biomech.* **2019**, *92*, 162–168. https://doi.org/10.1016/j.jbiomech.2019.05.032.

(33) Zajac, F. E. Muscle and Tendon: Properties, Models, Scaling, and Application to Biomechanics and Motor Control. *Crit. Rev. Biomed. Eng.* **1989**, *17* (4), 359–411.

(34) Millard, M.; Uchida, T.; Seth, A.; Delp, S. L. Flexing Computational Muscle: Modeling and Simulation of Musculotendon Dynamics. *J. Biomech. Eng.* **2013**, *135* (2). https://doi.org/10.1115/1.4023390.

(35) Lieber, R. L.; Boakes, J. L. Sarcomere Length and Joint Kinematics during Torque Production in Frog Hindlimb. *Am. J. Physiol.-Cell Physiol.* **1988**, *254* (6), C759–C768. https://doi.org/10.1152/ajpcell.1988.254.6.C759.

(36) Bates, K. T.; Maidment, S. C. R.; Allen, V.; Barrett, P. M. Computational Modelling of Locomotor Muscle Moment Arms in the Basal Dinosaur Lesothosaurus Diagnosticus: Assessing Convergence between Birds and Basal Ornithischians. *J. Anat.* **2012**, *220* (3), 212–232. https://doi.org/10.1111/j.1469-7580.2011.01469.x.

(37) Otero, A.; Allen, V.; Pol, D.; Hutchinson, J. R. Forelimb Muscle and Joint Actions in Archosauria: Insights from Crocodylus Johnstoni (Pseudosuchia) and Mussaurus Patagonicus (Sauropodomorpha). *PeerJ* **2017**, *5*, e3976. https://doi.org/10.7717/peerj.3976.

(38) Delp, S. L.; Loan, J. P.; Hoy, M. G.; Zajac, F. E.; Topp, E. L.; Rosen, J. M. An Interactive Graphics-Based Model of the Lower Extremity to Study Orthopaedic Surgical Procedures. *IEEE Trans. Biomed. Eng.* **1990**, *37* (8), 757–767. https://doi.org/10.1109/10.102791.

(39) Martin, M. L.; Travouillon, K. J.; Fleming, P. A.; Warburton, N. M. Review of the Methods Used for Calculating Physiological Cross-Sectional Area (PCSA) for Ecological Questions. *J. Morphol.* **2020**, *281* (7), 778–789. https://doi.org/10.1002/jmor.21139.

(40) Kikuchi, Y.; Kuraoka, A. Differences in Muscle Dimensional Parameters Between Non-Formalin-Fixed (Freeze-Thawed) and Formalin-Fixed Specimen in Gorilla (Gorilla Gorilla). *Mammal Study* **2014**, *39* (1), 65–72. https://doi.org/10.3106/041.039.0101.

(41) Ward, S. R.; Eng, C. M.; Smallwood, L. H.; Lieber, R. L. Are Current Measurements of Lower Extremity Muscle Architecture Accurate? *Clin. Orthop.* **2009**, *467* (4), 1074–1082. https://doi.org/10.1007/s11999-008-0594-8.

(42) Redl, C.; Gfoehler, M.; Pandy, M. G. Sensitivity of Muscle Force Estimates to Variations in Muscle–Tendon Properties. *Hum. Mov. Sci.* **2007**, *26* (2), 306–319. https://doi.org/10.1016/j.humov.2007.01.008.

(43) Sacks, R. D.; Roy, R. R. Architecture of the Hind Limb Muscles of Cats: Functional Significance. *J. Morphol.* **1982**, *173* (2), 185–195. https://doi.org/10.1002/jmor.1051730206.

(44) Charles, J. P.; Cappellari, O.; Hutchinson, J. R. A Dynamic Simulation of Musculoskeletal Function in the Mouse Hindlimb During Trotting Locomotion. *Front. Bioeng. Biotechnol.* **2018**, *6*, 61. https://doi.org/10.3389/fbioe.2018.00061.

APPENDIX

A: Accessing the Database

All the above-described raw data and inputs are accessible at the following link, with a document labeled "Table of Contents" detailing all the contents of each folder:

https://drive.google.com/drive/folders/1xyufYDNR-6QH8IIsRdQ9Ob5ECSCohF0B

Additionally, the same data is saved to a local network drive that can be accessed using the protocol below:

Windows 11 Procedure:
Current retrieval of data includes using a NAS (network attached storage): Map a network drive to get to it from File Explorer in Windows without having to look for it or type its network address each time.

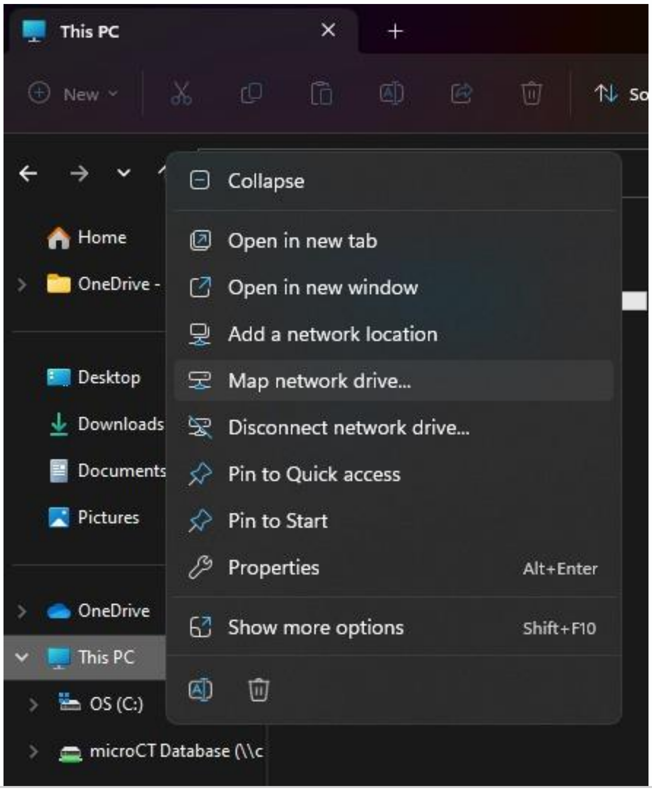

Figure A.1: A window within the library manager to display where to map a network drive in windows 11.

- Open **File Explorer** from the taskbar or the **Start menu**, or press the **Windows logo key +E**.
- Right click **This PC** from the left pane, from the pop-up select **Map network drive.**
- In the **Drive** list, select a drive letter. (Any available letter will do.)

- In the **Folder** box, type the path of the folder or computer, or select **Browse** to find the folder or computer. To connect every time you log on to your PC, select the **Reconnect at sign-in** check box.
- Here input server address: “smb:**cmrg-bioeng-241.ucsd.edu**”
- Select **Browse**
  - Select **cmrg-bioeng-241** Drive
- When prompted for username (email address) and Pin
  - Name: CMRG_Database (case sensitive)
  - Pass: CMl@b (case sensitive)
  - Drive of interest: “microCT Database” (for imaging and human studies)
  - Secondary Drive: "CMRG Backup" (For CMRG data backup)

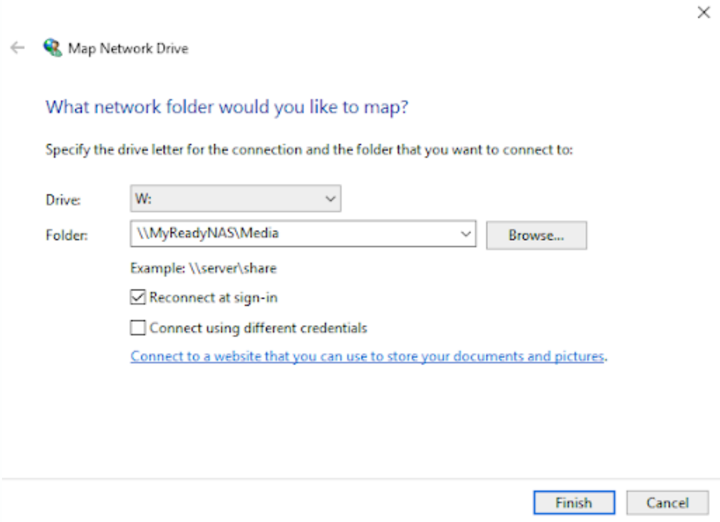

What network folder would you like to map?

Specify the drive letter for the connection and the folder that you want to connect to:

Drive: W:

Folder: \\MyReadyNAS\Media

Example: \\server\share

☑ Reconnect at sign-in

☐ Connect using different credentials

Connect to a website that you can use to store your documents and pictures.

Figure A.2: The second step of mapping the network drive which involves typing the corresponding folder for access. This name should be replaced with the one provided above.

Windows 10 Procedure

Current retrieval of data includes using a NAS (network attached storage):
Map a network drive to get to it from File Explorer in Windows without having to look for it or type its network address each time.

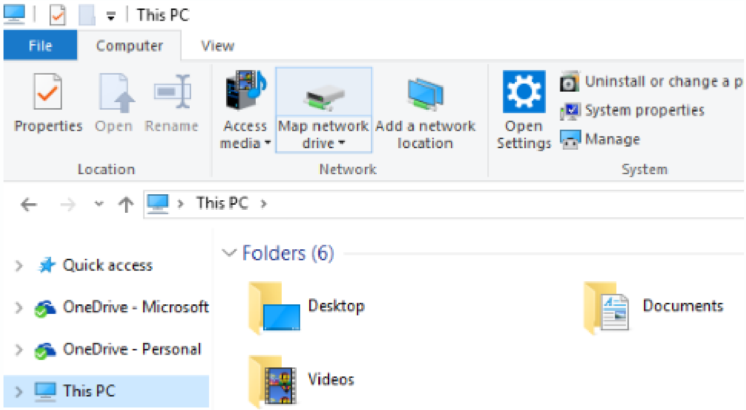

Figure A.3: A window within the library manager to display where to map a network drive in windows 10.

- Open **File Explorer** from the taskbar or the **Start menu**, or press the **Windows logo key +E**.
- Select **This PC** from the left pane. Then, on the **Computer** tab, select **Map network drive.**
- In the **Drive** list, select a drive letter. (Any available letter will do.)
- In the **Folder** box, type the path of the folder or computer, or select **Browse** to find the folder or computer. To connect every time you log on to your PC, select the **Reconnect at sign-in** check box.
- Here input server address: “smb:**cmrg-bioeng-241.ucsd.edu**”
- Select **Browse**
    - Select **cmrg-bioeng-241** Drive
- When prompted for username (email address) and Pin
    - Name: CMRG_Database (case sensitive)
    - Pass: CMl@b (case sensitive)
    - Drive of interest: “microCT Database” (for imaging and human studies)
    - Secondary Drive: "CMRG Backup" (For CMRG data backup)

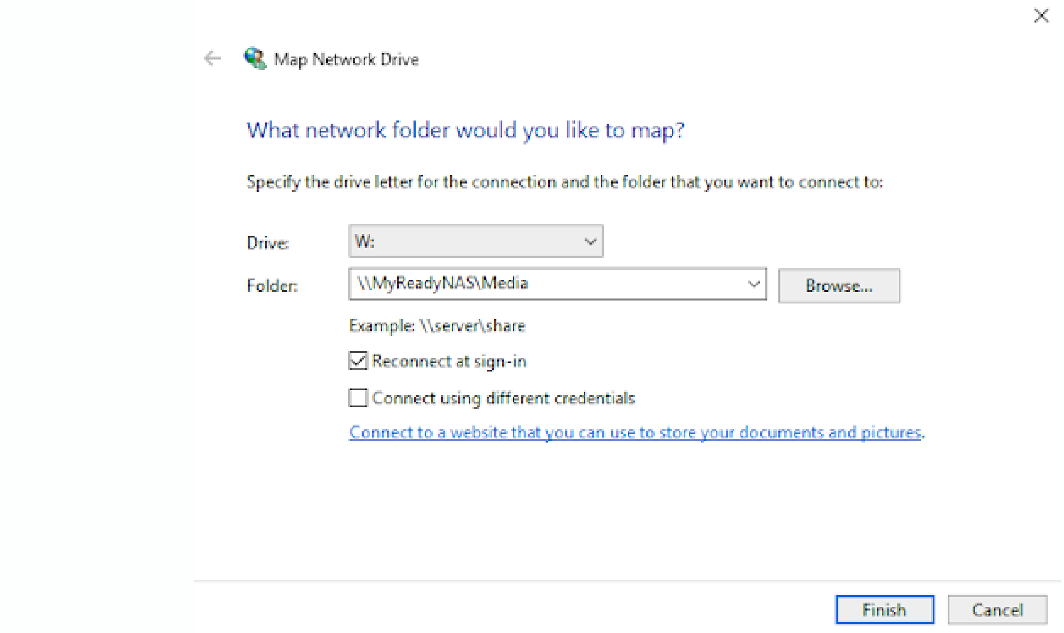

What network folder would you like to map?

Specify the drive letter for the connection and the folder that you want to connect to:

Drive: W:
Folder: \\MyReadyNAS\Media
Example: \\server\share
☑ Reconnect at sign-in
☐ Connect using different credentials
Connect to a website that you can use to store your documents and pictures.

Figure A.4: The second step of mapping the network drive which involves typing the corresponding folder for access. This name should be replaced with the one provided above.

Note: If you can't connect to a network drive or folder, the computer you're trying to connect to might be turned off, or you might not have the correct permissions.

MAC Procedure

Current retrieval of data includes using a NAS (network attached storage):

- If not on UCSD campus and connected to wifi, access and connect to UCSD Cisco VPN. For detailed instructions refer to UCSD Blink.
- Select the Finder window, typically accessed on the bottom left of taskbar or by searching finder in top right search.

Figure A.5: The finder icon that is selected for the first step of accessing the database using a Mac machine.

- After opening the finder, access the "Go" tab on the top and select "Connect to Server" at the bottom of the drop-down menu

Figure A.6: The second step to connecting to a server to access the database on a Mac machine.

- When prompted for a server address, type: "**cmrg-bioeng-241.ucsd.edu**" Drive of interest: "microCT Database"
    - Connect as "Registered User"
    - Name: CMRG_Database (case sensitive)
    - Pass: CMl@b (case sensitive)
    - Click Connect
- Drive of interest: "microCT Database" (for imaging and human studies)
- Secondary Drive: "CMRG Backup" (For CMRG data backup)

B: Model Parameters

Table A-1: Data that is read by the "JerboaModelBuilder" code describing bodies and their associated mass and inertial properties.

Bodies, and Mass Properties									
Bodies	Mass (kg)	Mass_center(x, m)	Mass_center(y)	Mass_center(z)	Inertia(x)kg*m^2	Inertia(y)	Inertia(z)	Mesh name(s)	# of Meshes
Pelvis	4.00E-02	-1.26E-02	-3.91E-03	-6.04E-04	5.84E-07	5.54E-07	2.79E-07	Pelvis_OS.stl	1
Femur_r	2.28E-03	9.82E-04	-7.70E-03	1.83E-03	4.34E-07	3.86E-07	1.28E-07	Femur_OS_r.stl	1
Tibia_r	1.53E-03	9.98E-06	-1.36E-02	6.78E-04	2.30E-07	2.16E-07	3.43E-09	Tibia_OS_r.stl	1
Patella_r	1.07E-05	1	1	1	1	1	1	Pat_OS_R.stl	1
Ankle_r	3.07E-04	1.52E-02	-4.28E-03	2.42E-03	1.27E-07	1.26E-07	1.07E-08	MT_OS_R.stl Calcn_OS_R.stl Ankle_S_OS_R.stl Talus_OS_R.stl T1_OS_R.stl T2_OS_R.stl T3_OS_R.stl T4_OS_R.stl T5_OS_R.stl	9
P6_r	2.49E-05	3.89E-03	-2.73E-04	-8.41E-04	3.16E-10	3.10E-10	1.66E-11	P6_OS_R.stl	1
P4_r	2.67E-05	3.38E-03	-4.81E-04	-4.05E-04	5.48E-10	5.39E-10	1.72E-11	P4_OS_R.stl	1
P2_r	2.85E-05	3.68E-03	-3.42E-04	-1.41E-04	3.33E-10	3.22E-10	2.69E-11	P2_OS_R.stl	1
P5_r	1.78E-05	2.26E-03	-2.32E-04	-2.06E-05	1.01E-11	9.99E-12	1.38E-12	P5_OS_R.stl	1
P3_r	1.51E-05	2.42E-03	-1.82E-04	4.70E-07	1.34E-11	1.31E-11	1.12E-12	P3_OS_R.stl	1
P1_r	1.78E-05	2.33E-03	-1.10E-04	-4.50E-05	2.40E-11	2.36E-11	3.32E-12	P1_OS_R.stl	1
Ungual3_r	1.60E-05	1.61E-03	8.01E-05	-1.17E-04	7.44E-11	6.63E-11	2.22E-11	U3_OS_R.stl	1
Ungual2_r	1.60E-05	1.62E-03	-4.76E-05	4.47E-05	3.79E-12	3.66E-12	6.63E-13	U2_OS_R.stl	1
Ungual1_r	1.51E-05	1.68E-03	8.43E-05	2.05E-04	5.48E-11	4.54E-11	2.01E-11	U1_OS_R.stl	1
Sacrum	1	1	1	1	1	1	1	Sacrum_OS.stl	1
L8	1	1	1	1	1	1	1	L8_OOS.stl	1

Table A-1 cont.

L7	1	1	1	1	1	1	1	L7_OS.stl	1
L6	1	1	1	1	1	1	1	L6_OS.stl	1
L5	1	1	1	1	1	1	1	L5_OS.stl	1
L4	1	1	1	1	1	1	1	L4_OS.stl	1
L3	1	1	1	1	1	1	1	L3_OS.stl	1
L2	1	1	1	1	1	1	1	L2_OS.stl	1
L1	1	1	1	1	1	1	1	L1_OS.stl	1
Ribs	1	1	1	1	1	1	1	Ribs_OS.stl Skull_OS.stl	2
C1	1	1	1	1	1	1	1	C1_OS.stl	1
C2	1	1	1	1	1	1	1	C2_OS.stl	1
C3	1	1	1	1	1	1	1	C3_OS.stl	1
C4	1	1	1	1	1	1	1	C4_OS.stl	1
C5	1	1	1	1	1	1	1	C5_OS.stl	1
C6	1	1	1	1	1	1	1	C6_OS.stl	1
C7	1	1	1	1	1	1	1	C7_OS.stl	1
C8	1	1	1	1	1	1	1	C8_OS.stl	1
C9	1	1	1	1	1	1	1	C9_OS.stl	1
C10	1	1	1	1	1	1	1	C10_OS.stl	1
C11	1	1	1	1	1	1	1	C11_OS.stl	1
C12	1	1	1	1	1	1	1	C12_OS.stl	1
C13	1	1	1	1	1	1	1	C13_OS.stl	1
C14	1	1	1	1	1	1	1	C14_OS.stl	1
C15	1	1	1	1	1	1	1	C15_OS.stl	1
C16	1	1	1	1	1	1	1	C16_OS.stl	1
C17	1	1	1	1	1	1	1	C17_OS.stl	1
C18	1	1	1	1	1	1	1	C18_OS.stl	1
C19	1	1	1	1	1	1	1	C19_OS.stl	1
C20	1	1	1	1	1	1	1	C20_OS.stl	1
C21	1	1	1	1	1	1	1	C21_OS.stl	1
C22	1	1	1	1	1	1	1	C22_OS.stl	1
C23	1	1	1	1	1	1	1	C23_OS.stl	1

Table A-2: Data that is read by the "JerboaModelBuilder" code listing the creation of joints the associated bodies and transformations.

Joint Coordinate System Transformation and Rotation Coordinates														
Joint	Parent body	Child body	Rx (deg)	Ry (deg)	Rz (deg)	Tx (m)	Ty (m)	Tz (m)	Rx name	Ry name	Rz name	Tx name	Ty name	Tz name
ground_pelvis	ground	Pelvis	0	0	0	0	0	0	Pelvic_List	Pelvic_Rotation	Pelvic_Tilt	Pelvis_Tx	Pelvis_Ty	Pelvis_Tz
Hip_r	Pelvis	Femur_r	0	0	0	-0.012004	-0.003653	0.006315	Hip_Rotation	Hip_Adduction	Hip_Flexion	Hip_Tx	Hip_Ty	Hip_Tz
Knee_r	Femur_r	Tibia_r	0	0	0	4.5E-08	-0.0250443	3E-09	Knee_Rx	Knee_Ry	Knee_Rz	Knee_Tx	Knee_Ty	Knee_Tz
Pat_Fem_r	Femur_r	Patella_r	0	0	0	-0.0009569	-0.0263627	-0.0002724	Pat_Rx	Pat_Ry	Pat_Rz	Pat_Tx	Pat_Ty	Pat_Tz
Ankle_r	Tibia_r	Ankle_r	0	0	0	0.000681	-0.045694	0.001582	Ankle_Rx	Ankle_Ry	Ankle_Rz	Ankle_Tx	Ankle_Ty	Ankle_Tz
P6_j_r	Ankle_r	P6_r	0	0	0	0.03489345	-0.0059895	0.00079328	P6_Rx	P6_Ry	P6_Rz	P6_Tx	P6_Ty	P6_Tz
P4_j_r	Ankle_r	P4_r	0	0	0	0.0356704	-0.0060426	-0.0006594	P4_Rx	P4_Ry	P4_Rz	P4_Tx	P4_Ty	P4_Tz
P2_j_r	Ankle_r	P2_r	0	0	0	0.0344849	-0.0062601	-0.0020628	P2_Rx	P2_Ry	P2_Rz	P2_Tx	P2_Ty	P2_Tz
P5_j_r	P6_r	P5_r	0	0	0	0.00753097	0	-0.0017095	P5_Rx	P5_Ry	P5_Rz	P5_Tx	P5_Ty	P5_Tz
P3_j_r	P4_r	P3_r	0	0	0	0.00952811	0	-0.0013148	P3_Rx	P3_Ry	P3_Rz	P3_Tx	P3_Ty	P3_Tz
P1_j_r	P2_r	P1_r	0	0	0	0.00769499	0	-0.0003768	P1_Rx	P1_Ry	P1_Rz	P1_Tx	P1_Ty	P1_Tz
C3_j_r	P5_r	Ungual3_r	0	0	0	0.00388161	0	-0.000124	U3_Rx	U3_Ry	U3_Rz	U3_Tx	U3_Ty	U3_Tz
C2_j_r	P3_r	Ungual2_r	0	0	0	0.00403131	0	-5.717E-05	U2_Rx	U2_Ry	U2_Rz	U2_Tx	U2_Ty	U2_Tz
C1_j_r	P1_r	Ungual1_r	0	0	0	0.00370518	0	2.2787E-05	U1_Rx	U1_Ry	U1_Rz	U1_Tx	U1_Ty	U1_Tz
Sacroiliac	Pelvis	Sacrum	0	0	0	-0.0059036	-0.0018014	8.9123E-05	Sac_Rx	Sac_Ry	Sac_Rz	Sac_Tx	Sac_Ty	Sac_Tz

Table A-2 cont.

L8_j	Sacrum	L8	0	0	0	-0.0002585	-0.0010874	4.1168E-05	L8_Rx	L8_Ry	L8_Rz	L8_Tx	L8_Ty	L8_Tz
L7_j	L8	L7	0	0	0	0.00309714	4.6E-08	4.3017E-05	L7_Rx	L7_Ry	L7_Rz	L7_Tx	L7_Ty	L7_Tz
L6_j	L7	L6	0	0	0	0.00418308	-2.4E-08	8.2381E-05	L6_Rx	L6_Ry	L6_Rz	L6_Tx	L6_Ty	L6_Tz
L5_j	L6	L5	0	0	0	0.00421326	-2.2E-08	-3.397E-05	L5_Rx	L5_Ry	L5_Rz	L5_Tx	L5_Ty	L5_Tz
L4_j	L5	L4	0	0	0	0.00450127	2.6E-08	-0.0002167	L4_Rx	L4_Ry	L4_Rz	L4_Tx	L4_Ty	L4_Tz
L3_j	L4	L3	0	0	0	0.00415226	0.00000004	-0.0003284	L3_Rx	L3_Ry	L3_Rz	L3_Tx	L3_Ty	L3_Tz
L2_j	L3	L2	0	0	0	0.0034359	2.5E-08	-0.000262	L2_Rx	L2_Ry	L2_Rz	L2_Tx	L2_Ty	L2_Tz
L1_j	L2	L1	0	0	0	0.00314899	-4.9E-08	-0.0005704	L1_Rx	L1_Ry	L1_Rz	L1_Tx	L1_Ty	L1_Tz
Ribs_j	L1	Ribs	0	0	0	0.00254128	1.3E-08	-4.636E-05	Ribs_Rx	Ribs_Ry	Ribs_Rz	Ribs_Tx	Ribs_Ty	Ribs_Tz
C1_j	Sacrum	C1	0	0	0	-0.0098343	-0.0010747	-9.403E-05	C1_Rx	C1_Ry	C1_Rz	C1_Tx	C1_Ty	C1_Tz
C2_j	C1	C2	0	0	0	-0.0025206	0.00000001	0.0002028	C2_Rx	C2_Ry	C2_Rz	C2_Tx	C2_Ty	C2_Tz
C3_j	C2	C3	0	0	0	-0.0028493	-2E-08	0.00020322	C3_Rx	C3_Ry	C3_Rz	C3_Tx	C3_Ty	C3_Tz
C4_j	C3	C4	0	0	0	-0.0036599	4E-09	1.537E-06	C4_Rx	C4_Ry	C4_Rz	C4_Tx	C4_Ty	C4_Tz
C5_j	C4	C5	0	0	0	-0.0052838	3.1E-08	0.00030778	C5_Rx	C5_Ry	C5_Rz	C5_Tx	C5_Ty	C5_Tz
C6_j	C5	C6	0	0	0	-0.0090621	0.00000003	-0.0004427	C6_Rx	C6_Ry	C6_Rz	C6_Tx	C6_Ty	C6_Tz
C7_j	C6	C7	0	0	0	-0.0102736	-5.6E-08	0.00046145	C7_Rx	C7_Ry	C7_Rz	C7_Tx	C7_Ty	C7_Tz
C8_j	C7	C8	0	0	0	-0.0101062	6E-09	3.5E-08	C8_Rx	C8_Ry	C8_Rz	C8_Tx	C8_Ty	C8_Tz
C9_j	C8	C9	0	0	0	-0.0105985	-4E-08	0.00045519	C9_Rx	C9_Ry	C9_Rz	C9_Tx	C9_Ty	C9_Tz
C10_j	C9	C10	0	0	0	-0.0100722	5.2E-08	-0.0004782	C10_Rx	C10_Ry	C10_Rz	C10_Tx	C10_Ty	C10_Tz
C11_j	C10	C11	0	0	0	-0.0101497	5.4E-08	-0.0006308	C11_Rx	C11_Ry	C11_Rz	C11_Tx	C11_Ty	C11_Tz
C12_j	C11	C12	0	0	0	-0.0095929	0.00049674	-0.0004259	C12_Rx	C12_Ry	C12_Rz	C12_Tx	C12_Ty	C12_Tz
C13_j	C12	C13	0	0	0	-0.0095057	-1.9E-08	-0.0004474	C13_Rx	C13_Ry	C13_Rz	C13_Tx	C13_Ty	C13_Tz

Table A-2 cont.

C14_j	C13	C14	0	0	0	-0.0092827	4.7E-08	-8.662E-05	C14_Rx	C14_Ry	C14_Rz	C14_Tx	C14_Ty	C14_Tz
C15_j	C14	C15	0	0	0	-0.0083953	-2.1E-08	-0.0008775	C15_Rx	C15_Ry	C15_Rz	C15_Tx	C15_Ty	C15_Tz
C16_j	C15	C16	0	0	0	-0.0080246	2E-09	-0.0004503	C16_Rx	C16_Ry	C16_Rz	C16_Tx	C16_Ty	C16_Tz
C17_j	C16	C17	0	0	0	-0.0074721	4E-09	-0.0002668	C17_Rx	C17_Ry	C17_Rz	C17_Tx	C17_Ty	C17_Tz
C18_j	C17	C18	0	0	0	-0.0071193	4.2E-08	-0.0003203	C18_Rx	C18_Ry	C18_Rz	C18_Tx	C18_Ty	C18_Tz
C19_j	C18	C19	0	0	0	-0.0063918	0	-2.113E-05	C19_Rx	C19_Ry	C19_Rz	C19_Tx	C19_Ty	C19_Tz
C20_j	C19	C20	0	0	0	-0.0056438	-2.3E-08	-0.0002214	C20_Rx	C20_Ry	C20_Rz	C20_Tx	C20_Ty	C20_Tz
C21_j	C20	C21	0	0	0	-0.0051494	3E-09	-0.0001143	C21_Rx	C21_Ry	C21_Rz	C21_Tx	C21_Ty	C21_Tz
C22_j	C21	C22	0	0	0	-0.002118312	-3.6E-08	0.00017593	C22_Rx	C22_Ry	C22_Rz	C22_Tx	C22_Ty	C22_Tz
C23_j	C22	C23	0	0	0	-0.0025065	5.2E-08	0.00062188	C23_Rx	C23_Ry	C23_Rz	C23_Tx	C23_Ty	C23_Tz

Table A-3: Data that is read by the "JerboaModelBuilder" code listing the bounds for joint range of motion and the default angles when opening up the model.

Joint Range of Motion and Default Stance									
Joint	Min Rx (deg)	Max Rx (deg)	Min Ry (deg)	Max Ry (deg)	Min Rz (deg)	Max Rz (deg)	Default Rx	Default Ry	Default Rz
ground_pelvis	-360	360	-360	360	-360	360	0	0	20.625
Hip_r	-22.449979	20.550021	-48.164725	21.835275	-35.979973	70.320027	-5.449979	-21.164725	60.320027
Knee_r	-68.919076	111.080924	-93.538629	86.461371	-149.03181	-41.131814	15.787	1.755	-122.13181
Pat_Fem_r	-157.74912	202.250878	-184.59734	175.402664	-304.50491	30	22.247572	-1.6490628	-77.038556
Ankle_r	-8.049129	-4.049129	-3.601413	0.398587	-40.444504	57.555496	-6.049129	-1.601413	11.975496
P6_j_r	-8.77715	31.22285	-25.724765	14.275235	-61.821035	68.178965	14.75185	-25.724765	-4.468035
P4_j_r	-21.935688	38.064312	-18.163374	21.836626	-63.562598	66.437402	8.064312	-5.222374	-2.386598
P2_j_r	-40.142191	-0.142191	-9.899106	30.100894	-60.400979	69.599021	-7.201191	17.159894	-6.871979

Table A-4 cont.

P5_j_r	-26.688057	-6.688057	0.118388	10.118388	-39.746239	-1.046239	-16.688057	5.118388	-22.146239
P3_j_r	-18.259775	21.740225	-17.500223	22.499777	-106.56647	23.433534	1.740225	2.499777	-41.566466
P1_j_r	-13.665805	46.334195	-16.526338	23.473662	-103.84314	26.156862	12.814195	-5.938338	-31.196138
C3_j_r	-29.640693	-19.640693	-6.574706	3.425294	-6.534342	63.465658	-24.640693	-1.574706	53.465658
C2_j_r	-18.057389	-8.057389	-9.510921	0.489079	4.068657	74.068657	-13.057389	-4.510921	64.068657
C1_j_r	10.754501	20.754501	3.001469	13.001469	-3.309517	66.690483	15.754501	8.001469	56.690483
Sacroiliac	-3	3	-1	1	-10	13	0	0	9.375
L8_j	-10	0	-2	2	-10	15	-7.370222	0.987105	10.826451
L7_j	0	10	-2	2	-30	20	4.921575	-0.741315	-25.137457
L6_j	-10	0	-3	2	-2	7	-7.304173	-1.669792	5.485005
L5_j	-6	13	-4	4	-5	0	10.94474	-2.987793	-3.100088
L4_j	-10	2	-3	2	-3	3	-4.071511	-1.833855	0.22523
L3_j	-3	2	-4	2	-1	7	0.252087	-1.15854	4.853712
L2_j	-3	2	-6	0	-20	2	-0.185933	-4.234008	-16.121665
L1_j	-2	4	0	9	-15	0	3.057054	7.717734	-13.963919
Ribs_j	-20	20	-8	8	-25	0	-9.375	3.75	-19.871626
C1_j	-90	90	-90	90	-90	90	2.821162	1.525	-7.013
C2_j	-90	90	-90	90	-90	90	-0.508	-8.644	-14.02
C3_j	-90	90	-90	90	-90	90	-7.16658	2.542	-10.51
C4_j	-90	90	-90	90	-90	90	1.418107	-0.508	-9.351
C5_j	-90	90	-90	90	-90	90	2.897896	5.593	-0.508
C6_j	-90	90	-90	90	-90	90	15.468915	-4.576	-2.542
C7_j	-90	90	-90	90	-90	90	-13.72833	0.508	12.857
C8_j	-90	90	-90	90	-90	90	-8.077557	-1.525	12.857
C9_j	-90	90	-90	90	-90	90	3.590082	5.593	17.532
C10_j	-90	90	-90	90	-90	90	7.96575	1.525	9.351
C11_j	-90	90	-90	90	-90	90	-0.862621	0.508	10.678
C12_j	-90	180	-90	90	-90	90	-2.338	1.169	17.532
C13_j	-90	90	-90	90	-90	90	-2.34916	1.169	9.351
C14_j	-90	90	-90	90	-90	90	-4.805531	3.559	5.844
C15_j	-90	90	-90	90	-90	90	-7.222525	-0.508	5.844
C16_j	-90	90	-90	90	-90	90	11.167722	-1.525	-1.169

Table A-5 cont.

C17_j	-90	90	-90	90	-90	90	-7.741923	0.508	-22.2
C18_j	-90	90	-90	90	-90	90	7.710287	-1.525	-23.37
C19_j	-90	90	-90	90	-90	90	-13.260092	3.506	-21.03
C20_j	-90	90	-90	90	-90	90	-7.502978	5.844	-18.7
C21_j	-90	90	-90	90	-90	90	19.016526	-3.559	-3.506
C22_j	-90	90	-90	90	-90	90	-14.55057	-6.61	1.169
C23_j	-90	90	-90	90	-90	90	0.000021	13.729	-22.2

Table A-6: Raw data collected from Geomagic providing muscle names, corresponding attachment points and their parent segments.

Muscle Attachment Points from Contrast Coordinate Frame			
Muscle	Point type	Coordinates(x,y,z)	Segment Location
Medial_Gastrocnemius	Origin	0.0346872, -0.0453576, 0.0528664 m	Femur_r
Medial_Gastrocnemius	Insertion	0.0340812, -0.0209862, 0.0129883 m	Ankle_r
Lateral_Gastrocnemius	Origin	0.0376616, -0.0451771, 0.0517976 m	Femur_r
Lateral_Gastrocnemius	Insertion	0.0339756, -0.0211849, 0.0136018 m	Ankle_r
Plantaris	Origin	0.0369556, -0.0445804, 0.0523056 m	Femur_r
Plantaris	via_point_1	0.0340747, -0.0211281, 0.0132195 m	Ankle_r
Plantaris	via_point_2	0.0338395, -0.0198487, 0.0126233 m	Ankle_r
Plantaris	via_point_3	0.0335989, -0.0162089, 0.0167604 m	Ankle_r
Plantaris	via_point_4	0.0330781, -0.0148787, 0.0182746 m	Ankle_r
Plantaris	via_point_5	0.0330084, -0.0137681, 0.0223659 m	Ankle_r
Plantaris	via_point_6	0.0298789, -0.0079998, 0.0499906 m	Ankle_r
Plantaris	via_point_7	0.0295, -0.0069, 0.0522 m	P4_r
Plantaris	via_point_8	0.0284021, -0.0063231, 0.0569114 m	P4_r
Plantaris	via_point_9	0.0274487, -0.0055250, 0.0605905 m	P4_r
Plantaris	via_point_10	0.0268687, -0.0021251, 0.0620246 m	P3_r
Plantaris	Insertion	0.0268296, -0.0022989, 0.0627316 m	P3_r
Soleus	Origin	0.0371610, -0.0382693, 0.0470677 m	Tibia_r
Soleus	Insertion	0.0338837, -0.0212620, 0.0134955 m	Ankle_r
Tibialis_Anterior	Origin	0.0364, -0.0402, 0.0577 m	Tibia_r
Tibialis_Anterior	via_point_1	0.0342363, -0.0186778, 0.0185598 m	Tibia_r
Tibialis_Anterior	via_point_2	0.0330, -0.0180, 0.0201 m	Ankle_r
Tibialis_Anterior	via_point_3	0.0325, -0.0172, 0.0216 m	Ankle_r
Tibialis_Anterior	Insertion	0.0321, -0.0160, 0.0235 m	Ankle_r
Extensor_Digitorum_Longus	Origin	0.0376009, -0.0408997, 0.0565672 m	Tibia_r
Extensor_Digitorum_Longus	via_point_1	0.0354192, -0.0195065, 0.0187586 m	Tibia_r
Extensor_Digitorum_Longus	via_point_2	0.0341, -0.0171, 0.0206 m	Ankle_r
Extensor_Digitorum_Longus	via_point_3	0.0336975, -0.0163780, 0.0231594 m	Ankle_r
Extensor_Digitorum_Longus	via_point_4	0.0327201, -0.0145211, 0.0297022 m	Ankle_r
Extensor_Digitorum_Longus	via_point_5	0.0314342, -0.0116586, 0.0406772 m	Ankle_r
Extensor_Digitorum_Longus	via_point_6	0.0308, -0.0105, 0.0453 m	Ankle_r

Table A-7 cont.

Extensor_Digitorum_Longus	via_point_7	0.0300020, -0.0092072, 0.0497651 m	Ankle_r
Extensor_Digitorum_Longus	via_point_8	0.0296728, -0.0085123, 0.0520946 m	Ankle_r
Extensor_Digitorum_Longus	via_point_9	0.0274153, -0.0063764, 0.0609121 m	P4_r
Extensor_Digitorum_Longus	via_point_10	0.0270495, -0.0040602, 0.0618382 m	P3_r
Extensor_Digitorum_Longus	Insertion	0.0266978, -0.0028219, 0.0628565 m	P3_r
Flexor_Digitorum_Longus	Origin	0.0358643, -0.0416400, 0.0544087 m	Tibia_r
Flexor_Digitorum_Longus	via_point_1	0.0344684, -0.0326025, 0.0378907 m	Tibia_r
Flexor_Digitorum_Longus	via_point_2	0.0321729, -0.0205445, 0.0181601 m	Tibia_r
Flexor_Digitorum_Longus	via_point_3	0.0322680, -0.0185821, 0.0172584 m	Ankle_r
Flexor_Digitorum_Longus	via_point_4	0.0320703, -0.0172982, 0.0170344 m	Ankle_r
Flexor_Digitorum_Longus	via_point_5	0.0318809, -0.0168568, 0.0174825 m	Ankle_r
Flexor_Digitorum_Longus	via_point_6	0.0318390, -0.0168304, 0.0177492 m	Ankle_r
Flexor_Digitorum_Longus	via_point_7	0.0318329, -0.0152596, 0.0222113 m	Ankle_r
Flexor_Digitorum_Longus	via_point_8	0.0323, -0.0133, 0.0284 m	Ankle_r
Flexor_Digitorum_Longus	via_point_9	0.0314673, -0.0113773, 0.0355799 m	Ankle_r
Flexor_Digitorum_Longus	via_point_10	0.0306, -0.0097, 0.0429 m	Ankle_r
Flexor_Digitorum_Longus	via_point_11	0.0297444, -0.0074785, 0.0517789 m	Ankle_r
Flexor_Digitorum_Longus	via_point_12	0.0284021, -0.0063231, 0.0569114 m	P4_r
Flexor_Digitorum_Longus	via_point_13	0.0274487, -0.0055250, 0.0605905 m	P4_r
Flexor_Digitorum_Longus	via_point_14	0.0268687, -0.0021251, 0.0620246 m	P3_r
Flexor_Digitorum_Longus	Insertion	0.0268296, -0.0022989, 0.0627316 m	P3_r
Vastus_Lateralis	Origin	.0313188, -.0429808, .0313653 m	Femur_r
Vastus_Lateralis	via_point_1	0.03232207, -0.0455075, 0.0369967 m	Femur_r
Vastus_Lateralis	via_point_2	0.03583578, -0.0486089, 0.048608964 m	Femur_r
Vastus_Lateralis	Insertion	.0370902, -.0474891, .0565218 m	Patella_r
Rectus_Femoris	Origin	.0259069, -.0463905, .0348008 m	Pelvis
Rectus_Femoris	via_point_1	0.03152358, -0.0479104, 0.04660523 m	Femur_r
Rectus_Femoris	Insertion	.0361783, -.0469238, .0573845 m	Patella_r
Vastus_Medialis	Origin	.0283106, -.0427231, .0342965 m	Femur_r
Vastus_Medialis	Insertion	.0361261, -.0465284, .0576645 m	Patella_r
Vastus_Intermedius	Origin	.0344660, -.0469287, .0463003 m	Femur_r
Vastus_Intermedius	Insertion	.0370171, -.0474979, .0565996 m	Patella_r
Popliteus	Origin	.0385495, -.0442185, .0552544 m	Femur_r
Popliteus	via_point_1	.0334282, -.0377329, .0477406 m	Tibia_r
Popliteus	Insertion	.0332030, -.0370925, .0472014 m	Tibia_r
Gluteus_Maximus_dorsal	Origin	.0259123, -.0550259, .0382281 m	Pelvis
Gluteus_Maximus_dorsal	via_point_1	.0240913, -.0491017, .0348554 m	Pelvis
Gluteus_Maximus_dorsal	via_point_2	.0289825, -.0418700, .0299301 m	Femur_r
Gluteus_Maximus_dorsal	via_point_3	.0292293, -.0415175, .0302450 m	Femur_r
Gluteus_Maximus_dorsal	via_point_4	.0295804, -.0413124, .0307449 m	Femur_r
Gluteus_Maximus_dorsal	via_point_5	.0300888, -.0409952, .0321353 m	Femur_r
Gluteus_Maximus_dorsal	Insertion	.0301216, -.0410130, .0334040 m	Femur_r
Gluteus_Maximus_middle	Origin	.0272041, -.0549063, .0386151 m	Pelvis
Gluteus_Maximus_middle	via_point_1	.0248988, -.0495334, .0359811 m	Pelvis
Gluteus_Maximus_middle	via_point_2	.0290268, -.0418842, .0299236 m	Femur_r
Gluteus_Maximus_middle	via_point_3	.0292293, -.0415175, .0302450 m	Femur_r

Table A-8 cont.

Gluteus_Maximus_middle	via_point_4	.0295804, -.0413124, .0307449 m	Femur_r
Gluteus_Maximus_middle	via_point_5	.0300888, -.0409952, .0321353 m	Femur_r
Gluteus_Maximus_middle	Insertion	.0301216, -.0410130, .0334040 m	Femur_r
Gluteus_Maximus_ventral	Origin	.0276188, -.0538718, .0395394 m	Pelvis
Gluteus_Maximus_ventral	via_point_1	.0254378, -.0498636, .0366971 m	Pelvis
Gluteus_Maximus_ventral	via_point_2	.0290690, -.0418996, .0299199 m	Femur_r
Gluteus_Maximus_ventral	via_point_3	.0292293, -.0415175, .0302450 m	Femur_r
Gluteus_Maximus_ventral	via_point_4	.0295804, -.0413124, .0307449 m	Femur_r
Gluteus_Maximus_ventral	via_point_5	.0300888, -.0409952, .0321353 m	Femur_r
Semitendinosus	Origin	.0258605, -.0375226, .0222746 m	Pelvis
Semitendinosus	Insertion	.0330854, -.0362797, .0488057 m	Tibia_r
Biceps_Femoris_Anterior	Origin	0.0254462, -0.0381442, 0.0223152 m	Pelvis
Biceps_Femoris_Anterior	Insertion	0.0385576, -0.0455604, 0.0555350 m	Femur_r
Semimembranosus	Origin	0.0254252, -0.0381023, 0.0251912 m	Pelvis
Semimembranosus	Insertion	0.0350488, -0.0458814, 0.0567896 m	Femur_r
Biceps_Femoris_Posterior_cranial	Origin	.0261449, -.0392017, .0279546 m	Pelvis
Biceps_Femoris_Posterior_cranial	Insertion	0.0388846, -0.0421729, 0.0549750 m	Tibia_r
Biceps_Femoris_Posterior_mid	Origin	.0259910, -.0389404, .0275718 m	Pelvis
Biceps_Femoris_Posterior_mid	Insertion	0.0391773, -0.0405392, 0.0537747 m	Tibia_r
Peroneus_Longus	Origin	.0388835, -.0417922, .0549055 m	Tibia_r
Peroneus_Longus	via_point_1	.0389281, -.0411216, .0538711 m	Tibia_r
Peroneus_Longus	via_point_2	.0376840, -.0344890, .0428459 m	Tibia_r
Peroneus_Longus	via_point_3	.0357420, -.0290035, .0329154 m	Tibia_r
Peroneus_Longus	via_point_4	.0356135, -.0268881, .0290204 m	Tibia_r
Peroneus_Longus	via_point_5	.0352914, -.0242684, .0245872 m	Tibia_r
Peroneus_Longus	via_point_6	.0348787, -.0213881, .0201784 m	Tibia_r
Peroneus_Longus	via_point_7	.0349271, -.0187016, .0175532 m	Ankle_r
Peroneus_Longus	via_point_8	.0344656, -.0176552, .0186979 m	Ankle_r
Peroneus_Longus	Insertion	.0341137, -.0169518, .0203465 m	Ankle_r
Peroneus_digiti_quarti	Origin	.0386058, -.0422472, .0538353 m	Tibia_r
Peroneus_digiti_quarti	via_point_1	.0384044, -.0415639, .0524029 m	Tibia_r
Peroneus_digiti_quarti	via_point_2	.0373990, -.0390058, .0481246 m	Tibia_r
Peroneus_digiti_quarti	via_point_3	.0366499, -.0356439, .0433271 m	Tibia_r
Peroneus_digiti_quarti	via_point_4	.0361023, -.0330071, .0394720 m	Tibia_r
Peroneus_digiti_quarti	via_point_5	.0351754, -.0285634, .0308442 m	Tibia_r
Peroneus_digiti_quarti	via_point_6	.0345433, -.0239867, .0229847 m	Tibia_r
Peroneus_digiti_quarti	via_point_7	.0346087, -.0211512, .0191922 m	Tibia_r
Peroneus_digiti_quarti	via_point_8	.0349380, -.0186132, .0175910 m	Ankle_r
Peroneus_digiti_quarti	via_point_9	.0343848, -.0172230, .0191664 m	Ankle_r
Peroneus_digiti_quarti	via_point_10	.0340917, -.0170679, .0207121 m	Ankle_r
Peroneus_digiti_quarti	via_point_11	.0325088, -.0152229, .0277695 m	Ankle_r
Peroneus_digiti_quarti	via_point_12	.0317612, -.0128457, .0362622 m	Ankle_r
Peroneus_digiti_quarti	via_point_13	.0300519, -.0093412, .0493861 m	Ankle_r
Peroneus_digiti_quarti	via_point_14	.0296309, -.0084736, .0521066 m	Ankle_r
Peroneus_digiti_quarti	via_point_15	.0285837, -.0073433, .0561832 m	P4_r
Peroneus_digiti_quarti	via_point_16	.0274914, -.0065415, .0605512 m	P4_r

Table A-9 cont.

Peroneus_digiti_quarti	via_point_17	.0273553, -.0062454, .0611705 m	P4_r
Peroneus_digiti_quarti	via_point_18	.0272306, -.0056178, .0614043 m	P3_r
Peroneus_digiti_quarti	via_point_19	.0269511, -.0036485, .0620506 m	P3_r
Peroneus_digiti_quarti	Insertion	.0267988, -.0028501, .0628736 m	P3_r
Pectineus	Origin	.0237872, -.0410451, .0342248 m	Pelvis
Pectineus	Insertion	.0315125, -.0441939, .0404679 m	Femur_r
Iliacus	Origin	.0261048, -.0530800, .0402741 m	Pelvis
Iliacus	Insertion	.0285551, -.0411931, .0353352 m	Femur_r
Adductor_longus	Origin	0.0221002, -0.0385377, 0.0342304 m	Pelvis
Adductor_longus	Insertion	0.0327303, -0.0450278, 0.0435891 m	Femur_r
Gracilis_posterior	Origin	.0199411, -.0350316, .0319407 m	Pelvis
Gracilis_posterior	Insertion	.0330981, -.0373228, .0503410 m	Tibia_r
Adductor_magnus	Origin	.0251504, -.0377633, .0242759 m	Pelvis
Adductor_magnus	Insertion	.0349280, -.0451931, .0466410 m	Femur_r
Adductor_brevis	Origin	.0199656, -.0304928, .0288329 m	Pelvis
Adductor_brevis	Insertion	.0329257, -.0435494, .0395403 m	Femur_r
Gracilis_anterior	Origin	.0214912, -.0373253, .0333659 m	Pelvis
Gracilis_anterior	via_point_1	.0361473, -.0448249, .0577928 m	Patella_r
Gracilis_anterior	Insertion	.0364797, -.0446307, .0578358 m	Patella_r
Obturator_externus	Origin	.0202697, -.0331675, .0298280 m	Pelvis
Obturator_externus	Insertion	.0276702, -.0422553, .0314298 m	Femur_r
Gemellus	Origin	.0247698, -.0393549, .0249900 m	Pelvis
Gemellus	Insertion	.0273812, -.0422388, .0314624 m	Femur_r
Quadratus_femoris	Origin	.0251880, -.0378926, .0261954 m	Pelvis
Quadratus_femoris	Insertion	.0280995, -.0407126, .0359836 m	Femur_r
Gluteus_minimus	Origin	.0258745, -.0465411, .0346913 m	Pelvis
Gluteus_minimus	via_point_1	.0306638, -.0431415, .0302353 m	Femur_r
Gluteus_minimus	via_point_2	.0308454, -.0426216, .0301288 m	Femur_r
Gluteus_minimus	Insertion	.0309437, -.0420478, .0306061 m	Femur_r
Gluteus_medius	Origin	.0267067, -.0541469, .0387015 m	Pelvis
Gluteus_medius	via_point_1	.0290853, -.0426661, .0300508 m	Femur_r
Gluteus_medius	via_point_2	.0292994, -.0420864, .0298913 m	Femur_r
Gluteus_medius	Insertion	.0293630, -.0416782, .0301111 m	Femur_r
Gluteus_superficialis	Origin	.0275316, -.0547000, .0388807 m	Pelvis
Gluteus_superficialis	via_point_1	.0305423, -.0431001, .0302173 m	Femur_r
Gluteus_superficialis	via_point_2	.0307302, -.0425826, .0301109 m	Femur_r
Gluteus_superficialis	Insertion	.0308073, -.0419737, .0305413 m	Femur_r
Gemellus_superior	Origin	.0253564, -.0492522, .0361784 m	Pelvis
Gemellus_superior	Insertion	.0310690, -.0432301, .0306759 m	Femur_r

Table A-10: Data that is read by the "JerboaModelBuilder" code converted from Table A-4, into OS segment systems to describe attachment site locations for each muscle on its appropriate body.

Muscle Attachment points in the OpenSim BCS Frame					
SetName	Point	Body	x	y	z
Medial_Gastrocnemius	Origin	Femur_r	0.000787409	-0.021848804	-0.000613548
Medial_Gastrocnemius	Insertion	Ankle_r	-0.004645998	0.000269739	0.000387912
Lateral_Gastrocnemius	Origin	Femur_r	0.000970966	-0.022085961	0.002537965
Lateral_Gastrocnemius	Insertion	Ankle_r	-0.00406847	0.000562937	0.000301245
Plantaris	Origin	Femur_r	0.000264448	-0.022212899	0.001765133
Plantaris	via_point_1	Ankle_r	-0.004441891	0.000448472	0.000382823
Plantaris	via_point_2	Ankle_r	-0.004797874	-0.000928017	0.000220983
Plantaris	via_point_3	Ankle_r	-0.00010404	-0.003809172	0.000518462
Plantaris	via_point_4	Ankle_r	0.001643934	-0.004892906	0.000196628
Plantaris	via_point_5	Ankle_r	0.005857988	-0.005284847	0.000451881
Plantaris	via_point_6	Ankle_r	0.034208677	-0.006422606	-0.000613501
Plantaris	via_point_7	P4_r	0.000992615	-0.00104337	-0.000122104
Plantaris	via_point_8	P4_r	0.005800391	-0.000552465	-0.00073837
Plantaris	via_point_9	P4_r	0.009643437	-0.000510233	-0.001295977
Plantaris	via_point_10	P3_r	0.00415585	-0.000715559	-2.73E-05
Plantaris	Insertion	P3_r	0.004361108	-1.69E-05	9.03E-06
Soleus	Origin	Tibia_r	0.000738994	-0.010707796	0.001863204
Soleus	Insertion	Ankle_r	-0.004179454	0.000613769	0.000197378
Tibialis_Anterior	Origin	Tibia_r	0.004911635	-0.000788894	6.15E-04
Tibialis_Anterior	via_point_1	Tibia_r	0.00222514	-0.045381317	0.002650227
Tibialis_Anterior	via_point_2	Ankle_r	0.002922846	-0.001517859	-3.61E-05
Tibialis_Anterior	via_point_3	Ankle_r	0.004566773	-0.002081649	-0.000381961
Tibialis_Anterior	Insertion	Ankle_r	0.006663924	-0.002962366	-0.000572472
Extensor_Digitorum_Longus	Origin	Tibia_r	0.003567547	-0.001256466	0.001706187
Extensor_Digitorum_Longus	via_point_1	Tibia_r	0.001487944	-0.044658091	3.68E-03
Extensor_Digitorum_Longus	via_point_2	Ankle_r	0.003487882	-0.002236775	0.001161389
Extensor_Digitorum_Longus	via_point_3	Ankle_r	0.006153788	-0.002534573	0.000966246
Extensor_Digitorum_Longus	via_point_4	Ankle_r	0.012967115	-0.003303142	0.000519596
Extensor_Digitorum_Longus	via_point_5	Ankle_r	0.02432894	-0.00431902	0.000101281

Table A-5 cont.

Extensor_Digitorum_Longus	via_point_6	Ankle_r	0.029113289	-0.004707295	-0.000170919
Extensor_Digitorum_Longus	via_point_7	Ankle_r	0.033776465	-0.005266354	-0.000603928
Extensor_Digitorum_Longus	via_point_8	Ankle_r	0.03620661	-0.005571818	-0.000741456
Extensor_Digitorum_Longus	via_point_9	P4_r	0.009765668	0.000390882	-0.001345736
Extensor_Digitorum_Longus	via_point_10	P3_r	0.002377945	9.09E-05	-5.54E-05
Extensor_Digitorum_Longus	Insertion	P3_r	0.003993472	0.000363479	-0.000154252
Flexor_Digitorum_Longus	Origin	Tibia_r	0.002017004	-0.002866563	-9.00E-05
Flexor_Digitorum_Longus	via_point_1	Tibia_r	0.000907208	-0.021710578	0.000285062
Flexor_Digitorum_Longus	via_point_2	Tibia_r	0.000716591	-0.044946839	0.000318391
Flexor_Digitorum_Longus	via_point_3	Ankle_r	8.23E-05	-1.49E-03	-9.74E-04
Flexor_Digitorum_Longus	via_point_4	Ankle_r	9.05E-05	-0.002801932	-0.001077122
Flexor_Digitorum_Longus	via_point_5	Ankle_r	0.000618245	-0.003172096	-1.20E-03
Flexor_Digitorum_Longus	via_point_6	Ankle_r	0.000887878	-0.003155147	-0.001227845
Flexor_Digitorum_Longus	via_point_7	Ankle_r	0.005539054	-0.003930807	-0.00085009
Flexor_Digitorum_Longus	via_point_8	Ankle_r	1.19E-02	-0.004757184	0.000128833
Flexor_Digitorum_Longus	via_point_9	Ankle_r	1.94E-02	-0.005470322	-0.000132184
Flexor_Digitorum_Longus	via_point_10	Ankle_r	0.026900785	-0.005920729	-0.00044
Flexor_Digitorum_Longus	via_point_11	Ankle_r	0.03606392	-0.006636645	-0.000602466
Flexor_Digitorum_Longus	via_point_12	P4_r	0.005800391	-0.000552465	-0.00073837
Flexor_Digitorum_Longus	via_point_13	P4_r	0.009643437	-0.000510233	-1.30E-03
Flexor_Digitorum_Longus	via_point_14	P3_r	0.00415585	-0.000715559	-2.73E-05
Flexor_Digitorum_Longus	Insertion	P3_r	0.004361108	-1.69E-05	9.03E-06
Vastus_Lateralis	Origin	Femur_r	0.000692619	-0.000750149	0.00522857
Vastus_Lateralis	via_point_1	Femur_r	0.002611998	-0.006468342	0.00357882
Vastus_Lateralis	via_point_2	Femur_r	0.004597373	-0.018695341	1.74E-03
Vastus_Lateralis	Insertion	Patella_r	0.000725863	0.003544743	-1.05E-05
Rectus_Femoris	Origin	Pelvis	-0.008344745	-2.25E-03	6.07E-03
Rectus_Femoris	via_point_1	Femur_r	0.003798228	-0.015050988	-0.001285994
Rectus_Femoris	Insertion	Patella_r	0.001294715	0.002635343	-0.000873534
Vastus_Medialis	Origin	Femur_r	-0.000146192	-0.002158604	0.001352972
Vastus_Medialis	Insertion	Patella_r	0.001423241	0.002165509	-8.88E-04
Vastus_Intermedius	Origin	Femur_r	0.003096407	-0.015909156	0.001627002

Table A-5 cont.

Vastus_Intermedius	Insertion	Patella_r	0.000797637	0.003519584	-8.60E-05
Popliteus	Origin	Femur_r	-0.000313396	-0.025520019	0.002074922
Popliteus	via_point_1	Tibia_r	0.002024887	-0.010799256	-0.00174407
Popliteus	Insertion	Tibia_r	0.002300106	-0.011614091	-0.001852985
Gluteus_Maximus_dorsal	Origin	Pelvis	-0.000234576	0.002280713	0.005903864
Gluteus_Maximus_dorsal	via_point_1	Pelvis	-0.006606088	-0.000223325	4.19E-03
Gluteus_Maximus_dorsal	via_point_2	Femur_r	-0.000424228	0.001596783	0.003815581
Gluteus_Maximus_dorsal	via_point_3	Femur_r	-0.000790519	0.00123564	0.003956063
Gluteus_Maximus_dorsal	via_point_4	Femur_r	-0.001024336	0.000652522	0.004099381
Gluteus_Maximus_dorsal	via_point_5	Femur_r	-0.001461221	-0.000795984	0.004042281
Gluteus_Maximus_dorsal	Insertion	Femur_r	-0.00159004	-0.001963603	0.003561591
Gluteus_Maximus_middle	Origin	Pelvis	1.09E-06	0.001973396	0.007201108
Gluteus_Maximus_middle	via_point_1	Pelvis	-0.005453706	-0.000580935	0.005000865
Gluteus_Maximus_middle	via_point_2	Femur_r	-0.000405883	0.001583429	0.003856709
Gluteus_Maximus_middle	via_point_3	Femur_r	-0.000790519	0.00123564	0.003956063
Gluteus_Maximus_middle	via_point_4	Femur_r	-0.001024336	0.000652522	0.004099381
Gluteus_Maximus_middle	via_point_5	Femur_r	-1.46E-03	-0.000795984	0.004042281
Gluteus_Maximus_middle	Insertion	Femur_r	-0.00159004	-0.001963603	0.003561591
Gluteus_Maximus_ventral	Origin	Pelvis	6.81E-05	0.000597483	0.007647053
Gluteus_Maximus_ventral	via_point_1	Pelvis	-0.004685398	-0.000764699	0.005537653
Gluteus_Maximus_ventral	via_point_2	Femur_r	-0.000386847	0.001568304	0.003894663
Gluteus_Maximus_ventral	via_point_3	Femur_r	-0.000790519	0.00123564	0.003956063
Gluteus_Maximus_ventral	via_point_4	Femur_r	-0.001024336	0.000652522	0.004099381
Gluteus_Maximus_ventral	via_point_5	Femur_r	-1.46E-03	-0.000795984	0.004042281
Semitendinosus	Origin	Pelvis	-0.023657234	-0.001213358	0.006133974
Semitendinosus	Insertion	Tibia_r	0.003852157	-0.010697985	-0.001864769
Biceps_Femoris_Anterior	Origin	Pelvis	-0.023236819	-0.000766743	0.005705645
Biceps_Femoris_Anterior	Insertion	Femur_r	0.000982606	-0.025878719	0.001808071
Semimembranosus	Origin	Pelvis	-0.021033446	-0.002615719	0.005708283
Semimembranosus	Insertion	Femur_r	0.000873778	-0.025601381	-0.001920197
Biceps_Femoris_Posterior_cranial	Origin	Pelvis	-0.018190363	-0.003491934	0.006423935
Biceps_Femoris_Posterior_cranial	Insertion	Tibia_r	0.001488158	-0.001802314	0.002793485

Table A-5 cont.

Biceps_Femoris_Posterior_mid	Origin	Pelvis	-0.018653497	-0.003456293	0.006273151
Biceps_Femoris_Posterior_mid	Insertion	Tibia_r	0.002172955	-0.003645178	0.003368179
Peroneus_Longus	Origin	Tibia_r	0.001769057	-0.002061209	0.002855398
Peroneus_Longus	via_point_1	Tibia_r	0.00177005	-0.003282901	0.003026117
Peroneus_Longus	via_point_2	Tibia_r	0.001570694	-0.016207795	0.003065734
Peroneus_Longus	via_point_3	Tibia_r	0.001088313	-0.027675788	0.002211703
Peroneus_Longus	via_point_4	Tibia_r	0.000787837	-0.032090715	0.002495571
Peroneus_Longus	via_point_5	Tibia_r	0.000645407	-0.037244907	0.00267959
Peroneus_Longus	via_point_6	Tibia_r	0.000745265	-0.042524619	0.002816105
Peroneus_Longus	via_point_7	Ankle_r	0.000165856	-0.001128131	0.001678365
Peroneus_Longus	via_point_8	Ankle_r	0.001498856	-0.001992374	0.001371005
Peroneus_Longus	Insertion	Ankle_r	0.003262392	-0.002425017	0.001172896
Peroneus_digiti_quarti	Origin	Tibia_r	0.000852142	-0.002754219	0.002526043
Peroneus_digiti_quarti	via_point_1	Tibia_r	0.000682336	-0.004343691	0.002462997
Peroneus_digiti_quarti	via_point_2	Tibia_r	0.000658816	-0.00940385	0.001960208
Peroneus_digiti_quarti	via_point_3	Tibia_r	0.000996021	-0.01529907	0.001849724
Peroneus_digiti_quarti	via_point_4	Tibia_r	0.001205992	-0.01999675	0.001804062
Peroneus_digiti_quarti	via_point_5	Tibia_r	0.000420449	-0.02971403	0.001759908
Peroneus_digiti_quarti	via_point_6	Tibia_r	0.000119221	-0.038822361	0.002014923
Peroneus_digiti_quarti	via_point_7	Tibia_r	0.000450128	-0.04350952	0.002605211
Peroneus_digiti_quarti	via_point_8	Ankle_r	0.000217042	-0.001207688	0.001698686
Peroneus_digiti_quarti	via_point_9	Ankle_r	0.002037502	-0.002342168	0.001353069
Peroneus_digiti_quarti	via_point_10	Ankle_r	0.003604072	-0.002249615	0.001162163
Peroneus_digiti_quarti	via_point_11	Ankle_r	0.010963936	-0.002961531	0.000141342
Peroneus_digiti_quarti	via_point_12	Ankle_r	0.019765722	-0.003889105	7.73E-05
Peroneus_digiti_quarti	via_point_13	Ankle_r	0.033377846	-0.005196345	-0.00058693
Peroneus_digiti_quarti	via_point_14	Ankle_r	0.036227818	-0.00561079	-0.000779254
Peroneus_digiti_quarti	via_point_15	P4_r	0.004845324	0.000277465	-0.000682484
Peroneus_digiti_quarti	via_point_16	P4_r	0.009370852	0.000470605	-0.001313131
Peroneus_digiti_quarti	via_point_17	P4_r	0.01005182	0.000321186	-0.001373858
Peroneus_digiti_quarti	via_point_18	P3_r	0.000801709	4.93E-04	-7.96E-05
Peroneus_digiti_quarti	via_point_19	P3_r	0.002850148	7.18E-05	-8.63E-05

Table A-5 cont.

Peroneus_digiti_quarti	Insertion	P3_r	0.003962927	0.000385953	-5.50E-05
Pectineus	Origin	Pelvis	-0.012184831	-0.006076685	4.07E-03
Pectineus	Insertion	Femur_r	0.000839471	-0.009191629	0.001611071
Iliacus	Origin	Pelvis	0.000124821	-0.000515013	0.006157735
Iliacus	Insertion	Femur_r	-0.001763286	-0.003088385	0.001343316
Adductor_longus	Origin	Pelvis	-0.013778238	-0.008062518	0.002445359
Adductor_longus	Insertion	Femur_r	0.001395149	-0.012590378	0.001366024
Gracilis_posterior	Origin	Pelvis	-0.017786055	-9.38E-03	3.51E-04
Gracilis_posterior	Insertion	Tibia_r	0.003800689	-8.85E-03	-2.05E-03
Adductor_magnus	Origin	Pelvis	-0.021959574	-0.002306846	5.43E-03
Adductor_magnus	Insertion	Femur_r	0.001375102	-0.016278657	0.002119349
Adductor_brevis	Origin	Pelvis	-0.023061519	-0.010938962	0.000456213
Adductor_brevis	Insertion	Femur_r	0.000422913	-0.008881056	0.003343982
Gracilis_anterior	Origin	Pelvis	-0.015219339	-0.008470376	0.001857964
Gracilis_anterior	via_point_1	Patella_r	0.000977335	0.000529483	-6.79E-04
Gracilis_anterior	Insertion	Patella_r	0.00097289	0.000365495	-0.000328518
Obturator_externus	Origin	Pelvis	-0.020598435	-0.009487186	0.000705778
Obturator_externus	Insertion	Femur_r	-0.000323431	0.000744312	0.001976336
Gemellus	Origin	Pelvis	-0.02040416	-0.001532897	0.005022329
Gemellus	Insertion	Femur_r	-0.000366589	0.000834641	0.001702778
Quadratus_femoris	Origin	Pelvis	-0.020389253	-0.003417807	0.005483949
Quadratus_femoris	Insertion	Femur_r	-0.00235135	-0.003454454	0.000727647
Gluteus_minimus	Origin	Pelvis	-0.008334835	-0.00206332	0.006035786
Gluteus_minimus	via_point_1	Femur_r	0.00093233	0.000533674	5.07E-03
Gluteus_minimus	via_point_2	Femur_r	0.000444651	0.000594747	0.005337341
Gluteus_minimus	Insertion	Femur_r	-0.000171595	0.000163598	0.005304558
Gluteus_medius	Origin	Pelvis	-0.000415705	0.001318786	0.006722221
Gluteus_medius	via_point_1	Femur_r	0.000357817	0.001385314	0.00376461
Gluteus_medius	via_point_2	Femur_r	-0.000180244	0.00148567	0.004092864
Gluteus_medius	Insertion	Femur_r	-0.000605076	0.001290364	0.004111773
Gemellus_superior	Origin	Pelvis	-0.005474346	-9.13E-04	0.005466428
Gemellus_superior	Insertion	Femur_r	0.001000512	-3.98E-05	0.005247857

Table A-11: Data that is read by the "JerboaModelBuilder" code describing wrapping cylinder locations and size for corresponding muscles.

Muscle Wrapping Cylinders Properties and Transformations											
SetName	Body	Muscle	Wrap Rx (deg)	Wrap Ry (deg)	Wrap Rz (deg)	Wrap Tx	Wrap Ty	Wrap Tz	Radius (m)	Length (m)	Quadrant
MG_shank	Tibia_r	Medial_Gastrocnemius	-7.573	-17.747	-1.753	0.00674	-0.01349	0.001451	0.009765	0.0065019	-x
LG_shank	Tibia_r	Lateral_Gastrocnemius	-1.504714	-10.276686	15.933895	0.006202	-0.0130465	0.00301646	0.009465	0.0065019	-x
MG_condylar	Femur_r	Medial_Gastrocnemius	17.874522	0.002806	-6.794002	1.155E-05	-0.0250484	-4.1285E-05	0.00162565	0.0044804	all
LG_condylar	Femur_r	Lateral_Gastrocnemius	17.874522	0.002806	-6.794002	1.155E-05	-0.0250484	-4.1285E-05	0.00162565	0.0044804	all
PLANT_shank	Tibia_r	Plantaris	-2.412729	0.08498	-50.90051	0.007239	-0.01666	0.000611	0.0100816	0.0040219	all
POP_Tibia	Tibia_r	Popliteus	-0.61528	21.08929	-3.602541	0.0017601	-0.0034115	0.00088306	0.0018395	0.0037978	-x
ST_Tibia	Tibia_r	Semitendinosus	-95.753467	3.580702	-112.34849	0.0029182	-0.010796	-0.0005033	0.0015997	0.0040858	all
SM_Pelvis	Pelvis	Semimembranosus	-72.40199	5.998478	77.917883	-0.018078	-0.0020967	0.0027946	0.004	0.002919	all
SM_Femur	Femur_r	Semimembranosus	-81.466972	-56.344147	-162.32637	0.0010225	-0.0228993	-0.00113487	0.00108995	0.004	-y
PL_ankle	Tibia_r	Peroneus_Longus	-3.79694	4.65477	111.67615	0.0014411	-0.0447083	0.00181442	0.000865	0.005	all
PDQA_ankle	Tibia_r	Peroneus_digiti_quarti	-3.79694	4.65477	111.67615	0.0014411	-0.0447083	0.00181442	0.000865	0.005	all
Iliacus_pelvis	Pelvis	Iliacus	4.495838	-1.19775	-89.529612	-0.012159	-0.0038497	0.00700004	0.001126	0.0025	all
AM_pelvis	Pelvis	Adductor_magnus	-82.617362	6.735342	130.73413	-0.017498	-0.0025501	0.00173735	0.005	0.002	all

Table A-6 cont.

OE_pelvis	Pelvis	Obturator_externus	130.499789	55.545406	108.49742	-0.016324	-0.0027325	0.00199319	0.005	0.005	all
OE_pelvis_2	Femur_r	Obturator_externus	37.516786	-4.330313	-6.572306	-0.000136	-0.0005418	0.00158669	0.001275	0.002	all
G_minimus	Femur_r	Gluteus_minimus	35.586776	22.298674	24.683255	0.0002327	0.00034413	0.00446136	0.0007145	0.003	all
G_medius	Femur_r	Gluteus_medius	35.586776	22.298674	24.683255	0.0002327	0.00034413	0.00446136	0.0007145	0.003	all

Table A-12: Data that is read by the "JerboaModelBuilder" code describing wrapping sphere locations and size for corresponding muscles.

Muscle Wrapping Spheres Properties and Transformations												
SetName	Body	Muscle	Wrap Rx	Wrap Ry	Wrap Rz	Wrap Tx	Wrap Ty	Wrap Tz	Dimensions x (m)	Dimensions y (m)	Dimensions z (m)	Quadrant
POP_Femur	Femur_r	Popliteus	0	0	0	-0.000846695	-0.02461742	0.001520966	0.0007	0.0018	0.0013	z
ST_Pelvis	Pelvis	Semitendinosus	-0.000788	0.000763	-0.000002	-0.023437524	-0.00126377	0.005754231	0.000415	0.000415	0.000415	all
BFA_Pelvis	Pelvis	Biceps_Femoris_Anterior	-0.000788	0.000763	-0.000002	-0.023437524	-0.00126377	0.005754231	0.000415	0.000415	0.000415	all
BFA_Femur	Femur_r	Biceps_Femoris_Anterior	-79.83737	-10.07232	-171.0348	0.001245054	-0.00593955	0.002735198	0.00245	0.00245	0.011	all
BFA_Femur_Epicondyl	Femur_r	Biceps_Femoris_Anterior	-0.000216	-0.000899	0.001133	0.001312899	-0.022758948	0.000743931	0.002525	0.002525	0.002525	all
SM_femur_sphere	Femur_r	Semimembranosus	-0.057615	33.198214	-46.18577	-0.001695633	-0.00337001	0.001645676	0.00124	0.00124	0.00124	all
SM_femur_ellipsoid	Femur_r	Semimembranosus	-100.1029	-2.415508	3.878884	-0.000388116	-0.00057307	0.001488709	0.0007636	0.0007636	0.0026994	all
AB_femur	Femur_r	Adductor_brevis	-0.057615	33.198214	-46.18577	-0.001695633	-0.00337001	0.001645676	0.00124	0.00124	0.00124	all
AM_femur	Femur_r	Adductor_magnus	-80.63938	-15.30294	-56.04961	0.000312166	-0.00534267	0.002435437	0.0025	0.0025	0.00702	all
GP_pelvis	Pelvis	Gracilis_posterior	77.977572	80.348547	-106.2586	-0.024356343	-0.01020644	-0.000034265	0.0021	0.0021	0.003	all
GA_femur	Femur_r	Gracilis_anterior	-116.5371	-62.96925	150.72356	-0.000272183	-0.02478109	-0.001128921	0.0014	0.0014	0.002	-y
OE_sphere_pelvis	Pelvis	Obturator_externus	-58.73661	0.444301	43.624529	-0.013873529	-0.00350969	0.006763623	0.00053665	0.00053665	0.00053665	all
OE_sphere_femur	Femur_r	Obturator_externus	-0.057615	33.198214	-46.18577	-0.001695633	-0.00337001	0.001645676	0.00124	0.00124	0.00124	all

Table A-7 cont.

Gemellus_pelvis	Pelvis	Gemellus	-58.73661	0.444301	43.624529	-0.013873529	-0.00350969	0.006763623	0.0008	0.0008	0.0008	all
BFP_femur_sphere	Femur_r	Biceps_Femoris_Posterior_cranial	-0.057615	33.198214	-46.18577	-0.001695633	-0.00337001	0.001645676	0.00124	0.00124	0.00124	all
RF_Groove	Femur_r	Rectus_Femoris	20.089261	-7.153412	-29.05973	0.000830221	-0.02358619	0.000499479	0.0030764	0.00318	0.00318	x
VL_Groove	Femur_r	Vastus_Lateralis	20.089261	-7.153412	-29.05973	0.000830221	-0.02358619	0.000499479	0.0030764	0.00318	0.00318	x
VI_Groove	Femur_r	Vastus_Intermedius	20.089261	-7.153412	-29.05973	0.000830221	-0.02358619	0.000499479	0.0030764	0.00318	0.00318	x
VM_Medial	Femur_r	Vastus_Medialis	20.089261	-7.153412	-29.05973	0.000830221	-0.02358619	0.000499479	0.0030764	0.00318	0.00318	x

C: JerboaModelBuilder.m Code

```matlab
%% OpenSIM MATLAB API JERBOA MUSCULOSKELETAL MODEL BUILDER %%
% Coded by Yasser Abdelrahman @ UCSD 08/08/22
% This code was written to construct an OSIM file of the Jerboa using data
% from a modifiable XLS sheet.
clear; close all; clc;
%% Section 1.1: Importing appropriate packages and libraries
import org.opensim.modeling.*;
import org.opensim.utils.*;
import java.io.*
import java.swing.*;
import java.lang.*;
%% Declare an empty model
JerboaModel = Model();
%% Creating a Geometry path
% path = 'C:Musculoskeletal ModelingOpensim (stl. & .osim)Geometry'
% ModelVisualizer.addDirToGeometrySearchPaths(path);
%% Section 1.2: Assigning Name, Publication, Units, and Gravity
JerboaModel.setName('Jerboa_SIM');
JerboaModel.set_gravity(Vec3(0, -9.8066499999999994, 0));
JerboaModel.set_credits('This model....');
JerboaModel.set_publications('This model is described in the following paper:....');
JerboaModel.set_length_units('M');
JerboaModel.set_force_units('N');
%% Defining the Ground
% Adding ground
ground = JerboaModel.getGround();
%% Section 1.3: Reading data from xls sheet
%The below code reads from a downloaded google excel sheet, any changes to
%the sheet require re-downloading in order to effect to take place before
%running the code again

Bodies = readtable('Jerboa Model Building.xlsx', 'Sheet', "Bodies", 'VariableNamingRule', 'preserve');
JCS = readtable('Jerboa Model Building.xlsx', 'Sheet', "JCS", 'VariableNamingRule', 'preserve');
```

```
Wraps = readtable('Jerboa Model Building.xlsx', 'Sheet', "Wrapping
Cylinders", 'VariableNamingRule', 'preserve');
Wraps_S = readtable('Jerboa Model Building.xlsx', 'Sheet', "Wrapping
Spheres", 'VariableNamingRule', 'preserve');
Range = readtable('Jerboa Model Building.xlsx', 'Sheet', "Joint Coordinates",
'VariableNamingRule', 'preserve');
MUS = readtable('Jerboa Model Building.xlsx', 'Sheet', "Muscle architecture",
'VariableNamingRule', 'preserve');
MUSPoints = readtable('Jerboa Model Building.xlsx', 'Sheet', "Muscles",
'VariableNamingRule', 'preserve');
%% Section 2.1: Adding Body segments
%Body Segments are added to the model by including Properties of Segments
(Mass, COM, Inertia),
%Appearance(opacity, scale, color) and STL file names from the listed google
sheet. For a body with multiple meshes an if statement was developed.

for i = 1:height(Bodies) %running loop to create all bodies in xls sheet
body = Body();
body.setName(Bodies{i,1});
body.setMass(Bodies{i,2});
body.setMassCenter(Vec3(Bodies{i,3}, Bodies{i,4}, Bodies{i,5}));
body.setInertia(Inertia(Bodies{i,6}, Bodies{i,7}, Bodies{i,8}));
if Bodies{i,10} == 1 %checks the number of mesh's attached to the body
attach_geo_body = Mesh(Bodies{i,9});
body.attachGeometry(attach_geo_body); %adding visible objects based on above
parameters
attach_geo_body.setName(cell2mat(strsplit(cell2mat(Bodies{i,9}), '.stl')))
attach_geo_body.set_scale_factors(Vec3(.001)); %scaling down for mm
else %if it has more than 0 additional meshes attatched
for o = 1:Bodies{i,10}
meshstr = split(Bodies{i,9});
add_geo_body = Mesh(meshstr{o}); %iterate through different meshes
add_geo_body.setName(cell2mat(strsplit(meshstr{o}, '.stl'))); %creates name
by removing '.stl'
add_geo_body.set_scale_factors(Vec3(.001)); %scaling down for mm
body.attachGeometry(add_geo_body); %adding visible objects based on above
parameters
end
end
JerboaModel.addBody(body); % adding body to the model
end

%Generation of joints requires names of the bodies that were added to the
%model, and thus the below is used to call back strings that will list
%Child and Parent Bodies. These strings come from the sheet, or built in
%API functions to retrieve string.
Childbodystr = JCS{:,3};
Parentbodystr = JCS{:,2};
Bodylist = osimList2MatlabCell(JerboaModel, 'Body'); %reading back list of
bodies created above previously
Parentlist{1} = ground; %assigning ground to the first parent index

for j = 2:height(JCS)
A(j) = find(strcmp(Parentbodystr{j}, Childbodystr));
Parentlist{j} = cell2mat(Bodylist(A(j),1));
%This for loop sifts through the strings and will create bodies that
```

```
%opensim code can read by cross referencing strings to the xls sheet.
end

%% Section 2.2: Defining and Adding Joints
%When creating a "CustomJoint" you require spatialtrans function to
%constrain orientation and rotation. The for loop below uses the bodies
%above and creates joints based on parameters in the xls sheet.
%The below includes joints that have fixed points of rotation as well as
%joints that are based on polynomial functions that change body position as
%a function of joint angle (Patellar and Knee Joint)
%% Section 2.2.1: Knee Joint Function
for k = 1:height(JCS)
if k == 3 %Specifically for adding function for knee joint
LocationInParent = Vec3(JCS{k,7}, JCS{k,8}, JCS{k,9});
OrientationInParent =
Vec3(deg2rad(JCS{k,4}),deg2rad(JCS{k,5}),deg2rad(JCS{k,6}));
LocationInChild = Vec3(0);
OrientationInChild = Vec3(0);
spatialtrans_kneejoint = SpatialTransform();
spatialtrans_kneejoint.upd_rotation1().append_coordinates('Knee_Rz');
spatialtrans_kneejoint.upd_rotation1().set_axis(Vec3(1, 0, 0));
spatialtrans_kneejoint.upd_rotation1().set_function(LinearFunction(1, 0));
spatialtrans_kneejoint.upd_rotation2().append_coordinates('Knee_Rz');
spatialtrans_kneejoint.upd_rotation2().set_axis(Vec3(0, 1, 0));
spatialtrans_kneejoint.upd_rotation2().set_function(LinearFunction(1, 0));
simmspline_rotation1 = SimmSpline(); %The below points are what define the
various points along the curve for one axis of the knee joint
simmspline_rotation1.addPoint(deg2rad(-150), deg2rad(15.787));
simmspline_rotation1.addPoint(deg2rad(-137), deg2rad(15.787));
simmspline_rotation1.addPoint(deg2rad(-122), deg2rad(15.787));
simmspline_rotation1.addPoint(deg2rad(-113), deg2rad(15.787));
simmspline_rotation1.addPoint(deg2rad(-98), deg2rad(15));
simmspline_rotation1.addPoint(deg2rad(-82), deg2rad(14.5));
simmspline_rotation1.addPoint(deg2rad(-70), deg2rad(13));
simmspline_rotation1.addPoint(deg2rad(-60), deg2rad(12.5));
simmspline_rotation1.addPoint(deg2rad(-41), deg2rad(12));
spatialtrans_kneejoint.upd_rotation1().set_function(simmspline_rotation1);
spatialtrans_kneejoint.upd_rotation3().append_coordinates('Knee_Rz');
spatialtrans_kneejoint.upd_rotation3().set_axis(Vec3(0, 0, 1));
spatialtrans_kneejoint.upd_rotation3().set_function(LinearFunction(1, 0));
simmspline_rotation2 = SimmSpline();
simmspline_rotation2.addPoint(deg2rad(-150), deg2rad(3));
simmspline_rotation2.addPoint(deg2rad(-137), deg2rad(3));
simmspline_rotation2.addPoint(deg2rad(-98), deg2rad(1));
simmspline_rotation2.addPoint(deg2rad(-82), deg2rad(0));
simmspline_rotation2.addPoint(deg2rad(-70), deg2rad(-2));
simmspline_rotation2.addPoint(deg2rad(-60), deg2rad(-5));
simmspline_rotation2.addPoint(deg2rad(-41), deg2rad(-10.06));
spatialtrans_kneejoint.upd_rotation2().set_function(simmspline_rotation2);
spatialtrans_kneejoint.upd_translation1().append_coordinates('Knee_Rz');
spatialtrans_kneejoint.upd_translation1().set_axis(Vec3(1, 0, 0));
simmspline_translation1 = SimmSpline();
simmspline_translation1.addPoint(deg2rad(-150), 0);
simmspline_translation1.addPoint(deg2rad(-145), 0);
simmspline_translation1.addPoint(deg2rad(-137), 0);
simmspline_translation1.addPoint(deg2rad(-131), -0.000035);
```

```
simmspline_translation1.addPoint(deg2rad(-110), -0.000096);
simmspline_translation1.addPoint(deg2rad(-98), -0.00015);
simmspline_translation1.addPoint(deg2rad(-88), -0.000225);
simmspline_translation1.addPoint(deg2rad(-82), -0.00034);
simmspline_translation1.addPoint(deg2rad(-55.7), -0.001074);
simmspline_translation1.addPoint(deg2rad(-48.7), -0.001313);
simmspline_translation1.addPoint(deg2rad(-41), -0.0015);
spatialtrans_kneejoint.upd_translation1().set_function(simmspline_translation
1);
spatialtrans_kneejoint.upd_translation2().append_coordinates('Knee_Rz');
spatialtrans_kneejoint.upd_translation2().set_axis(Vec3(0, 1, 0));
simmspline_translation2 = SimmSpline();
simmspline_translation2.addPoint(deg2rad(-150), 0);
simmspline_translation2.addPoint(deg2rad(-137), 0.0005);
simmspline_translation2.addPoint(deg2rad(-127), 0.0005675);
simmspline_translation2.addPoint(deg2rad(-113), 0.0006);
simmspline_translation2.addPoint(deg2rad(-81), 0.00062);
simmspline_translation2.addPoint(deg2rad(-60), 0.00064);
simmspline_translation2.addPoint(deg2rad(-41), 0.00065);
spatialtrans_kneejoint.upd_translation2().set_function(simmspline_translation
2);
spatialtrans_kneejoint.upd_translation3().append_coordinates('Knee_Rz');
spatialtrans_kneejoint.upd_translation3().set_axis(Vec3(0, 0, 1));
simmspline_translation3 = SimmSpline();
simmspline_translation3.addPoint(deg2rad(-150), -0.0003);
simmspline_translation3.addPoint(deg2rad(-113), -0.00032);
simmspline_translation3.addPoint(deg2rad(-82), -0.00035);
simmspline_translation3.addPoint(deg2rad(-60), -0.0004);
simmspline_translation3.addPoint(deg2rad(-41), -0.0006);
spatialtrans_kneejoint.upd_translation3().set_function(simmspline_translation
3);
kneejoint = CustomJoint(JCS{k,1}, Parentlist{k}, LocationInParent,
OrientationInParent, cell2mat(Bodylist(k,1)), LocationInChild,
OrientationInChild, spatialtrans_kneejoint);
JerboaModel.addJoint(kneejoint); %adding joint to the model
kneejoint.upd_coordinates(0).set_default_value(deg2rad(-122));
kneejoint.upd_coordinates(0).set_range(0, deg2rad(-150));
kneejoint.upd_coordinates(0).set_range(1, deg2rad(-41));
kneejoint.upd_coordinates(0).set_clamped(true);
kneejoint.upd_coordinates(0).set_locked(false);
kneejoint.upd_coordinates(0).set_prescribed(false);
%% Section 2.2.2 Patella-Femoral Joint Function
%Creation of the Patella femoral joint and allowing for translation.
elseif k == 4
LocationInParent = Vec3(JCS{k,7}, JCS{k,8}, JCS{k,9});
OrientationInParent =
Vec3(deg2rad(JCS{k,4}),deg2rad(JCS{k,5}),deg2rad(JCS{k,6}));
LocationInChild = Vec3(0);
OrientationInChild = Vec3(0);
spatialtrans_Patjoint = SpatialTransform();
spatialtrans_Patjoint.upd_rotation1().append_coordinates('Pat_Rx');
spatialtrans_Patjoint.upd_rotation1().set_axis(Vec3(1, 0, 0));
spatialtrans_Patjoint.upd_rotation1().set_function(LinearFunction(1, 0));
spatialtrans_Patjoint.upd_rotation2().append_coordinates('Pat_Ry');
spatialtrans_Patjoint.upd_rotation2().set_axis(Vec3(0, 1, 0));
spatialtrans_Patjoint.upd_rotation2().set_function(LinearFunction(1, 0));
spatialtrans_Patjoint.upd_rotation3().append_coordinates('Pat_Rz');
```

```
spatialtrans_Patjoint.upd_rotation3().set_axis(Vec3(0, 0, 1));
spatialtrans_Patjoint.upd_rotation3().set_function(LinearFunction(1, 0));
spatialtrans_Patjoint.upd_translation1().append_coordinates('Pat_Tx');
spatialtrans_Patjoint.upd_translation1().set_axis(Vec3(1, 0, 0));
spatialtrans_Patjoint.upd_translation1().set_function(LinearFunction(1, 0));
spatialtrans_Patjoint.upd_translation2().append_coordinates('Pat_Ty');
spatialtrans_Patjoint.upd_translation2().set_axis(Vec3(0, 1, 0));
spatialtrans_Patjoint.upd_translation2().set_function(LinearFunction(1, 0));
Patjoint = CustomJoint(JCS{k,1}, Parentlist{k}, LocationInParent,
OrientationInParent, cell2mat(Bodylist(k,1)), LocationInChild,
OrientationInChild, spatialtrans_Patjoint);
JerboaModel.addJoint(Patjoint); %adding joint to the model
%% Section 2.2.3 Pelvic translation addition
%In the event of conducitng inverse kinematics, the pelvis is required to
%have open translation capabilities, and thus the below is added for the
%pelvis alone, as all other joints will follow the parent body.
elseif k == 1 %for pelvis translation
LocationInParent = Vec3(JCS{k,7}, JCS{k,8}, JCS{k,9});
OrientationInParent =
Vec3(deg2rad(JCS{k,4}),deg2rad(JCS{k,5}),deg2rad(JCS{k,6}));
LocationInChild = Vec3(0);
OrientationInChild = Vec3(0);
spatialtrans_joint = SpatialTransform();
spatialtrans_joint.upd_rotation1().append_coordinates(JCS{k,10});
spatialtrans_joint.upd_rotation1().set_axis(Vec3(1, 0, 0));
spatialtrans_joint.upd_rotation1().set_function(LinearFunction(1, 0));
spatialtrans_joint.upd_rotation2().append_coordinates(JCS{k,11});
spatialtrans_joint.upd_rotation2().set_axis(Vec3(0, 1, 0));
spatialtrans_joint.upd_rotation2().set_function(LinearFunction(1, 0));
spatialtrans_joint.upd_rotation3().append_coordinates(JCS{k,12});
spatialtrans_joint.upd_rotation3().set_axis(Vec3(0, 0, 1));
spatialtrans_joint.upd_rotation3().set_function(LinearFunction(1, 0));
spatialtrans_joint.upd_translation1().append_coordinates(JCS{k,13});
spatialtrans_joint.upd_translation1().set_axis(Vec3(1, 0, 0));
spatialtrans_joint.upd_translation1().set_function(LinearFunction(1, 0));
spatialtrans_joint.upd_translation2().append_coordinates(JCS{k,14});
spatialtrans_joint.upd_translation2().set_axis(Vec3(0, 1, 0));
spatialtrans_joint.upd_translation2().set_function(LinearFunction(1, 0));
spatialtrans_joint.upd_translation3().append_coordinates(JCS{k,15});
spatialtrans_joint.upd_translation3().set_axis(Vec3(0, 0, 1));
spatialtrans_joint.upd_translation3().set_function(LinearFunction(1, 0));
joint = CustomJoint(JCS{k,1}, Parentlist{k}, LocationInParent,
OrientationInParent, cell2mat(Bodylist(k,1)), LocationInChild,
OrientationInChild, spatialtrans_joint);
JerboaModel.addJoint(joint); %adding joint to the model
%Updating range of motion and default model config
joint.upd_coordinates(0).set_default_value(deg2rad(Range{k,8}));
joint.upd_coordinates(0).set_range(0, deg2rad(Range{k,2}));
joint.upd_coordinates(0).set_range(1, deg2rad(Range{k,3}));
joint.upd_coordinates(0).set_clamped(true);
joint.upd_coordinates(0).set_locked(true);
joint.upd_coordinates(0).set_prescribed(false);
joint.upd_coordinates(1).set_default_value(deg2rad(Range{k,9}));
joint.upd_coordinates(1).set_range(0, deg2rad(Range{k,4}));
joint.upd_coordinates(1).set_range(1, deg2rad(Range{k,5}));
joint.upd_coordinates(1).set_clamped(true);
joint.upd_coordinates(1).set_locked(true);
```

```
joint.upd_coordinates(1).set_prescribed(false);
joint.upd_coordinates(2).set_default_value(deg2rad(Range{k,10}));
joint.upd_coordinates(2).set_range(0, deg2rad(Range{k,6}));
joint.upd_coordinates(2).set_range(1, deg2rad(Range{k,7}));
joint.upd_coordinates(2).set_clamped(true);
joint.upd_coordinates(2).set_locked(false);
joint.upd_coordinates(2).set_prescribed(false);
joint.upd_coordinates(3).set_default_value(deg2rad(0));
joint.upd_coordinates(3).set_clamped(true);
joint.upd_coordinates(3).set_locked(false);
joint.upd_coordinates(3).set_prescribed(false);
joint.upd_coordinates(4).set_default_value(deg2rad(0));
joint.upd_coordinates(4).set_clamped(true);
joint.upd_coordinates(4).set_locked(false);
joint.upd_coordinates(4).set_prescribed(false);
joint.upd_coordinates(5).set_default_value(deg2rad(0));
joint.upd_coordinates(5).set_clamped(true);
joint.upd_coordinates(5).set_locked(false);
joint.upd_coordinates(5).set_prescribed(false);
%% Section 2.2.4 For all other joints with constant centers of rotation and
only x,y,z rotation.
else
LocationInParent = Vec3(JCS{k,7}, JCS{k,8}, JCS{k,9});
OrientationInParent =
Vec3(deg2rad(JCS{k,4}),deg2rad(JCS{k,5}),deg2rad(JCS{k,6}));
LocationInChild = Vec3(0);
OrientationInChild = Vec3(0);
spatialtrans_joint = SpatialTransform();
spatialtrans_joint.upd_rotation1().append_coordinates(JCS{k,10});
spatialtrans_joint.upd_rotation1().set_axis(Vec3(1, 0, 0));
spatialtrans_joint.upd_rotation1().set_function(LinearFunction(1, 0));
spatialtrans_joint.upd_rotation2().append_coordinates(JCS{k,11});
spatialtrans_joint.upd_rotation2().set_axis(Vec3(0, 1, 0));
spatialtrans_joint.upd_rotation2().set_function(LinearFunction(1, 0));
spatialtrans_joint.upd_rotation3().append_coordinates(JCS{k,12});
spatialtrans_joint.upd_rotation3().set_axis(Vec3(0, 0, 1));
spatialtrans_joint.upd_rotation3().set_function(LinearFunction(1, 0));
joint = CustomJoint(JCS{k,1}, Parentlist{k}, LocationInParent,
OrientationInParent, cell2mat(Bodylist(k,1)), LocationInChild,
OrientationInChild, spatialtrans_joint);
JerboaModel.addJoint(joint); %adding joint to the model
%Updating range of motion and default model config
joint.upd_coordinates(0).set_default_value(deg2rad(Range{k,8}));
joint.upd_coordinates(0).set_range(0, deg2rad(Range{k,2}));
joint.upd_coordinates(0).set_range(1, deg2rad(Range{k,3}));
joint.upd_coordinates(0).set_clamped(true);
joint.upd_coordinates(0).set_locked(true);
joint.upd_coordinates(0).set_prescribed(false);
joint.upd_coordinates(1).set_default_value(deg2rad(Range{k,9}));
joint.upd_coordinates(1).set_range(0, deg2rad(Range{k,4}));
joint.upd_coordinates(1).set_range(1, deg2rad(Range{k,5}));
joint.upd_coordinates(1).set_clamped(true);
joint.upd_coordinates(1).set_locked(true);
joint.upd_coordinates(1).set_prescribed(false);
joint.upd_coordinates(2).set_default_value(deg2rad(Range{k,10}));
joint.upd_coordinates(2).set_range(0, deg2rad(Range{k,6}));
joint.upd_coordinates(2).set_range(1, deg2rad(Range{k,7}));
```

```
joint.upd_coordinates(2).set_clamped(true);
joint.upd_coordinates(2).set_locked(false);
joint.upd_coordinates(2).set_prescribed(false);
end
end

%% Section 2.2.5: Adding Patella Femoral Joint Constraint
%Since the patella must be constrained to the motion of the knee joint
%which is a joint outside its parent body functions, constraints must be
%applied after the joint is generated as shown below.
con1 = CoordinateCouplerConstraint();
con1.setName('Pat_Rx_con');
con1.set_isEnforced(true);
simmspline_func_4_con1 = SimmSpline();
simmspline_func_4_con1.addPoint(deg2rad(-150), deg2rad(22.247572));
simmspline_func_4_con1.addPoint(deg2rad(-110), deg2rad(22.247572));
simmspline_func_4_con1.addPoint(deg2rad(-41), deg2rad(22.247572));
independentCoords_4_con1 = ArrayStr();
independentCoords_4_con1.append('Knee_Rz');
con1.setIndependentCoordinateNames(independentCoords_4_con1);
con1.setDependentCoordinateName('Pat_Rx')
con1.setFunction(simmspline_func_4_con1);
JerboaModel.addConstraint(con1);
con5 = CoordinateCouplerConstraint();
con5.setName('Pat_Ry_con');
con5.set_isEnforced(true);
simmspline_func_4_con5 = SimmSpline();
simmspline_func_4_con5.addPoint(deg2rad(-150), deg2rad(-1.649062));
simmspline_func_4_con5.addPoint(deg2rad(-110), deg2rad(-1.649062));
simmspline_func_4_con5.addPoint(deg2rad(-41), deg2rad(-1.649062));
independentCoords_4_con5 = ArrayStr();
independentCoords_4_con5.append('Knee_Rz');
con5.setIndependentCoordinateNames(independentCoords_4_con5);
con5.setDependentCoordinateName('Pat_Ry')
con5.setFunction(simmspline_func_4_con5);
JerboaModel.addConstraint(con5);
con6 = CoordinateCouplerConstraint();
con6.setName('Pat_Rz_con');
con6.set_isEnforced(true);
simmspline_func_4_con6 = SimmSpline();
simmspline_func_4_con6.addPoint(deg2rad(-150), deg2rad(-77.038555));
simmspline_func_4_con6.addPoint(deg2rad(-110), deg2rad(-64.92));
simmspline_func_4_con6.addPoint(deg2rad(-41), deg2rad(-26.25));
independentCoords_4_con6 = ArrayStr();
independentCoords_4_con6.append('Knee_Rz');
con6.setIndependentCoordinateNames(independentCoords_4_con6);
con6.setDependentCoordinateName('Pat_Rz')
con6.setFunction(simmspline_func_4_con6);
JerboaModel.addConstraint(con6);
con2 = CoordinateCouplerConstraint();
con2.setName('Pat_Tx_con');
con2.set_isEnforced(true);
simmspline_func_4_con2 = SimmSpline();
simmspline_func_4_con2.addPoint(deg2rad(-150), 0);
simmspline_func_4_con2.addPoint(deg2rad(-110), 0.001);
simmspline_func_4_con2.addPoint(deg2rad(-41), 0.0032);
```

```
independentCoords_4_con2 = ArrayStr();
independentCoords_4_con2.append('Knee_Rz');
con2.setIndependentCoordinateNames(independentCoords_4_con2);
con2.setDependentCoordinateName('Pat_Tx')
con2.setFunction(simmspline_func_4_con2);
JerboaModel.addConstraint(con2);
con3 = CoordinateCouplerConstraint();
con3.setName('Pat_Ty_con');
con3.set_isEnforced(true);
simmspline_func_4_con3 = SimmSpline();
simmspline_func_4_con3.addPoint(deg2rad(-150), 0);
simmspline_func_4_con3.addPoint(deg2rad(-110), -0.00025);
simmspline_func_4_con3.addPoint(deg2rad(-41), 0);
independentCoords_4_con3 = ArrayStr();
independentCoords_4_con3.append('Knee_Rz');
con3.setIndependentCoordinateNames(independentCoords_4_con3);
con3.setDependentCoordinateName('Pat_Ty')
con3.setFunction(simmspline_func_4_con3);
JerboaModel.addConstraint(con3);

%% Section 3.1: Adding Muscles
%Using parameters detailed in the excel sheet, this for loop adds all
%muscles and their corresponding values in a generic hill type muscle
%model.

for l = 1:height(MUS)
muscle = Millard2012EquilibriumMuscle();
muscle.setName(MUS{l,1});
muscle.setMaxIsometricForce(MUS{l,4});
muscle.setOptimalFiberLength(MUS{l,2});
muscle.setTendonSlackLength(MUS{l,5});
muscle.setPennationAngleAtOptimalFiberLength(deg2rad(MUS{l,3}));
Musclelist(l) = muscle; %Generating a list of the muscles as they are created
to call back later
end

%% Section 3.2: Adding Muscle Path Points
%After parameters, muscle path must be defined, to dictat line of action
%seen and used in GUI/OpenSim
Musclestr = MUS{:,1};
Muscle_path = MUSPoints{:,1};
Muscle_path_body = MUSPoints{:,3};

for p = 1:height(MUSPoints)
r(p) = find(strcmp(Muscle_path{p}, Musclestr));
Mus_points(p) = Musclelist(r(p));
t(p) = find(strcmp(Muscle_path_body{p}, Childbodystr));
Pathbodylist(p) = cell2mat(Bodylist(t(p),1)); %Finding bodies assocaiated
with each wrap
%This for loop sifts through the strings and will create bodies that
%opensim code can read by cross referencing strings to the xls sheet.
Upd_path_point = Vec3(MUSPoints{p,4}, MUSPoints{p,5}, MUSPoints{p,6});
Mus_points(p).addNewPathPoint(MUSPoints{p,2}, Pathbodylist(p),
Upd_path_point);
end
```

```
for a = 1:height(MUS)
JerboaModel.addForce(Musclelist(a));
end

%% Section 3.3: Creating Wrapping Cylinders
%Wrapping surfaces are similarly implemented using the google sheet to
%constrain muscle line of action path.
Mus_wrap_str = Wraps{:,3};
wrapbodystr = Wraps{:,2};

for q = 1:height(Wraps)
D(q) = find(strcmp(Mus_wrap_str{q}, Musclestr));
Mus_path(q) = Musclelist(D(q));
f(q) = find(strcmp(wrapbodystr{q}, Childbodystr));
Wrapbodylist(q) = cell2mat(Bodylist(f(q),1)); %Finding bodies assocaiated
with each wrap
%This for loop sifts through the strings and will create bodies that
%opensim code can read by cross referencing strings to the xls sheet.

wrap = WrapCylinder();
wrap.setName(cell2mat(Wraps{q,1}));
wrap.set_active(true);
wrap.set_xyz_body_rotation(Vec3(deg2rad(Wraps{q,4}), deg2rad(Wraps{q,5}),
deg2rad(Wraps{q,6})));
wrap.set_translation(Vec3(Wraps{q,7}, Wraps{q,8}, Wraps{q,9}));
wrap.set_quadrant(cell2mat(Wraps{q,12}));
wrap.upd_Appearance().set_visible(false);
wrap.upd_Appearance().set_opacity(0.5);
wrap.upd_Appearance().set_color(Vec3(0, 1, 1));
wrap.upd_Appearance().upd_SurfaceProperties().set_representation(3);
wrap.set_radius(Wraps{q,10});
wrap.set_length(Wraps{q,11});
Wrapbodylist(q).addWrapObject(wrap);
Mus_path(q).updGeometryPath().addPathWrap(wrap);
end

%% Section 3.4: Creating Wrapping Spheres
Mus_wrap_S_str = Wraps_S{:,3};
wrapsbodystr = Wraps_S{:,2};

for d = 1:height(Wraps_S)
G(d) = find(strcmp(Mus_wrap_S_str{d}, Musclestr));
Mus_paths(d) = Musclelist(G(d));
V(d) = find(strcmp(wrapsbodystr{d}, Childbodystr));
Wrapsbodylist(d) = cell2mat(Bodylist(V(d),1));
wrap_s = WrapEllipsoid();
wrap_s.setName(cell2mat(Wraps_S{d,1}));
wrap_s.set_active(true);
wrap_s.set_xyz_body_rotation(Vec3(deg2rad(Wraps_S{d,4}),
deg2rad(Wraps_S{d,5}), deg2rad(Wraps_S{d,6})));
wrap_s.set_translation(Vec3(Wraps_S{d,7}, Wraps_S{d,8}, Wraps_S{d,9}));
wrap_s.set_dimensions(Vec3(Wraps_S{d,10}, Wraps_S{d,11}, Wraps_S{d,12}))
wrap_s.set_quadrant(cell2mat(Wraps_S{d,13}));
wrap_s.upd_Appearance().set_visible(false);
wrap_s.upd_Appearance().set_opacity(0.5);
wrap_s.upd_Appearance().set_color(Vec3(0, 1, 1));
```

```
wrap_s.upd_Appearance().upd_SurfaceProperties().set_representation(3);
Wrapsbodylist(d).addWrapObject(wrap_s);
Mus_paths(d).updGeometryPath().addPathWrap(wrap_s);
end

%% Section 3.5: Adding Muscle Groups
%Below muscles are moved into various categories of functional groups for
%ease of retrieving after running opensim model. These groups are based on
%previously defined rodent and human hindlimb functional groups.
Musc_group = 'Knee_extensors';
JerboaModel.updForceSet().addGroup(Musc_group);
memberlist = {'Vastus_Lateralis', 'Vastus_Medialis', 'Rectus_Femoris',
'Vastus_Intermedius'};

for gr = 1 : length(memberlist)
JerboaModel.updForceSet().addObjectToGroup(Musc_group, memberlist{gr});
end

Musc_group = 'Knee_flexor';
JerboaModel.updForceSet().addGroup(Musc_group);
memberlist = {'Popliteus'};

for gr = 1 : length(memberlist)
JerboaModel.updForceSet().addObjectToGroup(Musc_group, memberlist{gr});
end

Musc_group = 'Ankle_Plantarflexors';
JerboaModel.updForceSet().addGroup(Musc_group);
memberlist = {'Medial_Gastrocnemius', 'Lateral_Gastrocnemius', 'Plantaris',
'Soleus', 'Flexor_Digitorum_Longus'};

for gr = 1 : length(memberlist)
JerboaModel.updForceSet().addObjectToGroup(Musc_group, memberlist{gr});
end

Musc_group = 'Ankle_Dorsiflexors';
JerboaModel.updForceSet().addGroup(Musc_group);
memberlist = {'Tibialis_Anterior', 'Extensor_Digitorum_Longus'};

for gr = 1 : length(memberlist)
JerboaModel.updForceSet().addObjectToGroup(Musc_group, memberlist{gr});
end

Musc_group = 'Ankle_Everters';
JerboaModel.updForceSet().addGroup(Musc_group);
memberlist = {'Peroneus_Longus', 'Peroneus_digiti_quarti', };

for gr = 1 : length(memberlist)
JerboaModel.updForceSet().addObjectToGroup(Musc_group, memberlist{gr});
end

Musc_group = 'Hip_Extensors';
JerboaModel.updForceSet().addGroup(Musc_group);
```

```
memberlist = {'Semimembranosus', 'Semitendinosus',
'Biceps_Femoris_Posterior_cranial', 'Biceps_Femoris_Posterior_mid',
'Biceps_Femoris_Anterior'};

for gr = 1 : length(memberlist)
JerboaModel.updForceSet().addObjectToGroup(Musc_group, memberlist{gr});
end

Musc_group = 'Hip_Flexors';
JerboaModel.updForceSet().addGroup(Musc_group);
memberlist = {'Pectineus', 'Iliacus', };

for gr = 1 : length(memberlist)
JerboaModel.updForceSet().addObjectToGroup(Musc_group, memberlist{gr});
end

Musc_group = 'Hip_Rotators';
JerboaModel.updForceSet().addGroup(Musc_group);
memberlist = {'Gluteus_Maximus_dorsal', 'Gluteus_Maximus_middle',
'Gluteus_Maximus_ventral', 'Gemellus', 'Gemellus_superior'};

for gr = 1 : length(memberlist)
JerboaModel.updForceSet().addObjectToGroup(Musc_group, memberlist{gr});
end

Musc_group = 'Hip_Adductors';
JerboaModel.updForceSet().addGroup(Musc_group);
memberlist = {'Adductor_magnus', 'Adductor_brevis', 'Adductor_longus',
'Gracilis_posterior', 'Gracilis_anterior'};

for gr = 1 : length(memberlist)
JerboaModel.updForceSet().addObjectToGroup(Musc_group, memberlist{gr});
end

%%
JerboaModel.updMarkerSet();
%%
JerboaModel.finalizeConnections();
%%
JerboaModel.print('Jerboa _SIM.osim');
disp('Model Printed')
```